MORPHO-TECTONIC ANALYSIS OF THE EAST AFRICAN RIFT SYSTEM

By

LIANG XUE

Bachelor of Engineer in Geological Engineering
Central South University
Changsha, China
2011

Master of Science in Geology
Missouri University of Science and Technology
Rolla, Missouri
2014

Submitted to the Faculty of the
Graduate College of the
Oklahoma State University
in partial fulfillment of
the requirements for
the Degree of
DOCTOR OF PHILOSOPHY
July, 2018

MORPHO-TECTONIC ANALYSIS OF THE EAST

AFRICAN RIFT SYSTEM

Dissertation Approved:

Dr. Mohamed Abdelsalam

Dissertation Adviser

Dr. Estella Atekwana

Dr. Danial Lao Davila

Dr. Amy Frazier

Dr. Javier Vilcaez Perez

ACKNOWLEDGEMENTS

This research could never have been completed without the support of my mentors, colleagues, friends, and family. I would thank my advisor, Dr. Mohamed Abdelsalam, who has introduced me to the geology of the East African Rift System. I was given so much trust, encouragement, patience, and freedom to explore anything that interests me in geoscience, including tectonic/fluvial geomorphology, unmanned aerial system/multi-special remote sensing, and numerical modeling. I thank my other members of my committee, Drs. Estella Atekwana, Daniel Lao Davila, Amy Frazier, and Javier Vilcaez Perez for their guidance in this work, as well as for their help and suggestion on my academic career. Their writing and teaching have always inspired me during my time at Oklahoma State University. The understanding, encouragement from my committee members have provided a good basis for the present dissertation. Also, I thank Dr. Nahid Gani, of Western Kentucky University for her contribution to editing and refining my three manuscripts constituting this dissertation.

It has been four years since I came to Oklahoma State University for my PhD program. I have greatly benefited over that time from interaction with my teachers and colleagues. The professors in Geology and Geography departments prepared me to be a much more balanced researcher. I also wish to express my appreciation to the Boone Pickens School of Geology, for providing the Graduate Teaching Assistant, and fellowships that made my study possible.

Further, I would like to thank several communities. This work is partially supported by American Association of Petroleum Geologists' Grant-in-Aid fund and Geological Society of America's Graduate Research Funding. I also thank the members of American Geophysical Union Gilbert Club and Community Surface Dynamics Modeling System for sharing their data, code, and helping me with methodologies of this work.

To my colleagues and treasured friends in the PhD office (NRC 412) and in the Geodynamic and Geospatial Science lab (NRC 303), Tadesse Alemu, Mercy Achang, Sahar Mohammadi, Jingyao Meng, Pouyan Ebrahimi, Ibukun Bode Omoleye, Zelalem Demissie, Folarin Kolawole, and Andrew Katumwehe, Babak Shabani, Luel Emishaw, I cannot give enough thanks for their supports, encourage, friendship, and good moments. A sincere thank is also due to all members of the Tectonic Group for their intellectual discussions, as well as for collaboration with Steven Johnson and Ines Barrios Galindez in their research projects.

Finally, I am grateful to my parents, grandma, and Shaoyi, who supported my efforts throughout this long journey. During my four years in the PhD program, I have only been back home once, so I would also like to thank my family and friends in China who have tolerated my long absence.

Name: LIANG XUE

Date of Degree: JULY, 2018

Title of Study: MORPHO-TECTONIC ANALYSIS OF THE DRAINAGE SYSTEMS IN THE EAST AFRICAN RIFT SYSTEM

Major Field: GEOLOGY

Abstract: Tectonic uplift of mountain ranges and plateaus have a significant impact on the geological record by influencing drainage systems and sediment supply, and on climate and on biogeography. Recent geomorphological, geochronological and geophysical studies have provided some understanding of time constraints and uplift rate distribution patterns, especially in convergent plate margins. Nevertheless, fewer studies took a comprehensive view over the topographic patterns, rates and changes in rates of tectonic uplift in continental rift systems. We do not know the how ground's vertical motion is localized along the axis of rift and the relative roles of upwelling of magma and rift extensional processes play in tectonic uplift history. The East African Rift System (EARS) has long served as the ideal example of a continental rift to explore the distribution patterns, rates, and timing of tectonic uplift in the evolution of geomorphology. This work addresses fundamental questions of tectonic uplift and its footprint on the topography associated with rift systems. Specifically, three distinct segments along the EARS, the Rwenzori Mountains in the Western Branch, the southeastern Ethiopian Plateau in the Northern Branch and the Kenyan Rift in the Eastern Branch are investigated. The first chapter evaluated geomorphic proxies in the Rwenzori Mountains. We found that the linear geomorphic proxies (normalized steepness and chi integral) have strong positive correlation with the erosion rates. Additionally, our geomorphic proxy results suggest that the north and south sectors of the Rwenzori Mountains are in relative tectonic quiescence but that the central sector is experiencing higher levels of erosion and rock uplift. The second chapter used morphotectonic analysis to study the tectonic uplift history of the southeastern Ethiopian Plateau (SEEP). We find an increase in tectonic uplift rates from the southeastern escarpments of the Afar Depression in the northeast to that of the Main Ethiopian Rift to the southwest. We identify three regional tectonic uplift events at ~11.7, ~6.5, and ~4.5 Ma recorded by the development of regionally distributed knickpoints. This is in good agreement with ages of tectonic uplift events reported from the Northwestern Ethiopian Plateau. The third chapter examined the tectonic uplift history of the Kenya Rift. This work found that the spatial and temporal pattern of the tectonic uplift inferred from the drainage incision is well-correlated with known phases of magmatic activities. Also, this work found that the rapid increase in drainage incision since ~4.5 Ma correlated well with a major change in vegetation from grassland to woodland. This suggests that the tectonic uplift coupled with Pliocene magmatic activities have caused a major shift in the ecosystem in the region.

PUBLICATION DISSERTATION OPTION

This dissertation has been structured in two sections. The first section (Chapter 1) gives a brief introduction of the dissertation and introduces the scientific questions investigated in this research. The second section (Chapters 2, 3, and 4) also presents three manuscripts including two that have been published and one in preparation for publication.

Paper 1: Xue, Liang, Nahid D. Gani, and Mohamed G. Abdelsalam. "Geomorphologic proxies for bedrock rivers: A case study from the Rwenzori Mountains, East African Rift system." Geomorphology 285 (2017): 374-398.

Paper 2: Xue, Liang, Alemu, Tadesse, Nahid D. Gani, and Mohamed G. Abdelsalam. "Spatial and temporal variation of tectonic uplift in the southeastern Ethiopian Plateau from morphotectonic analysis." Geomorphology 309 (2018): 98-111.

Paper 3: Xue, Liang, Nahid D. Gani, and Mohamed G. Abdelsalam. (*Submitted*) "Drainage incision, tectonic uplift, and magmatism of the Kenya rift, East African Rift System: a morpho-tectonic analysis approach." JGR-Earth Surface.

TABLE OF CONTENTS

LIST OF TABLES

LIST OF FIGURES

CHAPTER I

INTRODUCTION

1.0. Project Motivation

Continental rifts, where the continental lithosphere begin stretching to ultimately form new oceans is a central tenet of plate tectonics. One of the most prominent features of rift systems is the uplifted flanks developed parallel to the axis of extension. Such tectonic uplift is fundamental for reconstructing extensional processes, evaluating changes of the paleo-environments, and assessing hydrocarbon resource potential. Success has been made for an integrated and quantitative investigation of tectonic uplift by using the feedbacks of topography, often referred to as morpho-tectonic analysis (Burbank and Anderson, 2011; Keller and Pinter, 2002). Nevertheless, few, if any of these previous studies took a comprehensive view over the topographic expression of patterns, rates and changes in rates of uplift in continental rift systems. We do not know how the ground's vertical motion is localized along the axis of rift and the relative roles of upwelling of magma and rift extensional processes play in tectonic uplift history. Knowledge gaps remain regarding the questions on: (1) whether the topographic feedbacks to tectonic uplift (geomorphic proxies), which are successfully applied in convergent plate boundaries, can be as equally successfully applied to continental rift settings, where the erosion/uplift rates are comparatively lower; (2) what is the implication of the geomorphic

proxies on the distribution patterns of tectonic uplift rates on rift flanks; and (3) what is tectonic uplift history of the rift flanks and its potential interaction with rifting processes.

1.1. Objectives

The objectives of this work are to use the East African Rift System (EARS) to contribute to morpho-tectonic studies by providing examples these aims. (1) Examining the effectiveness of geomorphic proxies in depicting the spatial and temporal resolution of tectonic uplift rates in continental tectonic setting where the tectonic uplift rates are relatively low compared to those dominating convergent plate boundaries. (2) Using the well-tested geomorphic proxies to establish the uplift history of the southeastern flank of Northern Branch (mainly the Southeastern Ethiopian Plateau) of the EARS. (3) Using geomorphic proxies and topographic modeling to establish the relationship between tectonic uplift, magmatism and rifting in the Eastern Branch of the EARS (mainly the Kenya Rift). First, morpho-tectonic analysis was carried out in the Rwenzori Mountains, which is situated within the Albertine Rift of the Western Branch of the EARS (Fig. 1). Efforts have been made to investigate the cooling history, erosion rate and climate of these mountains (Baber, 2013; Bauer et al., 2015; Bauer et al., 2010; Ring, 2008; Roller et al., 2012), providing important independent constraints for the morpho-tectonic interpretation of our geomorphic proxy's results. Here, the geomorphic proxies which are widely used in last decades are evaluated to verify if they can quantify erosion/ uplift rate regarding magnitude and location in continental rift settings.

Second, this study used the most valid and robust geomorphic proxies to measure the relative uplift rates and tectonic activities of individual drainage basins in the southeastern Ethiopia Plateau, comparing the maturity state of the basins between north and south Main Ethiopian Rift . Moreover, we employed a knickpoint celerity model to determine the existence of multi-stage uplift history of southeastern Ethiopia, and compare the results to the findings from northwestern Ethiopian Plateau.

Third, the linkage between magmatism and tectonic uplift in the Kenya Rift is explored using morpho-tectonic analysis and published geochronological data. Also, the correlation between tectonic uplift, curst cooling history, magmatism, and paleoclimate is investigated since 15 Ma.

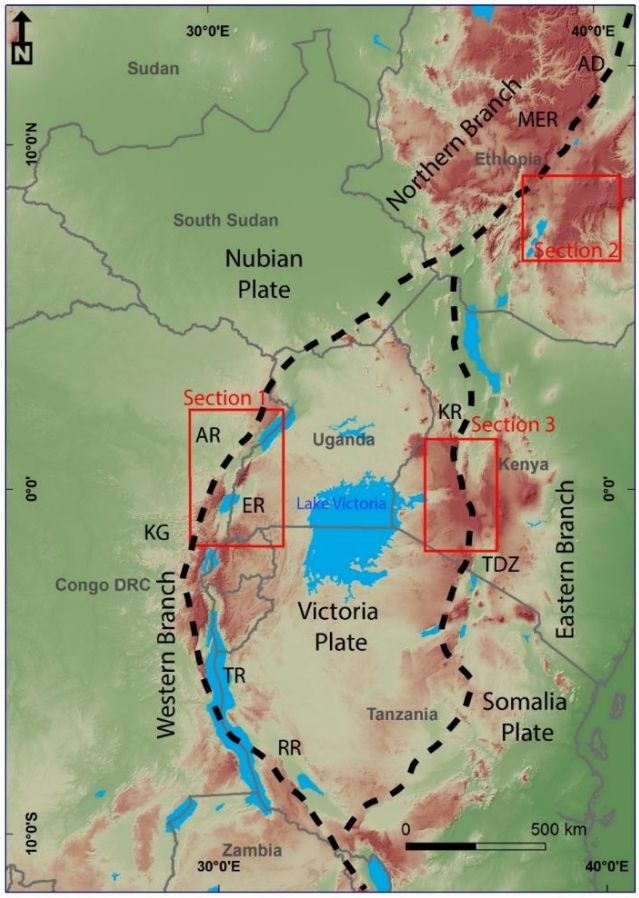

Figure 1- 1 Digital Elevation Model (DEM) generated from the 1 km spatial resolution Global Multi-resolution Terrain Elevation Data, showing the East African Rift System (EARS) and Northern, Eastern, Western Branches, and the three sections present in this work. AD= Afar Depression. MER= Main Ethiopian Rift. KR=Kenya Rift. TDZ=Tanzania Divergent Zone. AR=Albertine and Rhino Grabens. ER=Edward-George Rift. KG=Kivu Graben. TR=Tanganyika Rift. RR=Rukwa Rift. MR=Malawi Rift.

1.2. Significance

Results from this work advance the knowledge base of tectonic geomorphology. The usefulness of geomorphic proxies is assessed in quantifying the uplift and/or erosion rates in rift setting, where the erosion rate, or uplift rate in steady state, is much lower compared to collision zone (Kirby and Whipple, 2012; Perez-Pena et al., 2010). Therefore, this research will develop a new

framework for applying morpho-tectonic analysis to rift systems and in doing so, will move the scientific community toward a more comprehensive and quantitative understanding of the geomorphic response to both lateral and vertical crustal motion. Moreover, this work is the first attempt to correlate the spatial patterns of uplift to the Moho depth derived from two-dimensional (2D) spectral analysis of gravity data to explore the possible triggers and timing of uplift events. Such interdisciplinary study will complement our understanding of the techniques of morpho-tectonic analysis, which has the potential to apply to other rift systems around the world.

Besides, the results of this project yield important first-order observations on the linkage between topography and uplift in three distinct regions across the EARS. These results provide a spatially continuous image of uplift process from MER in the Northern Branch, the Rwenzori Mountains in the Western Branches, to the Eastern Branch. The distribution pattern of geomorphic proxies and knickpoint celerity models addresses long-standing controversy about the uplift history of the mountain belts, including the Rwenzori Mountains and Ethiopia Plateau, and mechanisms behind uplift. Moreover, insights in to uplift history and the approach to equilibrium among lithology, topography and erosion (and their spatial variation) will be compared to the mantle flow field and lithospheric structure gained from the gravity study. Such a powerful combination of temporal and spatial constraints will enable the evaluation of the importance of episodicity of tectonic uplift and magmatism in accommodating extension and initiation of the uplift.

Furthermore, the study of continental rift uplift evolution throughout the long-lived extensional process along the EARS has the potential to improve understanding of the range of contributions from isostasy and dynamic topographic mechanisms. While many studies focus on uplift history, this work examines the geomorphic development and how contributions from mantle upwelling and isostasy over time as rifting matures. Establishing how "fundamental rifting processes, and feedbacks between them, evolve in time and space" is one of the five key Rift Initiation and

Evolution questions identified in the GeoPRISMS draft science plan, thus the result of this project will interface with other GeoPRISMS efforts across disciplines to examine rift development.

Moreover, quantifying the interaction between the tectonics and topography is relevant to a number of societal issues including the rate of sediment input to reservoirs, intensity of erosion processes in agricultural, and geo-hazards problems at potential locations of earthquake and landslides along EARS. Fatal earthquakes, landslides and volcanic hazards produced along the EARS have long threatened to the growing population of the region. Diffuse seismic activities associated with rifting are reported throughout EARS (Chorowicz, 2005). For the study area specifically, the second largest earthquake that ever occurred in East Africa was reported in the Rwenzori Mountains in 1966 (Foster and Jackson, 1998) and an earthquake in Ethiopia also recorded up to a magnitude of 6.3 (Ayele and Arvidsson, 1997). The geomorphic proxies make it possible to identify the basin's maturity and deformation activity, allowing for identification and localization of potential seismic events. Moreover, in this work, related hazards including landslides and volcanism associated with rifting processes that can be evaluated within the drainage basins along EARS. The region constitutes a large portion of the drainage systems for some of the most important rivers in Africa (e.g. White River, Semliki River), and their surface processes directly impact the well-being of millions of people in Africa.

This work reveals the favorable geodynamic settings for mineralization associated with magmatism and trapped hydrocarbon resources in the EARS. A large volume of mineral explorations is carried out along the EARS, because of the magmatism associated with continental rifting (Chorowicz, 2005; Goldrick and Bishop, 2007; Kanazawa and Kamitani, 2006). In the meanwhile, organic-rich units with lacustrine origin are a significant source of hydrocarbons throughout the world, and a large number of such extant lakes are located in the continental extensional basins (Karp et al., 2012). By quantifying the erosion pattern and rate, this

project can provide insight on localization of sediment accumulation and further improve the understanding of the relationship between rift evolution and hydrocarbon habitat.

1.3. References

Ayele, A., and Arvidsson, R., 1997, Fault mechanisms and tectonic implication of the 1985–1987 earthquake sequence in south-western Ethiopia: Journal of Seismology, v. 1, no. 4, p. 383-394.

Baber, M. B., 2013, Surface-exposure (10Be) dating of the Omurubaho moraines in the Rwenzori Mountains of Uganda, Dartmouth College.

Bauer, F., Glasmacher, U., Ring, U., Grobe, R., Mambo, V., and Starz, M., 2015, Long-term cooling history of the Albertine Rift: new evidence from the western rift shoulder, DR Congo: International Journal of Earth Sciences, p. 1-22.

Bauer, F., Glasmacher, U., Ring, U., Schumann, A., and Nagudi, B., 2010, Thermal and exhumation history of the central Rwenzori Mountains, Western Rift of the East African Rift System, Uganda: International Journal of Earth Sciences, v. 99, no. 7, p. 1575-1597.

Burbank, D. W., and Anderson, R. S., 2011, Tectonic geomorphology, John Wiley & Sons.

Chorowicz, J., 2005, The east African rift system: Journal of African Earth Sciences, v. 43, no. 1, p. 379-410.

Foster, A. N., and Jackson, J. A., 1998, Source parameters of large African earthquakes: implications for crustal rheology and regional kinematics: Geophysical Journal International, v. 134, no. 2, p. 422-448.

Goldrick, G., and Bishop, P., 2007, Regional analysis of bedrock stream long profiles: evaluation of Hack's SL form, and formulation and assessment of an alternative (the DS form): Earth Surface Processes and Landforms, v. 32, no. 5, p. 649-671.

Kanazawa, Y., and Kamitani, M., 2006, Rare earth minerals and resources in the world: Journal of alloys and compounds, v. 408, p. 1339-1343.

Karp, T., Scholz, C. A., and McGlue, M. M., 2012, Structure and stratigraphy of the Lake Albert Rift, East Africa: Observations from seismic reflection and gravity data.

Keller, E. A., and Pinter, N., 2002, Active Tectonics: Earthquakes, Uplift, and Landscape, New Jersey, Prentice Hall.

Kirby, E., and Whipple, K. X., 2012, Expression of active tectonics in erosional landscapes: Journal of Structural Geology, v. 44, p. 54-75.

Perez-Pena, J. V., Azor, A., Azanon, J. M., and Keller, E. A., 2010, Active tectonics in the Sierra Nevada (Betic Cordillera, SE Spain): Insights from geomorphic indexes and drainage pattern analysis: Geomorphology, v. 119, no. 1-2, p. 74-87.

Ring, U., 2008, Extreme uplift of the Rwenzori Mountains in the East African Rift, Uganda: Structural framework and possible role of glaciations: Tectonics, v. 27, no. 4.

Roller, S., Wittmann, H., Kastowski, M., and Hinderer, M., 2012, Erosion of the Rwenzori Mountains, East African Rift, from in situ-produced cosmogenic 10Be: Journal of Geophysical Research: Earth Surface v. 117, no. F3.

CHAPTER II

GEOMORPHOLOGIC PROXIES FOR BEDROCK RIVERS: A CASE STUDY FROM THE RWENZORI MOUNTAINS, EAST AFRICAN RIFT SYSTEM

2.0. Abstract

Geomorphic proxies yield useful insights into understanding long-term endogenic and exogenic response to erosion and/or rock uplift rate. By evaluating these geomorphic proxies, especially those obtained from bedrock streams (areal proxies including asymmetry factor (AF), mountain front sinuosity (S_{mf}), hypsometric integral (HI), geophysical relief, and shape factor (Shp), and linear proxies including normalized steepness index (k_{sn}), length-gradient index (SLk) and Chi gradient (Mχ)), the erosion and/or rock uplift rate can be quantified. We carried out morpho-tectonic analysis in the Rwenzori Mountains, which represents an anomalously uplifted Precambrian horst within the western branch of the East African Rift system (EARS). This study aims to: (1) evaluate the relationship between geomorphic proxies and drainage basin maturity; (2) evaluate the usefulness of geomorphic proxies as recorders of erosion and/or rock uplift rate; (3) evaluate the sensitivity of each geomorphic proxy to the drainage basin size and geometry, stream order, glaciers extent, and local structures; (4) explore internal correlation within the geomorphic proxies; and (5) contribute to the understanding of morphotectonic evolution of the Rwenzori Mountains.

For this, we computed the stream's 'Good of Fitness' (R^2, an indicator of the drainage basin's maturity) and geomorphic proxies for the drainage basins and their streams in the Rwenzori Mountains from the Advanced Spaceborne Thermal Emission and Reflection Radiometer (ASTER) digital elevation model (DEM). Subsequently, we correlated the areal geomorphic proxies with each other and with R^2. Also, we correlated the linear geomorphic proxies with each other and with published erosion rates obtained from cosmogenic ^{10}Be analysis. Our results show that the areal geomorphic proxies (AF, S_{mf}, HI, relief, and Shp), considering the drainage basin size and geometry, stream order, glacier extent, and local structures, can be applied to locally evaluate the maturity of the drainage basin. We also found that the linear geomorphic proxies (k_{sn}, SLk, and Mχ) have strong positive correlation with the erosion rates, they are effective in detecting fault activities, and some of them (k_{sn} and Mχ) are highly correlated with each other. Additionally, our geomorphic proxy results suggest that the north and south sectors of the Rwenzori Mountains are in relative tectonic quiescence but that the central sector is experiencing higher levels of erosion and rock uplift.

2.1. Introduction

A wide range of geomorphic proxies have proven to be valuable in estimating the erosion and/or rock uplift rate in different tectonic settings. These geomorphic proxies include asymmetry factor (AF; Hare and Gardner, 1985; Keller et al., 1997; Perez-Pena et al., 2010), mountain front sinuosity (S_{mf}; Ouchi, 1985; Schumm et al., 2002), hypsometric integral (HI; Ohmori, 1993; Perez-Pena et al., 2009a), geophysical relief (Burbank et al., 1996; Binnie et al., 2007; Carretier et al., 2013), shape factor (Shp; Bull and McFadden, 1977; Kale and Shejwalkar, 2008), normalized steepness index (k_{sn}; Kirby and Whipple, 2001, 2012; Wobus et al., 2006), length-gradient index (SLk; Hack, 1973; Chen et al., 2003; Perez-Pena et al., 2009b, 2010), and Chi gradient (Mχ; Perron and Royden, 2013; Mudd et al., 2014; Willett et al., 2014). The AF, S_{mf}, HI, geophysical relief, and Shp are grouped into areal geomorphic proxies whereas k_{sn}, SLk, and Mχ are grouped into linear geomorphic proxies. Under certain constraints and theoretical assumptions, these geomorphic proxies can be used to quantify the erosion and/or rock uplift rate.

The relationship between the geomorphic proxies and erosion and/or rock uplift rates is built upon empirical equations as well as theoretical assumptions (Delunel et al., 2010; Champagnac et al., 2014). Hence, a number of factors need to be considered when applying these geomorphic proxies for morphotectonic analysis. This is because the numerical value of a geomorphic proxy that is successfully used to estimate the erosion and/or rock uplift rate in one tectonic setting (such as collision zone with high uplift rate > 0.5 mm/y) may not be applicable to a different tectonic setting (such as continental rift systems with low to moderate uplift rate < 0.5 mm/y (Perez-Pena et al., 2010; Kirby and Whipple, 2012).

Furthermore, different approaches that are implemented to extract the geomorphic proxies from the digital elevation model (DEM) can result in different numerical values for these proxies. For example, changing the length of the channel's intervals with which the SLk is calculated results in significantly different numerical values for this proxy, and this can lead to distinctively different morphotectonic interpretations (Perez-Pena et al., 2009b). Also, factors

such as the drainage basin size and geometry, stream order, glacier extent, and local structures can influence the numerical values calculated for some geomorphic proxies and their spatial distribution. For example, it is documented that geomorphic proxies calculated from channels with lower first and second stream order are more influenced by local structures than those calculated for channels with higher third and fourth stream order (Ries, 2013). Therefore, when using lower-order streams, the variation in the numerical values of the geomorphic proxies is not directly reflective of the erosion and/or rock uplift rate. Rather, this variation is more reflective of local tectonic activities.

Geomorphic proxies have been successful in investigating morphotectonic evolution of contractional tectonic regimes such as the Himalayas, the Andes, and the Alps (Keller et al., 1997; Perez-Pena et al., 2010; Daxberger and Riller, 2015). However, the application of geomorphic proxies for studying morphotectonic evolution of extensional tectonic regimes has not yet been fully explored. The East African Rift system (EARS) represents an excellent example of a continental rift system that can be used to test the usefulness of geomorphic proxies in quantifying the erosion and/or rock uplift rate as well as the drainage basin's maturity in an extensional tectonic setting. Yet, only a few morphotectonic studies have been carried out in the EARS. These studies focused on the northwestern Ethiopian Plateau (Fig. 1; Gani et al., 2007; Ismail and Abdelsalam, 2012; Gani, 2015; Molin and Corti, 2015; Sembroni et al., 2016).

In this work, we used geomorphic proxies to carry out morpho-tectonic analysis of the Rwenzori Mountains, which represent an anomalously uplifted Precambrian horst situated between the Albertine and Edward-George rifts of the western branch of the EARS (Figs. 1 and 2). Efforts have been made to investigate the cooling history, erosion rate, and climate of these mountains (Ring, 2008; Bauer et al., 2010, 2015; Roller et al., 2012; Baber, 2013). Some of these studies provided important independent constraints for the morpho-tectonic interpretation of our geomorphic proxy's results. Our objectives are to use the Rwenzori Mountains as an example of an uplifted terrain developing in association with a continental rift system exemplifying an

extensional tectonic regime to (i) evaluate the relationship between geomorphic proxies and the drainage basin's maturity as defined by the channel's longitudinal profile 'Good of Fitness' (R^2); (ii) evaluate the relationship between these geomorphic proxies and erosion rate estimated for different drainage basins of the Rwenzori Mountains using cosmogenic ^{10}Be analysis (Roller et al., 2012); (iii) evaluate the influence of the drainage basin's size and geometry, stream order, glacier extent, and local structures on the geomorphic proxy anomalies; (iv) explore the internal correlation within the areal geomorphic proxies on the one hand and the linear geomorphic proxies on the other hand; and (v) explain aspects of morpho-tectonic evolution of the Rwenzori Mountains using these geomorphic proxies.

2.2. Geologic setting

2.2.1. The East African Rift system (EARS)

The EARS represents a series of continental rift segments extending in eastern Africa (Fig.1). It can be broadly divided into a northern branch (constituting the Afar depression and the main Ethiopian Rift), an eastern branch, and a western branch (Fig. 1). The Rwenzori Mountains, the focus of this study, are located within the northern part of the western branch (Fig. 1). The western branch comprises, from north to south, the NE-trending Albertine-Rhino Rift and the Edward-George Rift, the N-trending Kivu graben, the NNW-trending Tanganyika Rift, the NW-trending Rukwa Rift, and the N-trending Malawi Rift (Figs. 1 and 2A). The western branch marks the boundary between the Nubian and the Victoria plates (Fig. 1). The Victoria plate is currently moving eastward away from the Nubian plate with a surface rift opening velocity ranging from

1.1 mm/y in the north to 2.9 mm/y in the south (Saria et al., 2014; Katumwehe et al., 2015).

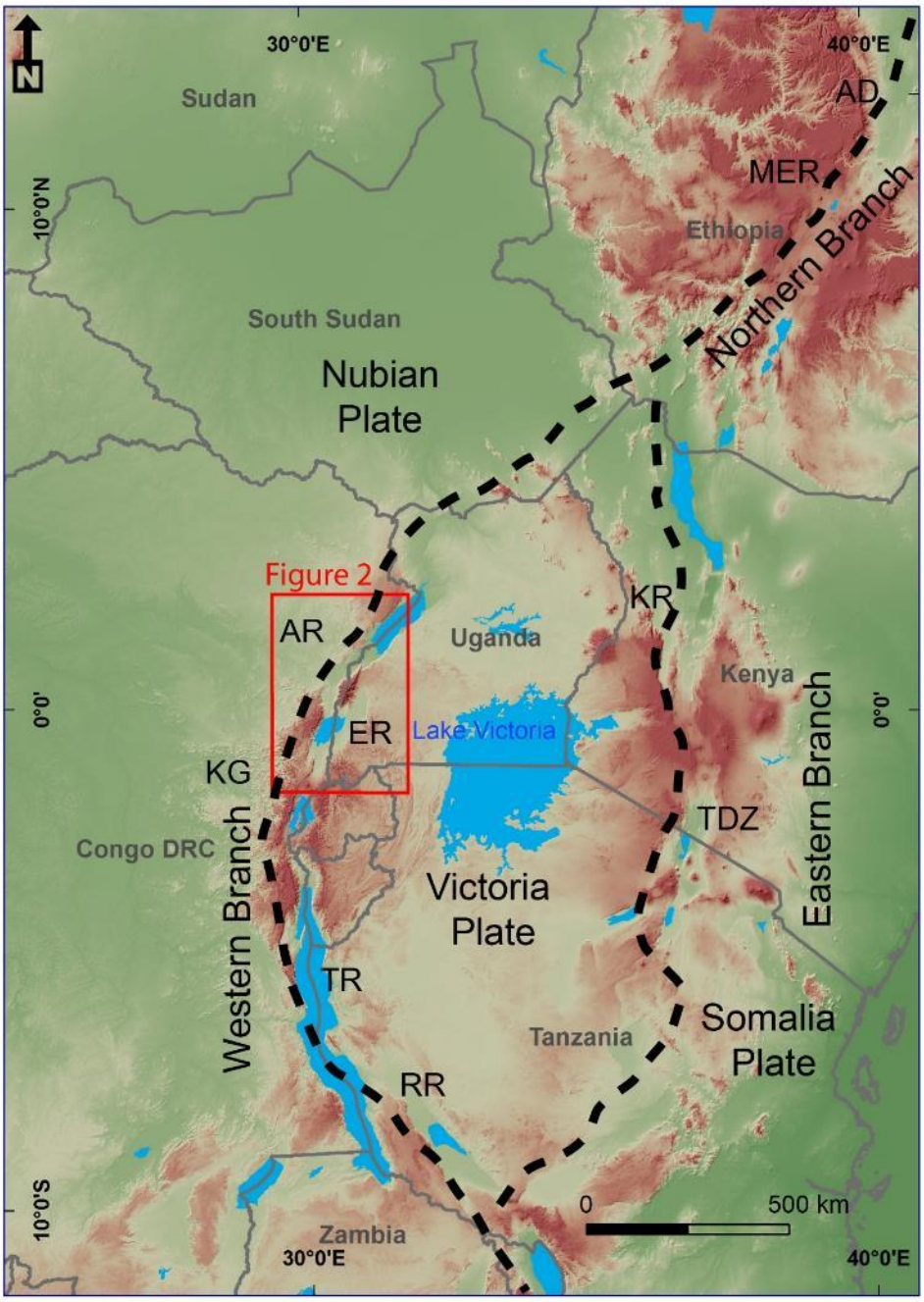

Figure 2-1 Digital elevation model (DEM) generated from the 1-km spatial resolution Global Multi-resolution Terrain Elevation Data, showing the East African Rift system (EARS) and its northern, eastern, and western branches. AD= Afar Depression. MER= Main Ethiopia Rift. KR=Kenya Rift. TDZ=Tanzania Divergent Zone. AR=Albertine and Rhino Grabens. ER=Edward-George Rift. KG=Kivu Graben. TR=Tanganyika Rift. RR=Rukwa Rift. MR=Malawi Rift.

2.2.2. The Rwenzori Mountains

The NNE-trending Rwenzori Mountains, situated at the border between Uganda and the Democratic Republic of Congo, is ~110 km long and ~50 km wide (Fig. 2A). These mountains are located at the contact between the Precambrian Kibara-Karagwe-Ankole belt and the Rwenzori belt (Nyakecho and Hagemann, 2014). It is bounded by the Cenozoic Albertine Rift in the northwest and the Edward-George Rift to the southeast (Katumwehe et al., 2015; Fig. 2B). Physiographically, the Rwenzori Mountains can be divided into a north sector, a central sector, and a south sector (Fig. 3). The margins of the long and narrow north sector are intersected by the NE-trending Ruimi-Wasa fault in the east and the Bwamba Border fault to the west (Fig. 3). The central sector yields the highest elevations (5109 m) and the widest width and forms the core of the Rwenzori Mountains (Fig. 3). Its western side is intersected by the Lamya fault (Fig. 3). The south sector is where the elevation of the Rwenzori Mountains drops steeply southward (Fig. 2A). Below we describe the lithology, tectonic uplift history, and climate and glacial history of the Rwenzori Mountains because these are factors that influence the geomorphic proxy's variation.

2.2.2.1. Lithology

The majority of the lithological units exposed in the Rwenzori Mountains are low-to high-grade metamorphic rocks of Archean–Paleoproterozoic age (Fig. 3; Ring, 2008; Bauer et al., 2010, 2012, 2013; Westerhof et al., 2014; Koehn et al., 2016). Minor Plio-Pleistocene basaltic rocks are exposed in the southern part of the mountains (Fig. 3). The Archean lithological units are made up of high-grade gneisses and migmatites that dominate the northern and southern parts of the Rwenzori Mountains. These are separated by an E-W trending belt of Paleoproterozoic amphibolite schists sandwiching Paleoproterozoic amphibolites (Fig. 3). The Paleoproterozoic amphibolite schists are also exposed in the southeastern part of the Rwenzori Mountains (Fig. 3). The Paleoproterozoic amphibolite schists and amphibolites belt that traverse the central part of the Rwenzori Mountains in an east-west direction are considered to represent a N-verging, thick-

skinned, fold-and-thrust belt—referred to as the Buganda-Toro belt (Koehn et al., 2016) and interpreted as the origin of the Paleoproterozoic amphibolites to be mafic volcanic rocks. Also, because of the stacking of the nappes from south to north, Koehn et al. (2016) found a decrease in the grade of metamorphism northward. In this graded metamorphic setting, Koehn et al. (2016) found that the Archean gneisses and Paleoproterozoic amphibolite schists in the south are metamorphosed into high-grade amphibolite facies, whereas the amphibolite schists in the north are metamorphosed into low-grade green schist facies. Also, Koehn et al. (2016) found that the Archean gneisses in the north, at the front of the N-verging nappes, are overprinted by a low-grade green schist facies metamorphic event.

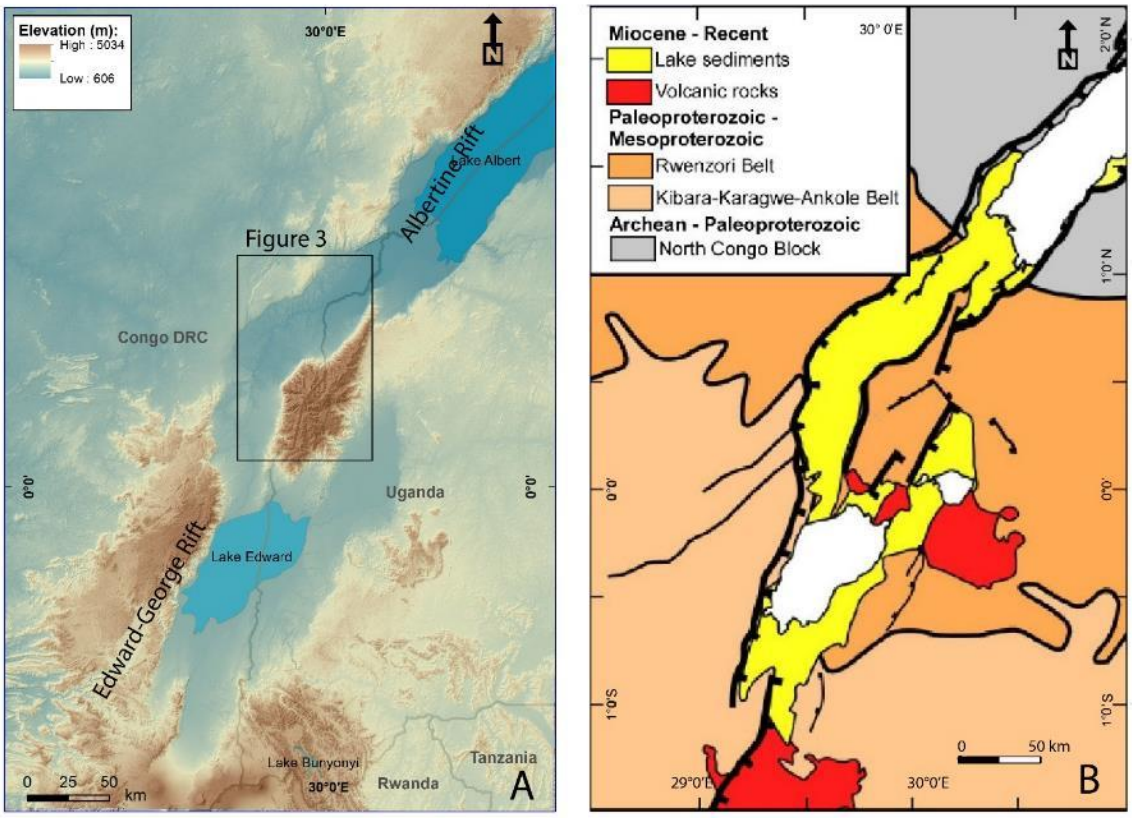

Figure 2-2(A) Digital elevation model (DEM) generated from the Advanced Spaceborne Thermal Emission and Reflection Radiometer (ASTER) data showing the Albertine Rift, the Edward-George Rifts and the Rwenzori Mountains. (B) Tectonic map of the Albertine Rift, the Edward-George Rifts and the Rwenzori Mountains, showing the dominant Precambrian units (modified from Katumwehe et al., 2015).

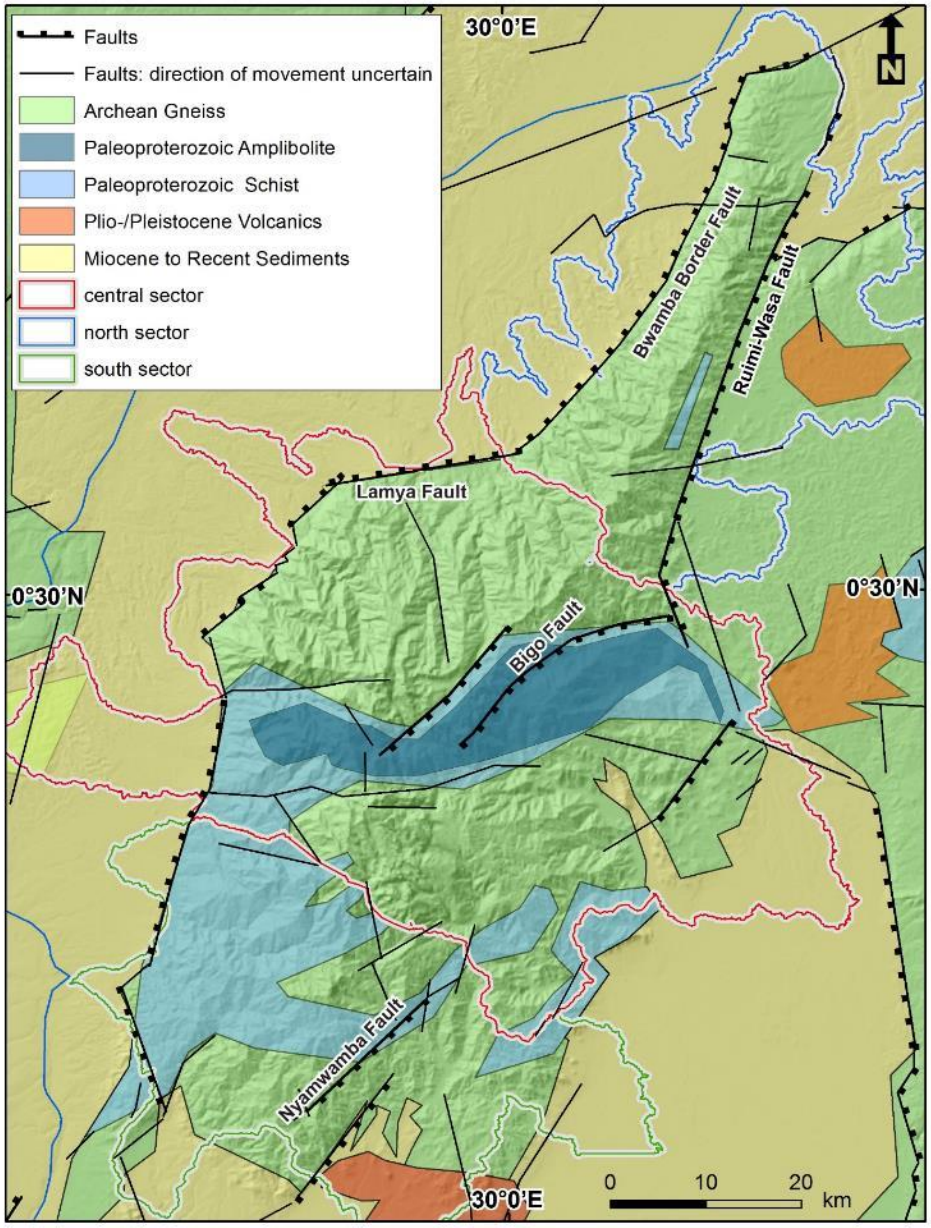

Figure 2-3 Geologic map of the Rwenzori Mountains showing major rock units and fault systems (modified from Ring, 2008; Bauer et al., 2010, 2012, 2013, 2015; Westerhof et al., 2014). The orange, blue, and pink dashed lines show the north, central, and south sectors of the Rwenzori Mountains, respectively.

Roller et al. (2012) evaluated the strength characteristics of the lithological units in the Rwenzori Mountains to quantify their level of erodibility. Roller et al. (2012) found that the Paleoproterozoic amphibolite schists of the Buganda-Toro belt that stretches in an E-W direction in the center of the Rwenzori Mountains have medium erodibility, the Archean gneisses that crop

out north and south of the Buganda-Toro belt have low erodibility, and the Paleoproterozoic amphibolites that form an E-W trending belt in the center of the Buganda-Toro belt have a very low erodibility. As such, the Precambrian bedrock formations are highly resistant to erosions, and this leads to low erosion rates by the streams within the drainage basins in the Rwenzori Mountains (Eggermont et al., 2009; Jacobs et al., 2015).

2.2.2.2. Uplift history

A number of models have been proposed to explain the unusually high elevation of the Rwenzori Mountains as a Precambrian uplifted horst structure within the Albertine and Edward-George Rift. The earliest of these models advocated for a two-phase flexural uplift of the footwall of the Albertine Rift facilitated by the rearrangement of border faults (Kusznir et al., 1995; Karner et al., 2000). This rift-flank flexural uplift mechanism accounted for ~4 km of rock uplift of the Rwenzori Mountains, hence an additional mechanism is needed to account for the remainder ~1 km elevation of the mountains (Karner et al., 2000). Glaciation erosion starting in the middle Pleistocene (which is suggested to have removed 1-2 km of geological material from the top of the Rwenzori Mountains), glacier retreat during interglacial periods, and subsequent isostatic rebound that facilitated normal faulting were called for as an explanation for the additional ~1 km rock uplift of the Rwenzori Mountains (Ring, 2008).

Alternatively, a deeper lithospheric process (referred to as 'rift-induced delamination') was introduced to explain the anomalous rock uplift of the Rwenzori Mountains (Wallner and Schmeling, 2010). In this model, it was suggested that the southward propagation of the Albertine Rift and the north propagation of the Edward-George Rift (Fig. 2) resulted in the overlapping of the two rifts at the site that became the Rwenzori Mountains. Hence, the overlapping of the two rifts triggered the delamination of subcontinental lithosphere. Removal of the sub-continental

lithospheric mantle caused reduction of the viscosity and strength of the 'Rwenzori' lower crust, allowing for a rapid uplift of the less dense 'Rwenzori' crust.

Recently, it was suggested that part of the reason for the extreme rock uplift of the Rwenzori Mountains is its position in relationship to the E-W trending Paleoproterozoic Buganda-Toro belt (Koehn et al., 2016). This study pointed to the fact that the Rwenzori Mountains are located at the northern deformation front of the Buganda-Toro belt, which is dominated by N-verging, thick-skinned nappes showing increased levels of exhumation from south to north. This study also drew attention to the fact that the south terminal tip of the Albertine Rift and the north terminal tip of the Edward-George Rift are found within the Buganda-Toro belt enclosing the Rwenzori Mountains. This work proposed that the presence of this preexisting inherited structure might have influenced rift propagation leading to the development of brittle faults that enabled significant rock uplift of the Rwenzori Mountains within the overlap zone between the two rifts.

Linking the evolution of the Rwenzori Mountains to that of the Albertine and Edward-George rifts precipitated the understanding that the rock uplift of the mountains is a relatively recent event. For example, it was proposed that Lake Albert north of the Rwenzori Mountains and Lake Edward south of it were once connected, forming a bigger paleolake that existed between 7.5 and 2.5 Ma (Van Damme and Pickford, 2003). Subsequent uplift of the Rwenzori Mountains that started at 2.5 Ma resulted in rift segmentation and the separation of the paleolake into Lake Albert and Lake Edward. However, recent low-temperature thermochronological studies revealed a more complicated exhumation and cooling history for the Rwenzori Mountains that might have started as early as Permo-Triassic (Bauer et al., 2010, 2012, 2013). Results of these studies can be summarized into (i) an early exhumation at the Permo-Triassic that might be related to the beginning of the fragmentation of supercontinent Pangaea and possibly the formation of the Karoo basins. (ii) A rapid exhumation in the Middle to Upper Jurassic that might have produced positive topography as high as ~1500 m in the absence of erosion rates high enough to balance

the high rock uplift rates. The possible positive topography formed during this phase is referred to as the 'Mesozoic Albertine high' (Bauer et al., 2013). (iii) A phase where fault-controlled low differential topography was formed during the Cretaceous and Paleogene because the rock uplift phase might have been slightly higher than the erosion rates. (iv) An accelerated Neogene age exhumation that resulted in the formation of low relief because rock uplift rates was slightly higher than erosion rates. This phase might be associated with the onset of the Albertine and Edward-George rifts. (v) A final phase of accelerated rock uplift that produced the modern topography of the Rwenzori Mountains because the uplift rates are much higher than can be compensated by the erosion rates.

Results of low-temperature thermochronological studies also show that the rock uplift in the Rwenzori Mountains was not uniform and that the western flank of the mountains might have witnessed a higher level of rock uplift compared to their eastern flank (Bauer et al., 2013). It is also shown that different blocks within the central sector of the Rwenzori Mountains witnessed rock uplift at distinctively different times (Bauer et al., 2013). This study showed the presence of a NW-trending fault in the central sector of the Rwenzori Mountains separating a northeastern block that gave an apatite fission track age of ~130 Ma from a southeastern block that gave an age of ~300 Ma.

2.2.2.3. Precipitation and glaciers

Precipitation in the Rwenzori Mountains is controlled by the movement of the Inter Tropical Convergence Zone (ITCZ) and the orographic effect from the height of the mountains (Taylor et al., 2009). Movement of the ITCZ controls the seasonal variation in precipitation that is characterized by March-May and August-November rainy seasons (Taylor et al., 2009). The orographic effect is reflected in the general increase in mean annual precipitation from the foot of the Rwenzori Mountains to the middle-higher altitude (~3000 m) of the mountains. This generally

is shown by 1998 to 2009 annual rainfall received by the Rwenzori Mountains from Tropical Rainfall Measuring Mission (TRMM) data (Fig. 4). The orographic effect is also demonstrated from in situ measurements between 1964 and 1995 showing mean annual precipitation of 1540 mm at ~1370 m elevation that drops to 890 mm at ~960 m elevation (Taylor et al., 2009). Available precipitation data are scarce for the Rwenzori Mountains at elevations higher than ~1370 m. It is observed from data collected between 1951 and 1954 in four stations that the mean annual precipitation increases from 1150 mm at ~1250 m elevation to 2500 mm at 3290 m elevation (Osmaston, 1989).

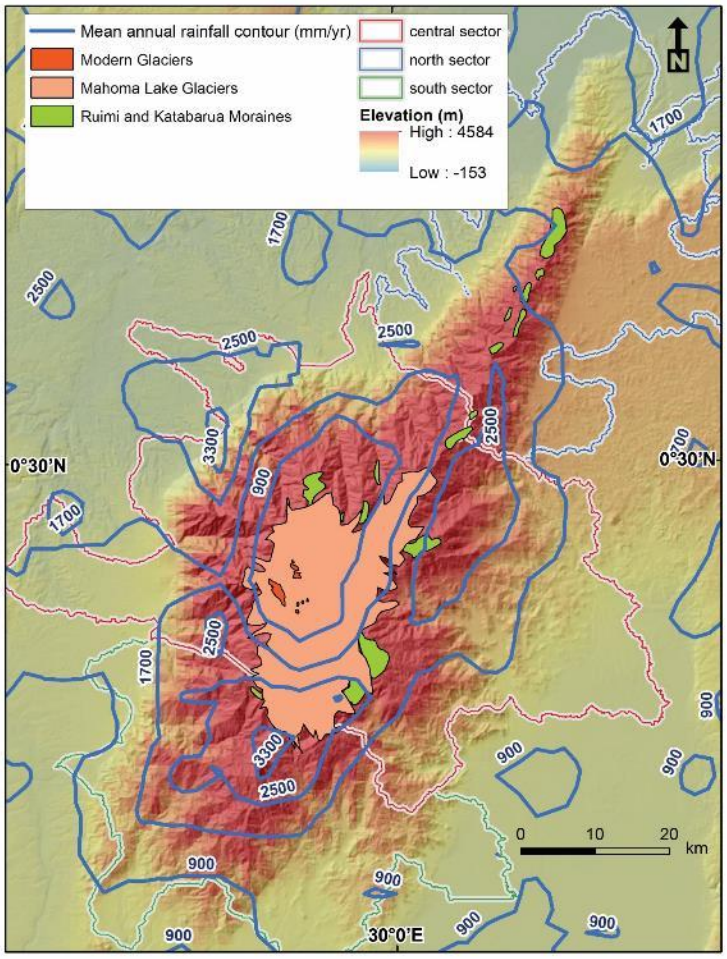

Figure 2-4 Contour map of the 1998 to 2009 annual rainfall received by the Rwenzori Mountains from the Tropical Rainfall Measuring Mission (TRMM) data. The red, pink, and green polygons illustrate the maximum extent of modern glaciers, Mahoma Lake glaciers, and Ruimi and Katabarua moraines, respectively (modefied after Kaser and Osmaston, 2002; Ring, 2008; Roller et al., 2012).

At present, Mount Stanley, the highest peak in the Rwenzori Mountains, is covered by 0.5 km^2 of permanent snow (Fig. 4; Kaufmann and Romanov, 2012). However, in the past the topography of the Rwenzori Mountains was carved by several glacial events starting in the middle Pleistocene (Kaser and Noggler, 1991; Kaser and Osmaston, 2002). The last three glacial maxima referred to as the Katabarua, the Rwimi Basin, and the Mahoma Lake glaciers (Fig. 4) occurred ~300, ~100, and 23-20 ky ago, respectively (Kaser and Osmaston, 2002; Ring, 2008; Kelly et al., 2014). The two oldest stages, the Katabarua and the Rwimi Basin glaciers, are suggested to have occurred before the last ice age (Osmaston, 1989). The Rwimi Basin glacier is characterized by the development of U-shaped valleys; while the Katabarua glacier is marked by large, eroded terminal moraines covering ~500 km^2 (Osmaston, 1989). The Mahoma Lake glacier is defined by prominent lateral moraines extending down to 2070 m elevation for the peak of the Rwenzori Mountains (Fig. 4: Kelly et al., 2014). These moraines define the maximum extent (260 km^2) of the Rwenzori glaciers at the end of the last glacial period before the ice cap started to retreat (Baber, 2013). Because of the tilt of the Rwenzori Mountain, the moraines on the eastern flank are found at a lower altitude compared to the moraines of similar size on the western flank of the mountains (Ring, 2008). The tilted morphology of the Rwenzori Mountains is reported to have started developing as a result of glacial rebound starting in the middle Pleistocene (Kaser

and Osmaston, 2002; Ring, 2008).

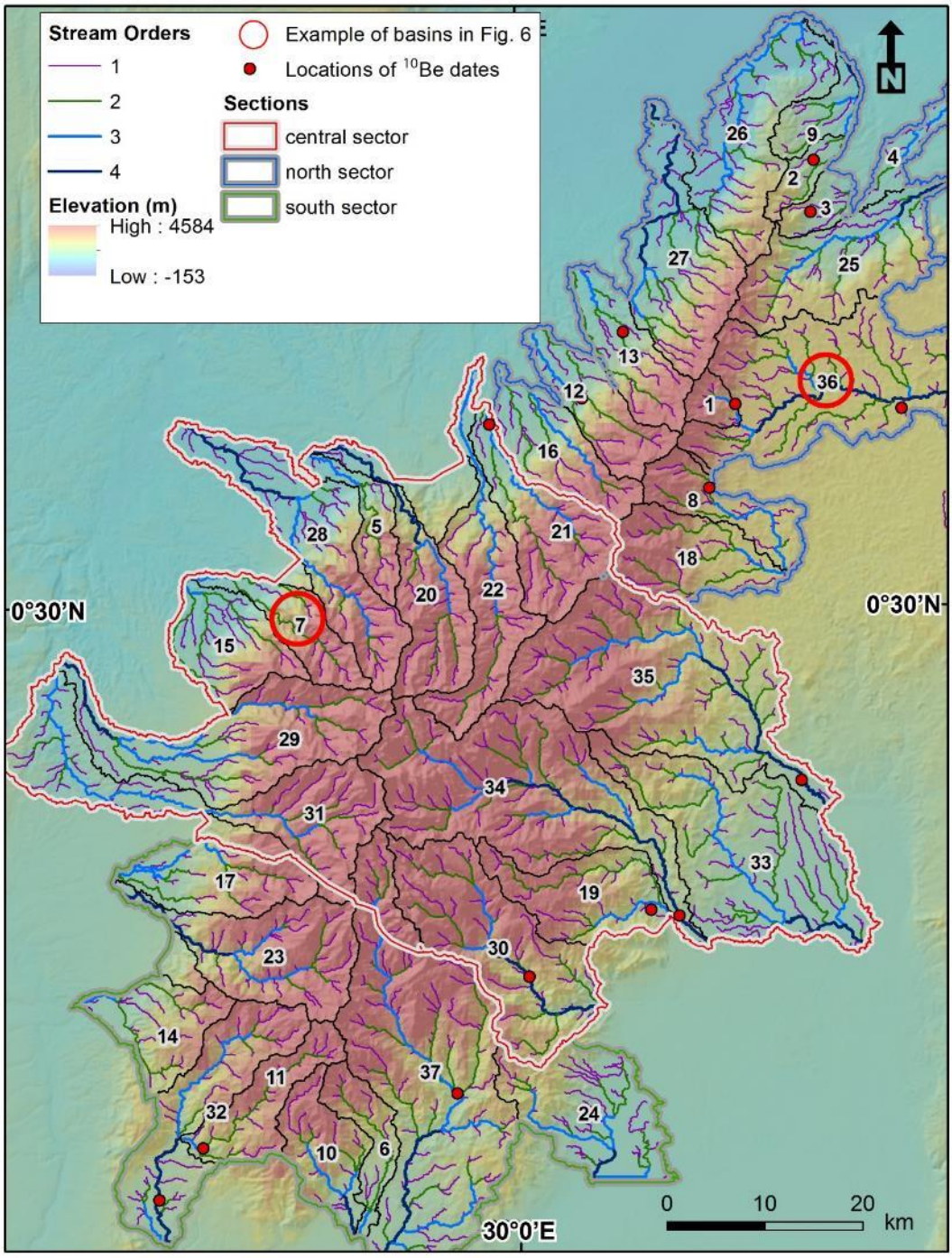

Figure 2-5 Advanced Spaceborne Thermal Emission and Reflection Radiometer (ASTER) digital elevation model (DEM) (30-m spatial resolution) of the Rwenzori Mountains showing spatial distribution of 40 basins and the stream orders. The stream orders are labelled from1 to 4 based on Strahler (1952). The locations of cosmogenic 10Be analysis (Roller et al., 2012) are marked by solid red dots. The open red circles indicate the drainage basins used for the examples of knickpoint analysis shown in Fig. 6.

2.3. Data and methods

Morphotectonic analysis was performed on 37 representative drainage basins with first to fourth stream order, which covers 92% of the total surface area of the Rwenzori Mountains (Fig. 5). To ensure similar discharge, the drainage basins were chosen to be confined to those containing channels with third and fourth stream order. These drainage basins are identified with serial numbers ranging from 1 to 37 based on the size of the basin. The smallest size drainage basin (23 km^2) is given the number 1, and the number 37 is assigned to the largest basin (448 km^2). To compute the geomorphic proxies, we used a DEM extracted from the 30-m spatial resolution ASTER data. Sinks and depressions were removed from the DEM, and lakes were leveled before the extraction of the geomorphic proxies. We also used erosion rates measured using cosmogenic ^{10}Be analysis for 16 samples collected from perennial streams on the Ugandan side of the Rwenzori Mountains (Roller et al., 2012; Fig. 5).

Table 1 Summary of areal and linear geomorphic proxies and their applications used in this study

	Proxies	Application	References
Areal and relief proxies	Asymmetry factor (AF)	AF is suggested to quantify and compare the amount of tilted area on both sides of the main stream within the entire drainage basin	Silva et al., 2003; Ries, 2013
	Mountain front sinuosity (S_{mf})	Tectonically active mountain front preserves a low S_{mf} value regardless of lithology, whereas inactive mountain fronts are characterized by high sinuosity values	Silva et al., 2003
	Hypsometric integral (HI)	Hypsometric analysis can differentiate erosional landforms at progressive stages and can be positively correlated to uplift rate	Perez-Pena et al., 2009a
	Relief	Geophysical relief has been applied to reconstruct paleodatum surfaces to quantify the volume of eroded rocks and to evaluate the isostatic rebound from erosion	Small and Anderson, 1998; Barcos et al., 2014
	Shape factor (Shp)	Shp describes the shape of the drainage basin and maturity of the landscape	Nexer et al., 2015
Linear proxies	Normalized steepness (k_{sn})	*ksn* is proportional to the local erosion rate for the steady-state basins when bedrock lithology and climate are steady	Kirby and Whipple, 2012
	Length-gradient index (SLk)	SLk has been applied to quantify tectonic forcing in drainage basins; specifically, high SLk values are associated with large erosion/uplift rate assuming uniform climate and lithology	Chen et al., 2003; Kobor and Roering, 2004
	Integral proxy chi (χ) and gradient chi ($M\chi$)	χ values for the streams sharing the same divide suggest the movement direction of the divide; the $M\chi$ values reflect uplift rate in steady-state	Mudd et al., 2014; Willett et al., 2014

The geomorphic proxies extracted from the ASTER DEM are classified into areal proxies and linear proxies (Table 1). The areal geomorphic proxies describe the general characteristics of the drainage basin and provide an overview of the basin's extent, shape, and relief. These geomorphic proxies are commonly used to assess the drainage basin's maturity and equilibrium stages (Perez-Pena et al., 2009b; Nexer et al., 2015). These geomorphic proxies include AF, S_{mf}, HI, geophysical relief, and Shp. The linear geomorphic proxies including k_{sn}, SLk, Mχ are derived from the stream's longitudinal profiles. These have been suggested to be proportional to local erosion and/or rock uplift rate in certain tectonic settings (Montgomery and Brandon, 2002; Wobus et al., 2006; Kirby and Whipple, 2012).

To evaluate the geomorphic proxies, we first extracted areal proxies for the drainage basins in the Rwenzori Mountains and linear proxies for the major streams within these drainage basins. Subsequently, using R^2 as a measure of the drainage basin maturity, we correlated the areal geomorphic proxies with R^2 in terms of spatial distribution and magnitude. For the linear geomorphic proxies, we compared their magnitude and distribution pattern with the erosion rates obtained from cosmogenic ^{10}Be analysis (Roller et al., 2012). We did not compare the areal geomorphic proxies (with the exception of geophysical relief) to erosion rates because the samples used in the cosmogenic ^{10}Be analysis are from individual streams, hence they are not representative of the erosion rates of the entire drainage basin. We compared the geophysical relief to erosion rates because this geomorphic proxy measures the minimum amount of bedrock incision of streams—a parameter that can be correlated to erosion rate. Finally, we used matrix scatter plots to examine the internal relationship between the areal geomorphic proxies on the one hand and the linear geomorphic proxies on the other hand.

2.3.1. Drainage basin's maturity

To investigate the relationship between the areal geomorphic proxies and drainage basin's maturity, we evaluated the longitudinal profiles of 75 third order streams within the drainage basins of the Rwenzori Mountains. Knickpoints along the stream's longitudinal profiles can be used to define the transient response of the stream to variation in lithology, climate, and rock uplift and/or subsidence (Kirby et al., 2003; Pedrera et al., 2009; Pederson and Tressler, 2012). The location of knickpoints records a perturbation event where the upstream retains the characteristics of the preexisting state and where the downstream is adjusted to a new state (Kirby and Whipple, 2012). The idealized stream's longitudinal profile at a dynamic equilibrium stage is described by the empirical power-law equation (Hack, 1973; Flint, 1974):

$$S = k_s A^{-\theta} \quad (1)$$

where k_s is the steepness index, A is the basin's drainage area, and θ is the concavity.

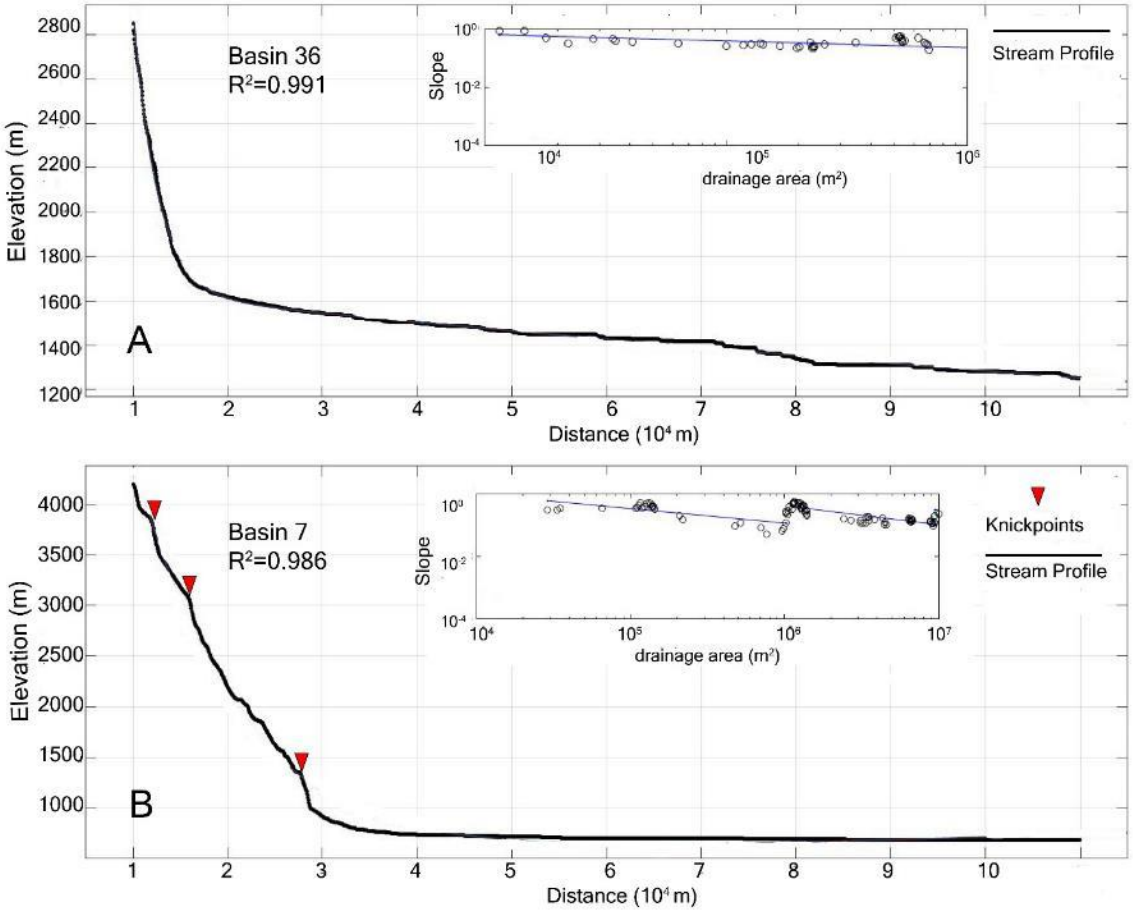

Figure 2-6 Longitudinal stream profiles of the mean streams in basins 6 (A) and 7 (B) of the Rwenzori Mountains. See drainage basin locations in Fig. 5. Insert graphs show slope-area relationships of the two streams. When the stream is in an equilibrium stage, its slope-area profile tends to have a linear fit and a high 'Good of Fitness' (R2) value to the concave longitudinal profile as the main stream profile of basin 36. When the stream's longitudinal profile is modified by external forces, knickpoint migration will start from downstream to upstream as a transient response, resulting in the interruption of the linear fit in slope-area profile and a low R2 value as in the case of the main stream longitudinal profile of basin 7.

When the stream is in equilibrium stage, its longitudinal profile will have a concave shape and the slope-area profile tends to have a linear fit. As a transient response, if the stream is modified by external factors, knickpoint migration will start from downstream to upstream. This will result in the disruption of the linear fit of the slope-area profile and change the stream's longitudinal profile into a convex shape (Whipple and Tucker, 1999; Snyder et al., 2000; Duvall et al., 2004). In this case, R^2 values will be reflective of the equilibrium and maturity of the

stream and its associated drainage basin (Ismail and Abdelsalam, 2012). For example, the longitudinal profiles in Figs 6A and B are extracted from the main streams in basins 36 and 7, respectively (Fig. 5). The stream in basin 36 is relatively closer to steady-state condition compared to the stream in basin 7. This is because the first stream has an R^2 value of 0.991, whereas the second stream has an R^2 value of 0.986. A higher R^2 value of a stream's longitudinal profile indicates a higher level of maturity and the approach of equilibrium state. Therefore, high R^2 values calculated for the majority of the stream's longitudinal profiles in a given drainage basin compared to another basin indicate that this basin is closer to reaching the equilibrium state. Thus, we interpolated using kriging the R^2 values calculated for the 75 third-order streams from the ASTER DEMs to construct a maturity index map for the drainage basins in the Rwenzori

Mountains (Fig. 7).

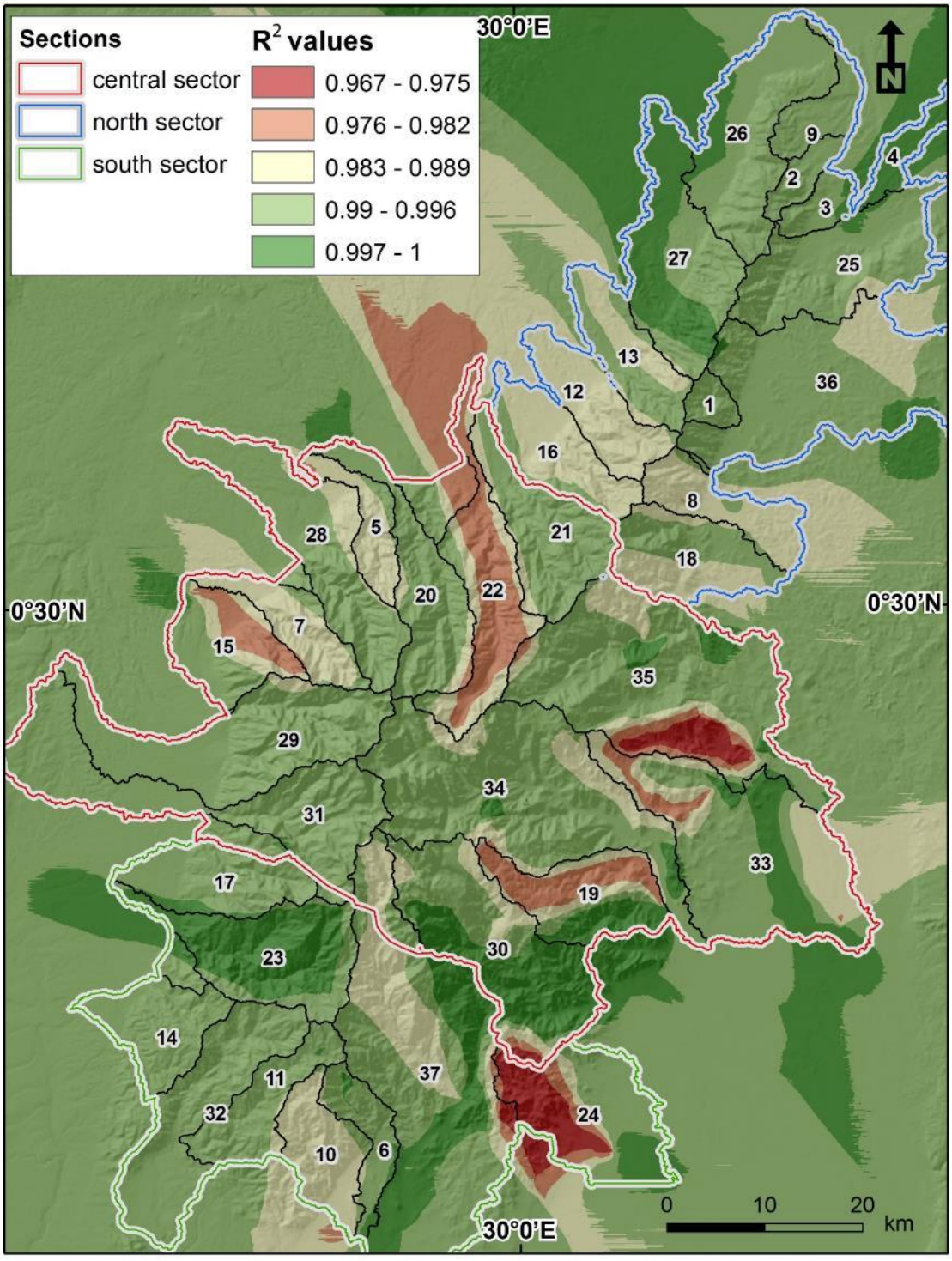

Figure 2-7 Drainage basin maturity map interpolated from the 'Good of Fitness' (R2) values of 75 third order streams in the Rwenzori Mountains. The green color represents mature drainage basins, while the red color reflects an unstable stage of the basins influenced by tectonics and climate.

2.3.2. Aerial geomorphic proxies

2.3.2.1. Asymmetry factor (AF)

Generally, streams flowing on homogenous lithological units that are not experiencing rock uplift are symmetrical and exhibit a dendritic drainage pattern (Schumm et al., 2002). Thus, the effect of rock uplift that results in tilting of the lithological units is preserved in the form of asymmetry of the drainage network of the basin. Regional-scale tectonic tilting causes asymmetry in the higher-order streams, whereas local faulting results in asymmetry in the lower-order streams (Ries, 2013). Also, asymmetry recorded in a stream is more obvious when the tilting is near perpendicular to the flow direction of the stream. Therefore, the AF can be used to quantify the amount of tilting experienced by a given drainage basin (Hare and Gardner, 1985; Keller et al., 1997; Perez-Pena et al., 2010). The AF is computed using the following equation:

$$\mathrm{AF} = \left| \frac{\mathrm{A_R}}{\mathrm{A_T}} * 100 - 50 \right| \quad (2)$$

where A_R is the basin's drainage area to the right of the main stream (looking downstream), and A_T is the basin's total drainage area.

2.3.2.2. Mountain front sinuosity (S_{mf})

The S_{mf} is used to evaluate tectonic activities, specifically in mountain front zones (Bull, 1976, 2008; Keller et al., 1997; Silva et al., 2003). The S_{mf} is expressed as:

$$\mathrm{S_{mf}} = \frac{\mathrm{L_{mf}}}{\mathrm{L_s}} \quad (3)$$

where L_{mf} is the length of the mountain front along the foot of the mountain, and L_s is the length of the mountain front measured along a straight line.

Straight mountain fronts are characteristics of zones where rock uplift rates exceed erosion rates. When the rock uplift decreases or ceases, continued erosion will produce sinuous

mountain fronts. Hence, regardless of lithological variation, tectonically active mountain fronts will have low S_{mf} values, whereas inactive mountain fronts are characterized by relatively high S_{mf} values because the retreating erosion will dominate the mountain front (Keller and Pinter, 2002; Perez-Pena et al., 2010; Giaconia et al., 2012; Mahmood and Gloaguen, 2012; Daxberger and Riller, 2015).

2.3.2.3. Hypsometric curve and hypsometric integral (HI) index

Hypsometric analysis describes the distribution of land surfaces at different elevations within a drainage basin by comparing their relative height and relative area (Strahler, 1952). The relative height is defined as the ratio between the height of a specific elevation within the drainage basin and the difference in elevation between the highest and lowest point in that basin. The relative area is defined as the ratio between the area of a horizontal plane at a given elevation within the drainage basin and the area of the entire drainage basin (Strahler, 1952). The shape of the hypsometric curve reflects the geomorphic development of the drainage basin and its stage of maturity. Drainage basins in a disequilibrium stage tend to have convex hypsometric curves, whereas mature and in equilibrium stage drainage basins have S-shape hypsometric curves (convex at high elevations and concave at low elevations; Strahler, 1952; Keller et al., 1997). Cheng et al. (2012) suggested that the shape of the hypsometric curves can be correlated with the drainage basin maturity and tectonic activities within 0.5 to 2.0 Ma time span.

The HI is an attribute of the hypsometric curve that can be considered as the proportions of the volume of horizontal slabs at a given thickness interval (h; Strahler, 1952). It can be expressed as

$$\mathrm{HI} = \int_{\text{Min el.}}^{\text{Max el.}} \mathrm{A}\ \mathrm{dh} \tag{4}$$

where A is the relative area in the drainage basin, and Max el. and Min el. are the maximum and the minimum elevation of the basin, respectively. The dh is the delta height.

Strahler (1952) suggested that HI values < 0.3 represent stable, mature, and in equilibrium drainage basins and that proposed that HI values > 0.6 are associated with unstable, immature drainage basins that are in a disequilibrium stage. Hence, the hypsometric analysis can differentiate between erosional landforms at progressively different equilibrium stages and can be positively correlated with the rates of rock uplift. Therefore, this geomorphic proxy has been widely used in morphotectonic analysis of tectonically active regions (Lifton and Chase, 1992; Ohmori, 1993; Chen et al., 2003). We used CalHypso ArcGIS extension (Perez-Pena et al., 2009a) to extract the hypsometric curves from the ASTER DEM and to calculate the HI for the 37 drainage basins in the Rwenzori Mountains (Fig. 10).

2.3.2.4. Geophysical relief

The evolution of relief records the relationship between rock uplift and erosion (Molnar, 2009). Geomorphic proxies based on relief evolution can be divided into local relief and geophysical relief (Champagnac et al., 2014; Nexer et al., 2015). Local relief infers the elevation difference between the envelope surface (an imaginary topographic surface constructed by ridges, peaks, or high-elevated surfaces) and the stream network or any specific points of low elevation such as valley bottoms (Ahnert, 1970; Champagnac et al., 2014; Nexer et al., 2015). Differently, geophysical relief is defined by the difference in elevation between the envelope surface and present-day topography (Small and Anderson, 1998; Champagnac et al., 2014; Nexer et al., 2015). Additionally, in contrast to local relief, geophysical relief considers the entire drainage basin as a low elevation surface rather than low elevation points. Geophysical relief has been applied to reconstruct paleodatum surfaces to quantify the volume of eroded geological material and to evaluate the isostatic rebound from erosion (Clark et al., 2006; Gani et al., 2007; Sternai et al., 2012; Champagnac et al., 2014).

We constructed the geophysical relief to estimate the minimum incision of bedrock streams in the Rwenzori Mountains since the initial time of the exhumation of the mountains. Initial exhumation of the Rwenzori Mountains might have started as early as the Paleozoic (Bauer et al., 2012). Using ArcGIS, we identified and extracted isolated erosional remnants in the Precambrian bedrock units based on the 1:1,000,000 geological map of Uganda (Westerhof et al., 2014) as well as other published data (Ring, 2008; Roller et al., 2012; Bauer et al., 2013). To avoid using remnants of different erodibility, the relief formed by Cenozoic volcanism in the south sector of the Rwenzori Mountains is excluded. We interpolated the remnants using the nearest neighbor algorithm to construct a composite paleodatum that represents the minimum elevation before the exhumation of the Rwenzori Mountains. Subsequently, we constructed the geophysical relief map by subtracting the modern topographic surface from the composite paleodatum surface (Fig. 11).

2.3.2.5. Shape factor (Shp)

The shape of the drainage basin directly controls the water supply to the main stream and therefore provides hydrological information about the basin's dynamics. Shp, also known as the elongation ratio, describes the shape of the drainage basin and the maturity of the landscape (Bull and McFadden, 1977; Kale and Shejwalkar, 2008). Drainage basins that are influenced by tectonic activities generally are more elongated in shape. On the other hand, circular-shaped drainage basins often are developed during tectonic quiescence (Bull and McFadden, 1977). Shp is calculated as follows:

$$\mathrm{Shp} = \frac{\sqrt{\mathrm{A}}}{\mathrm{d}} \tag{5}$$

where A is the basin's drainage area, and d is the diameter of the basin (maximum distance between two points on the basin's edge; Bull and McFadden, 1977; Nexer et al., 2015).

2.3.3. Linear geomorphic proxies

2.3.3.1. Normalized steepness (k_{sn})

As defined in Eq. (1), the power law relationship between the stream's slope and the basin's drainage area can be empirically supported (Flint, 1974; Wobus et al., 2006). The k_s is commonly normalized to a reference θ. However, using different θ values for the stream's longitudinal profiles result in large differences in the calculated k_s. In this work, we used a θ_{ref} value of 0.45 as recommended by Whipple (2004), which produced reliable results in the northwestern Ethiopian Plateau (Ismail and Abdelsalam, 2012). k_{sn} and θ are determined through regression of the stream's slope and the basin's drainage area.

We used the stream profiler tool (Kirby et al., 2003) in ArcGIS to extract the slope-area profiles and k_{sn} from the ASTER DEM for the main streams within the drainage basins in the Rwenzori Mountains. Subsequently, we interpolated the k_{sn} values using kriging to construct a k_{sn} anomaly map for the drainage basins of the Rwenzori Mountains (Fig. 13).

2.3.3.2. Length-gradient index (SLk)

SLk is a geomorphic proxy that highlights a stream's power by calculating the gradient changes along the stream's longitudinal profile (Hack, 1973). Length-gradient, SL, is calculated using the equation

$$SL = \frac{dH}{dL} L \quad (6)$$

where L is the total length of the stream, and dH/dL is the local stream gradient.

SL remains constant when the drainage basin is in an equilibrium state (Hack, 1973). The gradient of the stream is formed by differential shear stress or stream power, which can be affected by factors such as tectonic activities, lithological variation, and climate change (Keller et al., 1997; Burbank and Anderson, 2011). Thus, assuming no lithological variation and no change in the climate, SL is often used to identify the effect of tectonic activities in disrupting the

equilibrium state of the stream. SL is highly dependent on the stream's length. This is because longer streams are capable of adjusting their longitudinal profiles more rapidly than shorter streams (Chen et al., 2003). Hence, to minimize the effect of stream length on the computation of SL and to be able to compare values from different drainage basins, SL is usually modified to SLk. This is achieved by normalizing SL by the term k, which represents the graded gradient of the stream's longitudinal profile in the equilibrium stage (Chen et al., 2003; Perez-Pena et al., 2009b). Hence, k can be expressed as

$$K = \frac{C - h_m}{\ln L_t} \quad (7)$$

where C is the elevation of the highest point at the upstream, h_m is the elevation at the mouth of the stream, and L_t is the entire length of the stream.

SLk has been applied to quantify rock uplift in drainage basins in different regions around the world (Goldrick and Bishop, 2007; Perez-Pena et al., 2009b; Barcos et al., 2014; Dominguez-Gonzalez et al., 2015). In such analysis, assuming no change in climate and homogeneous bedrock lithology, high SLk values are associated with high rates of erosion and rock uplift (Keller et al., 1997; Chen et al., 2003). On the other hand, low SLk values suggest that the drainage basin is not witnessing tectonic activities.

We used ArcGIS to extract the SLk for the main streams within the drainage basins in the Rwenzori Mountains from the ASTER DEM at 150 m equal spacing. Subsequently, we extrapolated these values using kriging to develop an SLk anomaly map for the drainage basins in the Rwenzori Mountains (Fig. 14).

2.3.3.3. Chi analysis (Mχ)

An integral geomorphic proxy, referred to as χ, is reported to be useful in characterizing the geometry of the drainage basin and its dynamic state (Perron and Royden, 2013; Willett et al., 2014). At steady state, Eq. (1) can also be expressed as

$$S = \frac{dz}{dx} = (\frac{E}{K})^{\frac{1}{n}} A^{\frac{-m}{n}} \quad (8)$$

where S is the stream's local gradient, A is the basin's drainage area, z is the elevation of the stream, x is the longitudinal coordinate (the distance from the head of the stream to the location along the longitudinal profile with a specific z value), E is the bedrock erosion rate, K is the erosion coefficient, and m and n are empirical constants (Whipple and Tucker, 1999). χ can be computed by integrating both sides of Eq. (8):

$$z(x) = z_b + (\frac{E}{K A_0^m})^{\frac{1}{n}} \boldsymbol{\chi} \quad (9a)$$

$$\chi = \int_{x_b}^{x} (\frac{A_0}{A(x)})^{\frac{m}{n}} dx \quad (9b)$$

$$M\chi = (\frac{E}{K A_0^m})^{\frac{1}{n}} \quad (9c)$$

where z_b is the elevation at the mouth of the drainage basin, and A_0 is a reference drainage area (Perron and Royden, 2013).

Given the linear form of Eq. (9a), χ predicts an elevation for the stream's steady state at location x (Willett et al., 2014). Therefore, different χ values across a divide in a constant rock uplift suggest motion of the divide from a high χ value toward a low χ value (Willett et al., 2014). Mχ, often referred to as the gradient in χ space, proportionally reflects the erosion rate at constant precipitation and uniform bedrock lithology (Struth et al., 2015; Yang et al., 2015).

We computed Mχ for the main streams within the drainage basins in the Rwenzori Mountains from the ASTER DEM using the code of Mudd et al. (2014) and Perron and Royden (2013). To acquire the best fit for the m/n ratio, we carried out AICc-collinearity tests, a modified version of Akaike's information criterion, following the method of Mudd et al. (2014). We determined the uniform m/n ratio as 0.4, and we applied this to all main streams within the drainage basins in the Rwenzori Mountains (Fig. 15).

2.4. Results

2.4.1. Areal geomorphic proxies

2.4.1.1. Asymmetry factor (AF)

We found that the AF values for the drainage basins in the Rwenzori Mountains range between 0.4 and 34.8. We divided the basins into symmetrical ones where AF values are < 12.0, moderately asymmetrical ones where AF values are between 12.1 and 20.0, and highly asymmetrical where AF values are > 20.1 (Fig. 8). (i) The symmetrical drainage basins with AF values ≤ 12 are mostly found in the central sector (basins 5, 20, 22, 30, 31, 33, 34, and 35). This suggests that the drainage basins in the central sector of the Rwenzori Mountains did not witness significant tilting. (ii) The moderately asymmetrical drainage basins with AF values between 12.1 and 20 are mostly located in the north sector (basins 1, 25, 26, 27, and 36), with a few in the central sector (basin 28) and south sector (basins 10 and 37). (iii) The highly asymmetrical drainage basins with AF values > 20 are scattered all over the Rwenzori Mountains, including the north sector (basins 2, 3, and 9), the central sector (basins 15, 19, 21, and 29), and the south sector (basins 11, 14, 17, 24, and 32). This suggests random tilting of the drainage basins throughout the

Rwenzori Mountains.

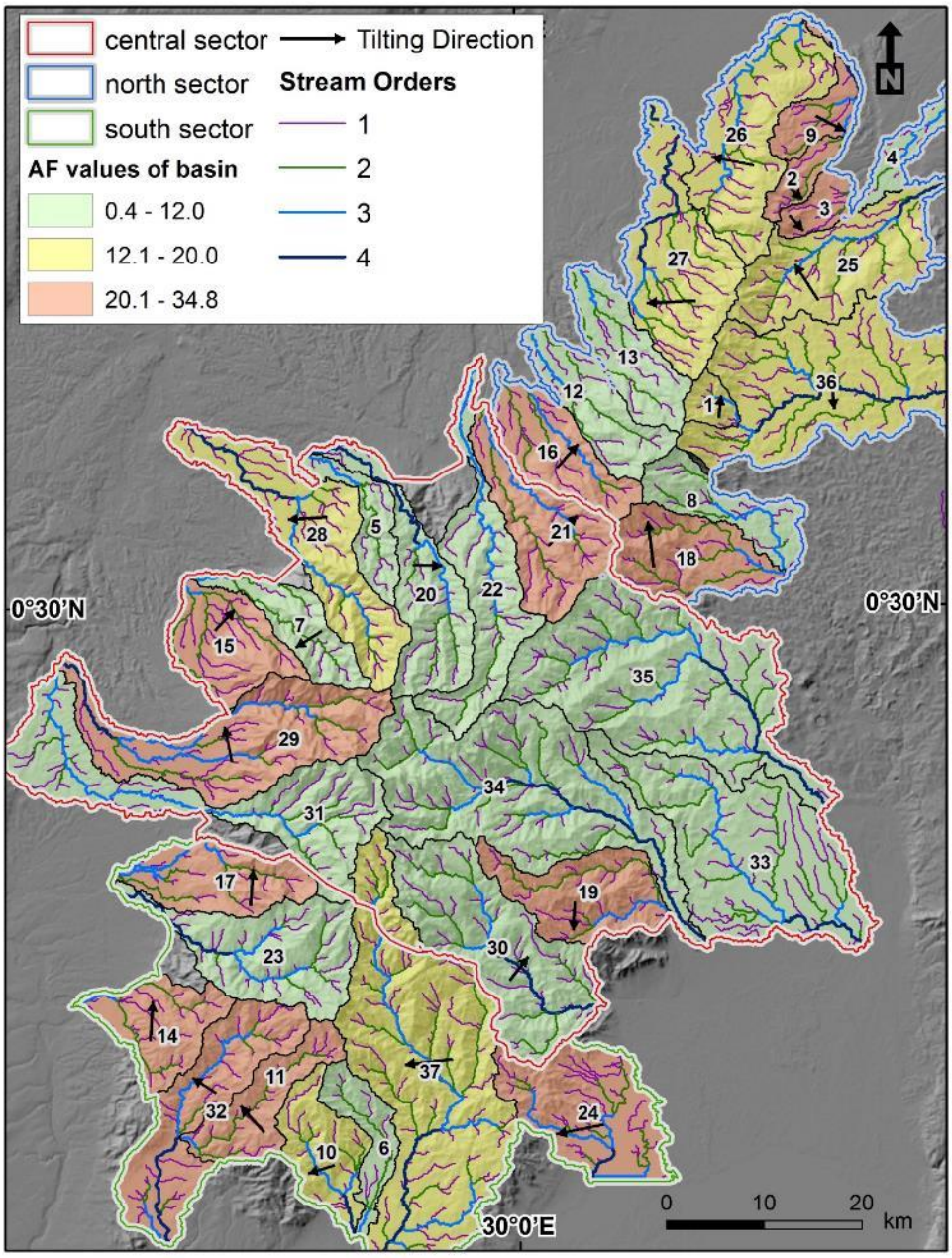

Figure 2-8 Asymmetric factor (AF) and tilting map of the drainage basins in the Rwenzori Mountains. The AF values are classified into three categories into 0.4-12 (symmetrical basins), 12.1-20 (moderately asymmetrical basins), and 20.1-34.8 (highly asymmetrical basins) symmetric, asymmetric, and highly tilted, respectively.

2.4.1.2. Mountain front sinuosity (S_{mf})

We found that the S_{mf} values of the drainage basins in the Rwenzori Mountains range between 0.00 and 2.33 (Fig. 9). We classified the S_{mf} values as high when they are > 1.22, as moderate when they are between 1.09 and 1.21, and as low when they are < 1.08 (Fig. 9). Bull (2008) considered S_{mf} values to be low when they are < 1.4 and moderate when they are between 1.4 and 3. It is suggested that low and moderate S_{mf} values are indicative of mountain fronts witnessing a high level of tectonic activities (Keller and Pinter, 2002; Perez-Pena et al., 2010; Giaconia et al., 2012; Mahmood and Gloaguen, 2012; Daxberger and Riller, 2015). The majority of the drainage basins in the Rwenzori Mountains have S_{mf} values < 1.4. However, some drainage basins including basins 2 and 9 in the north sector; basins 22, 30, 33, 34, and 35 in the central sector; and basins 6, 11, 24, 32, and 37 in the south sector have S_{mf} values > 1.4. Nonetheless, none of the drainage basins in the Rwenzori Mountains have S_{mf} values > 3 — an S_{mf} value range that is considered to be indicative of significant range-ward erosion and limited fault activities (Daxberger and Riller, 2015). Moreover, the distribution of the drainage basins of the Rwenzori Mountains with low S_{mf} values coincides with the location of regional faults. The drainage basins with anomalously low S_{mf} values in the north sector are intersected by the Ruimi-Wasa fault in the east and the Bwamba Border fault to the west (Fig. 9). Additionally, basins 5 and 20 (which have low S_{mf} values in the central sector) are intersected by the Lamya fault. Moreover, basin 10 (which is intersected by the Naymawamba Fault in the south sector) also has a low S_{mf} value. Further, almost all drainage basins on the western side of the central and southern sectors have S_{mf} values < 1.4, and these basins are intersected by the southern continuation of the Lamya fault (Fig. 9).

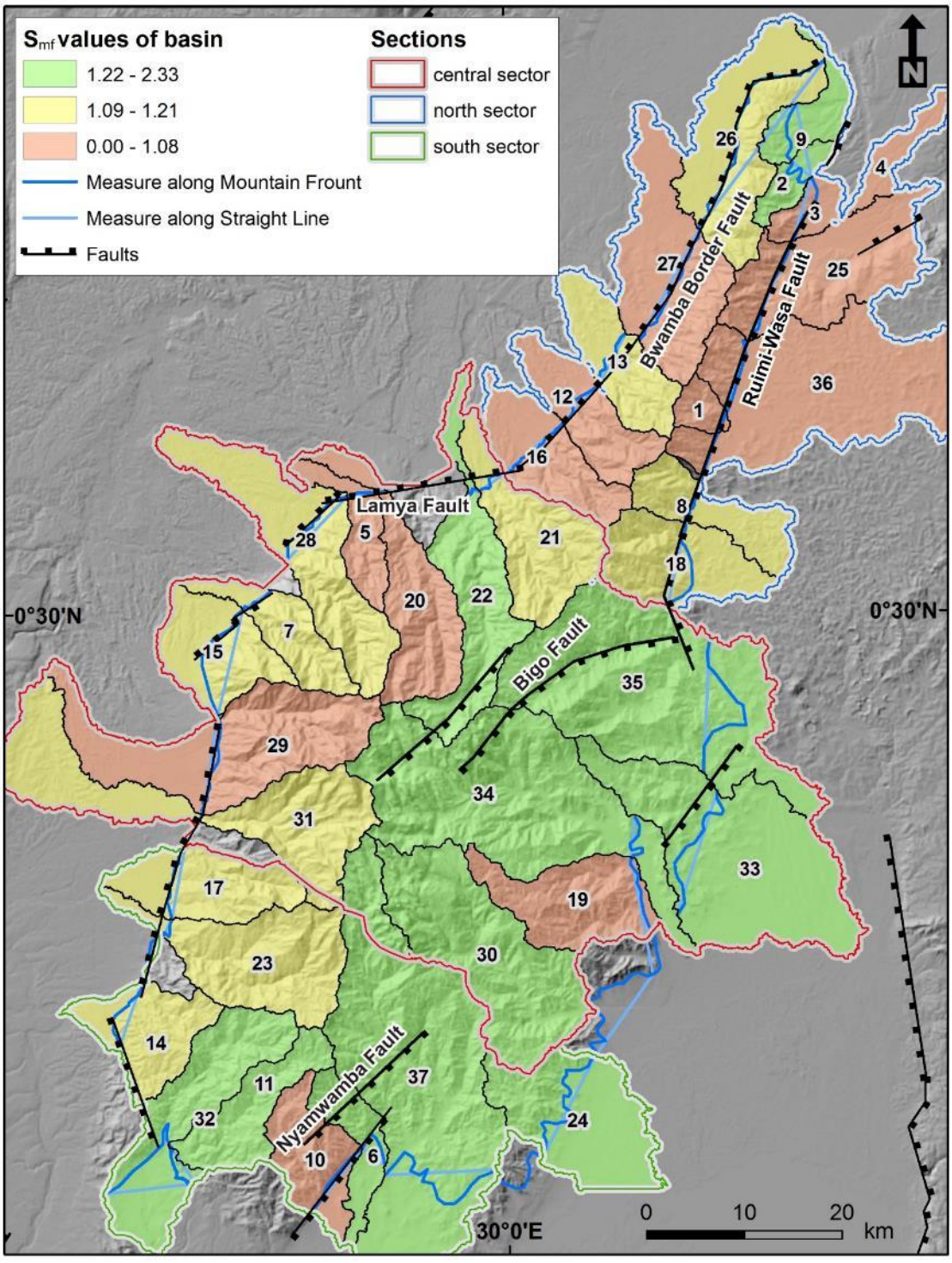

Figure 2-9 Mountain front sinuosity Smf map of the drainage basins in the Rwenzori Mountains. The Smf values of the drainage basins are classified into low (0.00-1.08), moderate (1.09-1.21), and high (1.22-2.33). Note that most of the drainage basins with low Smf values are intersected by major faults.

2.4.1.3. Hypsometric curve and hypsometric integral (HI index)

We divided the hypsometric curves of the drainage basins in the Rwenzori Mountains into concave, convex, S, and linear shape (Fig. 10A). Examples of these hypsometric curves are shown in Figs. 10C-E. We found that the HI values of these drainage basins range between 0.12 and 0.50 (Fig. 10B). We classified the HI values as low when they are < 0.25, as moderate when they are between 0.26 and 0.37, and as high when they are > 0.38 (Fig. 10B). We found that none of the drainage basins in the Rwenzori Mountains have HI value > 0.6. The HI values > 0.6 was suggested by Strahler (1952) to indicate unstable, immature relief that is in disequilibrium stage. We attribute the absence of HI values > 0.6 to the low rate of rock uplift in the Rwenzori Mountains.

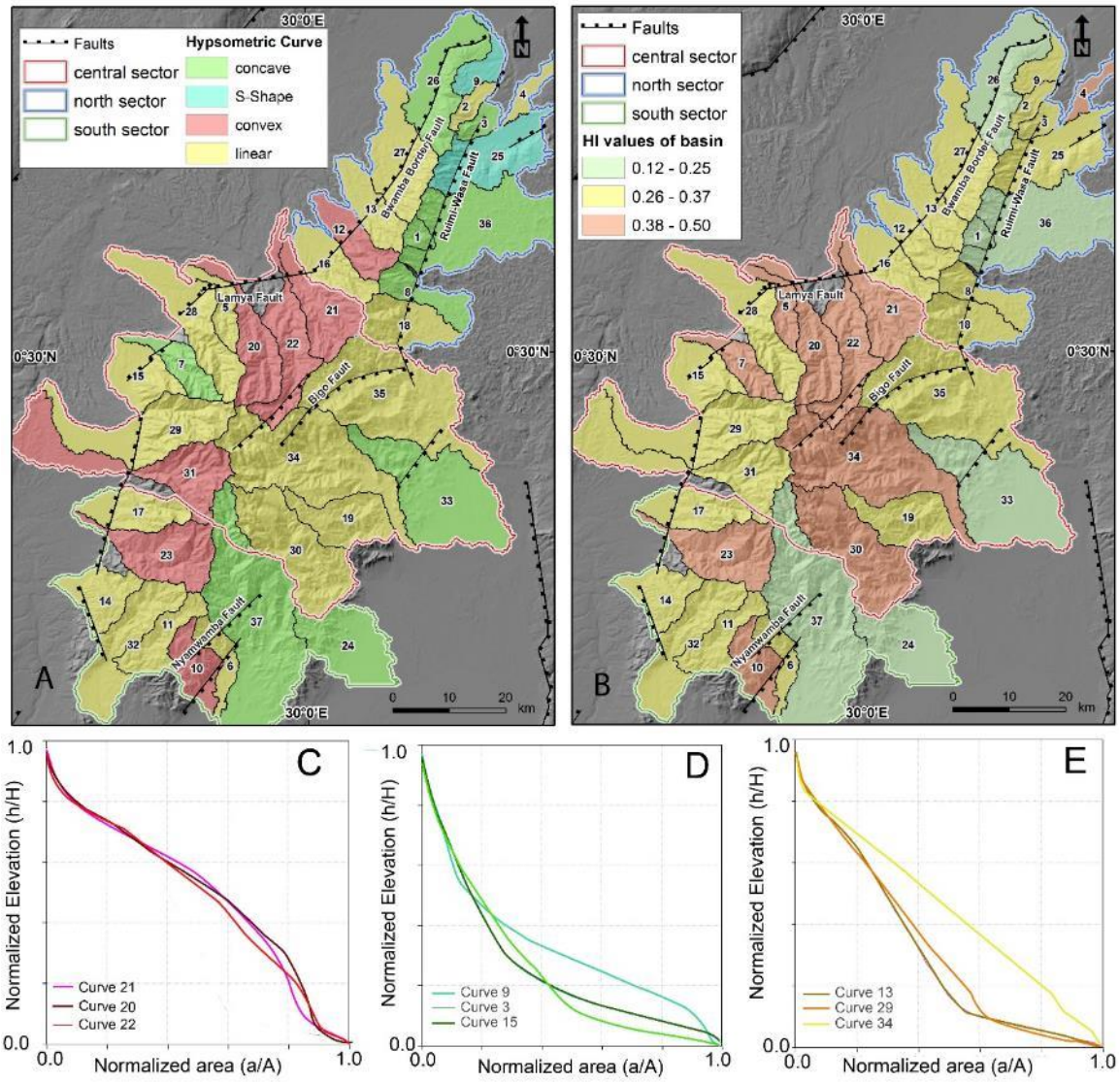

Figure 2-10 (A) Hypsometric index (HI) map of the drainage basins in the Rwenzori Mountains. The HI values are classified into low (<0.26) for stable at equilibrium basins, high (0.38-0.5) for at disequilibrium stage drainage basins, and moderate (0.26 < HI < 0.37) for drainage basins between the two end members. (B) Hypsometric curves map of the drainage basins in the Rwenzori Mountains. The S-shaped and concave hypsometric curves are represented in similar color (green) because they have similar tectonic implication. (C) Representative convex-shaped curves from drainage basins 21, 22, and 23 indicative of basins in youthful and disequilibrium stage. (D) Representative S-shape or concave-shaped curves from basins 3, 9, and 15 indicative of mature and at equilibrium stage basins. (E) Representative linear-shaped curves from drainage basins 13, 29, and 34 representing basins between the two end members.

Generally, we observed that the drainage basins with high HI values also have convex hypsometric curves; those with moderate HI values have linear curves; and those with low HI value have concave or S-shaped curves. However, some of the drainage basins in the central sector of the Rwenzori Mountains (basins 20, 21, and 22) have high HI values and convex

hypsometric curves indicating that these basins are in a young and tectonically active stage. Differently, some of the drainage basins in the north sector (basins 1, 26, and 36) have low HI values and concave hypsometric curves indicating a mature stage as suggested by Strahler's landscape evolution model (Strahler, 1952). Within the north sector, the drainage basins in the eastern slope (basins 1, 3, 8, and 36) show more concave hypsometric curves than those on the western slope (basins 2, 13, 16, and 27; Fig. 10A). Also, we observed a general increase in the HI values of the drainage basin from the north sector to the central sector of the Rwenzori Mountains (Fig. 10B). We also observed the presence of drainage basins with complex hypsometric curves. These show a convex shape only in their upper and lower parts and a concave shape in their middle part (e.g., curves 20 and 22 in Fig. 10C), suggesting a stream rejuvenation process.

2.4.1.4. Geophysical Relief

We found that the geophysical relief anomaly map shows an incision pattern that is generally following the modern drainage network of the Rwenzori Mountains (Fig. 11) with a maximum incision of 1280 m, occurring mostly in the central sector (basins 7, 28, 29, 31, and 34). The geophysical relief anomaly map also shows that the western side of the central sector (basins 7, 17, 28, 29, and 31 and the western part of basin 34) has experienced more erosion compared to its eastern side (basins 19 and 30 and the eastern part of basins 34 and 35). This is possibly caused by the eastward tilting of the Rwenzori Mountains resulting from a higher rate of rock uplift on the western side of the mountains, hence more erosion. These results are in good agreement with those of Bauer et al. (2012) who observed that the slopes on the eastern side of the Rwenzori Mountains are less steep compared to those in the west side. The geophysical relief anomaly map also suggests that the drainage in the north sector has less incision depth compared

to that in the central and south sectors (Fig. 11).

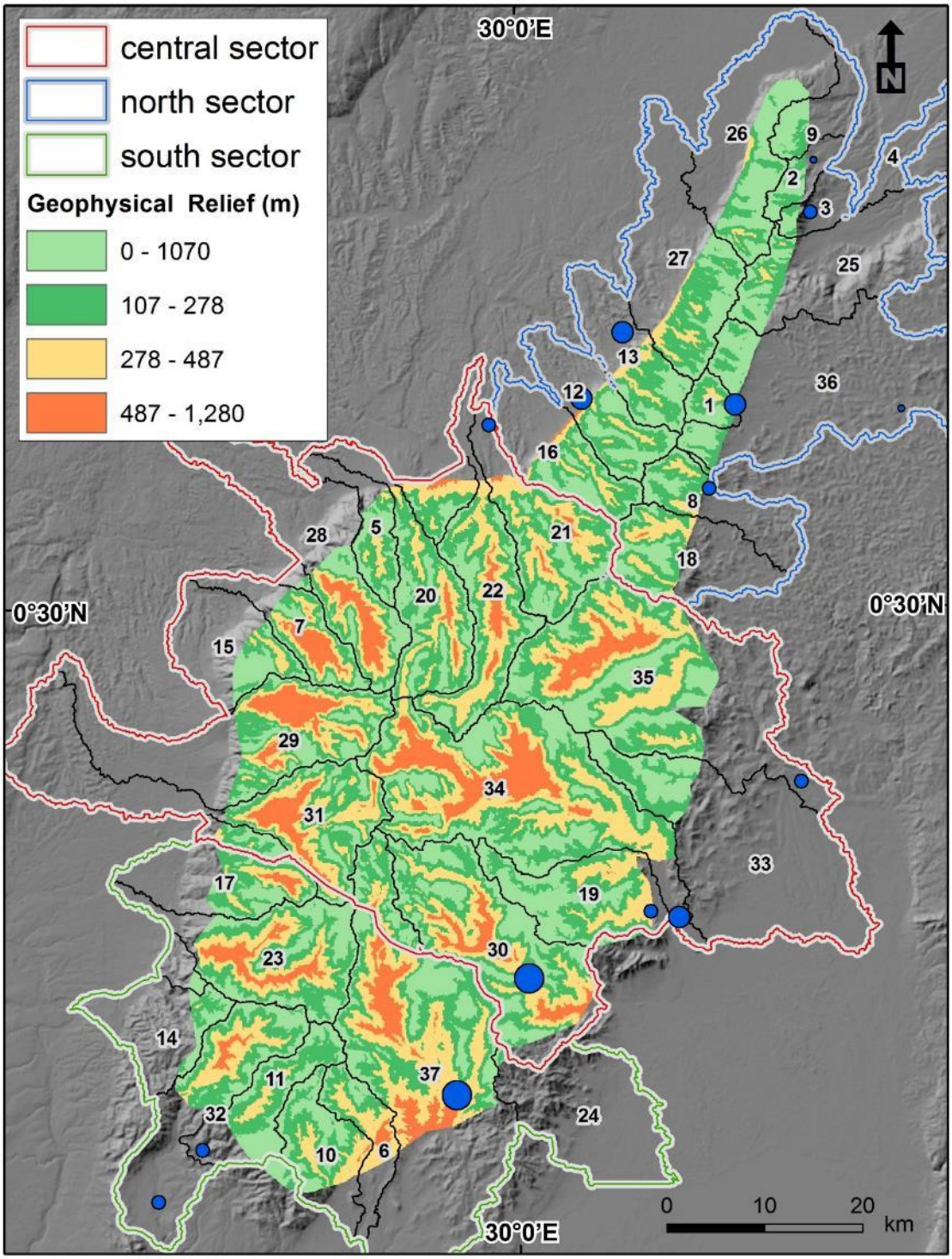

Figure 2-11 Geophysical relief map of the drainage basins of the Rwenzori Mountains. Values in meters represent the minimum incision depth. The Blue dots indicate the location and magnitude of the incision rate. Please refer to Fig. 13 for details.

2.4.1.5. Shape factor (Shp)

We found that the Shp values of the drainage basins in the Rwenzori Mountains vary between 0.38 and 0.85 (Fig. 12). We classified the drainage basins as circular when their Shp values are > 0.68, as moderately elongated when their Shp values are between 0.62 and 0.67, as elongated when their Shp values are between 0.52 and 0.61, and as highly elongated when their Shp values are < 0.51 (Fig. 12). We observed that the drainage basins in the western side of the central sector (basins 5, 7, 20, 22, 28, 29, and 31) have the highest Shp values compared to the rest of the drainage basins of the Rwenzori Mountains (Fig. 12). This indicates that these basins are more elongated than the rest of the basins in the Rwenzori Mountains. Differently, the drainage basins in the eastern side of the central sector as well as those in the north and south sectors have low Shp values, indicative of more rounded basins (Fig. 12). Also, in general, we observed that the drainage basins in the western side of the north sector (basins 12, 13, 16, and 27) have relatively higher Shp values compared to the basins in the eastern side of this sector (basins 1, 3, 18, 25, and 36).

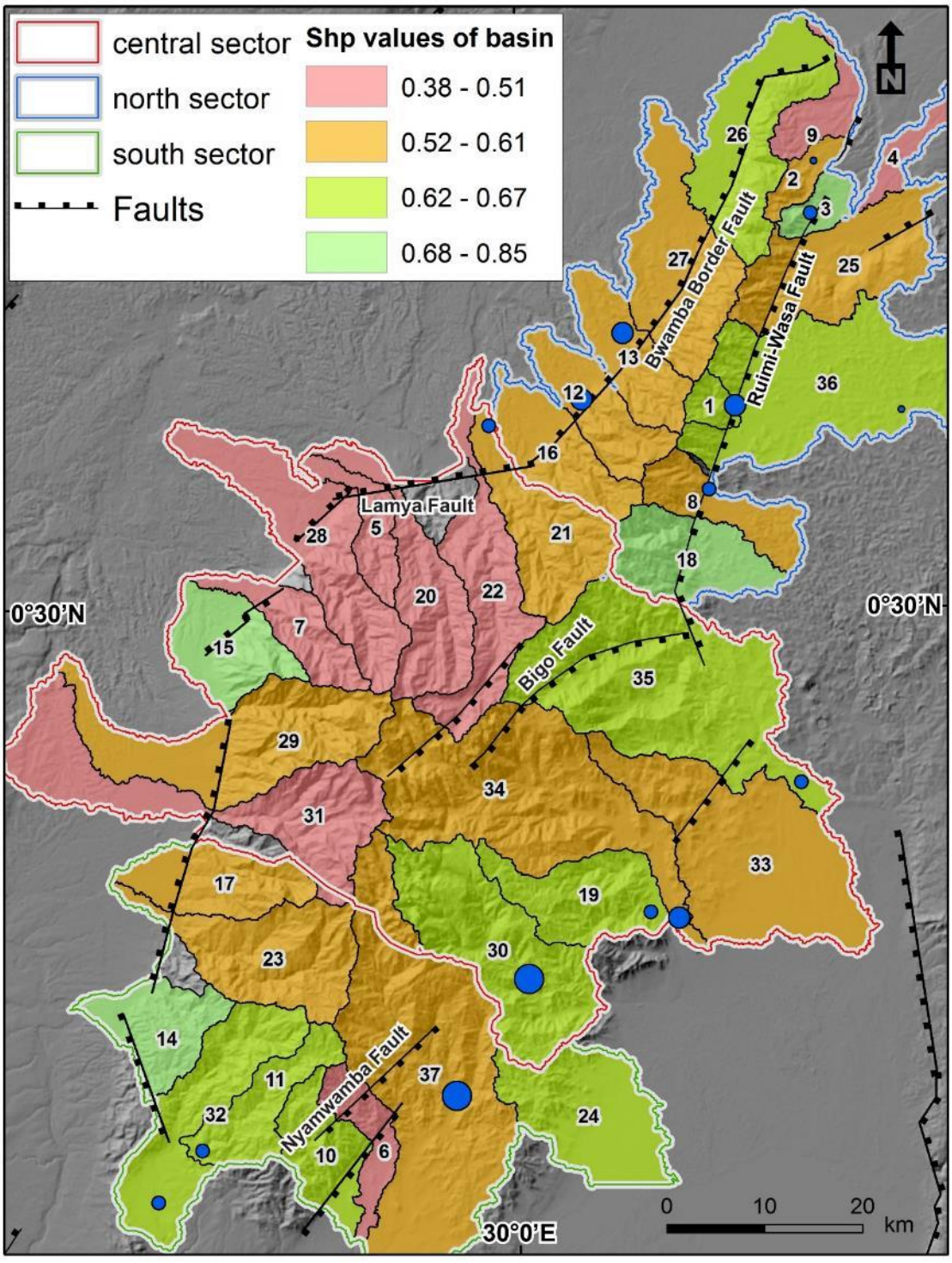

Figure 2-12 Shape factor (Shp) map of the drainage basins in the Rwenzori Mountains. Based on the Shp values, the drainage basins are classified as circular (Shp > 0.62), slightly elongated (0.52 < Shp < 0.61), and highly elongated (Shp < 0.51).

2.4.2. Linear geomorphic proxies

2.4.2.1. Normalized steepness index (k_{sn})

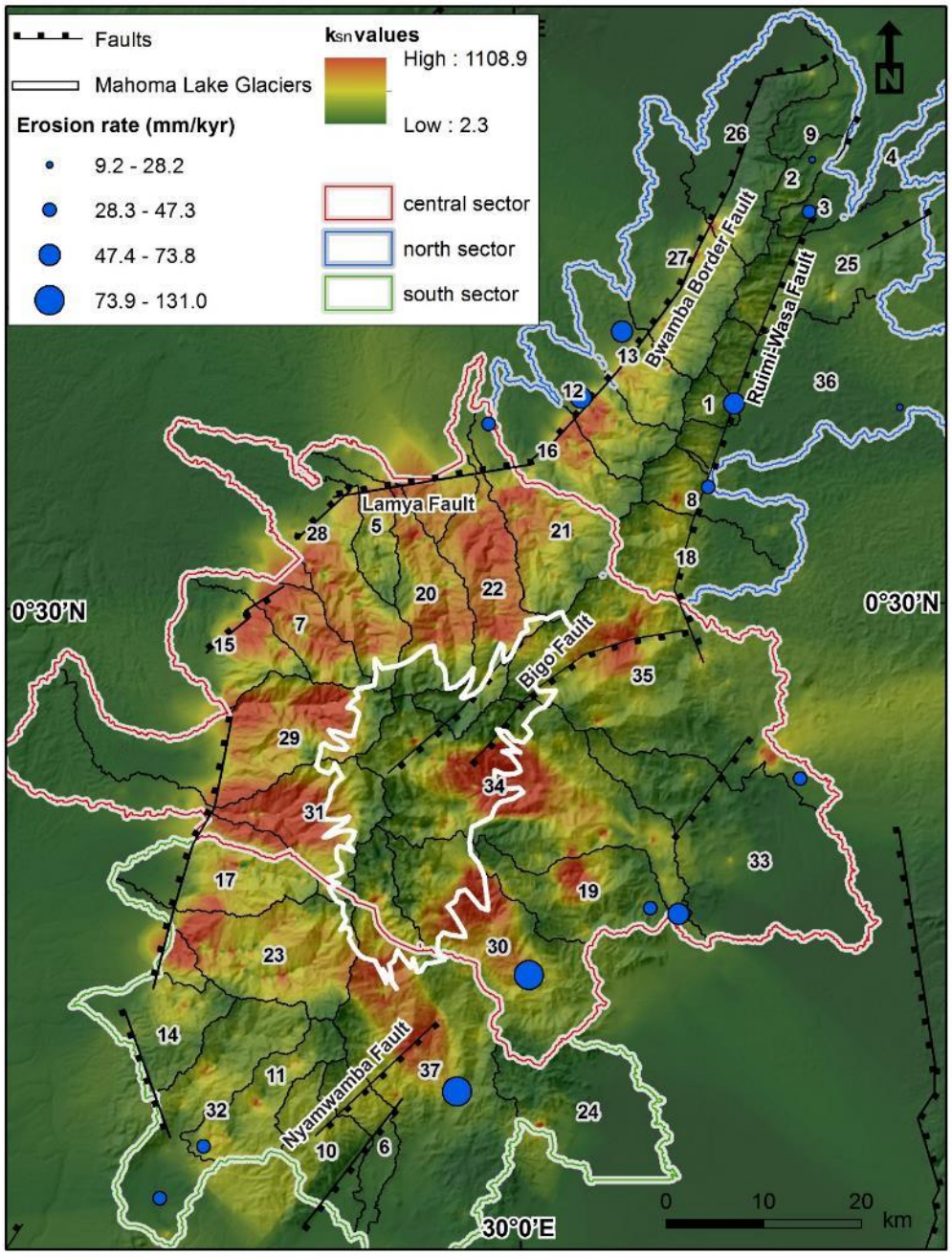

Figure 2-13 Normalized steepness index (ksn) map of the drainage basins in the Rwenzori Mountains constructed through the interpolation of the ksn values of the main streams in the mountains. The blue circles show the locations and magnitudes of the erosion rates determined by Roller et al. (2012) from cosmogenic 10Be analysis. The solid white line defines the extent of the Mahoma Lake glaciers.

We found that the k_{sn} values of the main streams within the drainage basins in the Rwenzori Mountains range between 2.3 and 1109 (Fig. 13). Mostly, the highest k_{sn} values are recorded for the drainage basins on the western side of the central sector. On the other hand, the lowest k_{sn} values are calculated for the drainage basins of the north and south sectors. We also observed that the k_{sn} values of the streams within the drainage basins on the western side of the north sector are relatively higher compared to the eastern side. Also, the central part of the central sector is characterized by anomalously low k_{sn} values (~100). The limits of these anomalously low k_{sn} values coincide with the extent of the Mahoma Lake glaciers (Fig. 13).

2.4.2.2. Length-gradient index (SLk)

We found that the SLk values of the main streams within the drainage basins in the Rwenzori Mountains range between 34 and 39,000 (Fig. 14). The highest SLk values are found in the drainage basins of the central sector, especially basins 20 and 22 close to the intersection of the Lamya fault with the Bwamba fault (Fig. 14). The SLk values reach their lowest level in the drainage basins of the north and south sectors. The distribution pattern of the SLk values calculated for the main streams within the drainage basins of the Rwenzori Mountains seems to follow the distribution pattern of R^2 (compare Figs. 7 and 14). As exemplified by basin 22, drainage basins with low levels of stream maturity (as indicated by low R^2 values) also have anomalously low SLk values. Also, drainage basins within the extent of the Mahoma Lake glaciers exhibits lower SLk values than those of other regions in the central sector of the

Rwenzori Mountains.

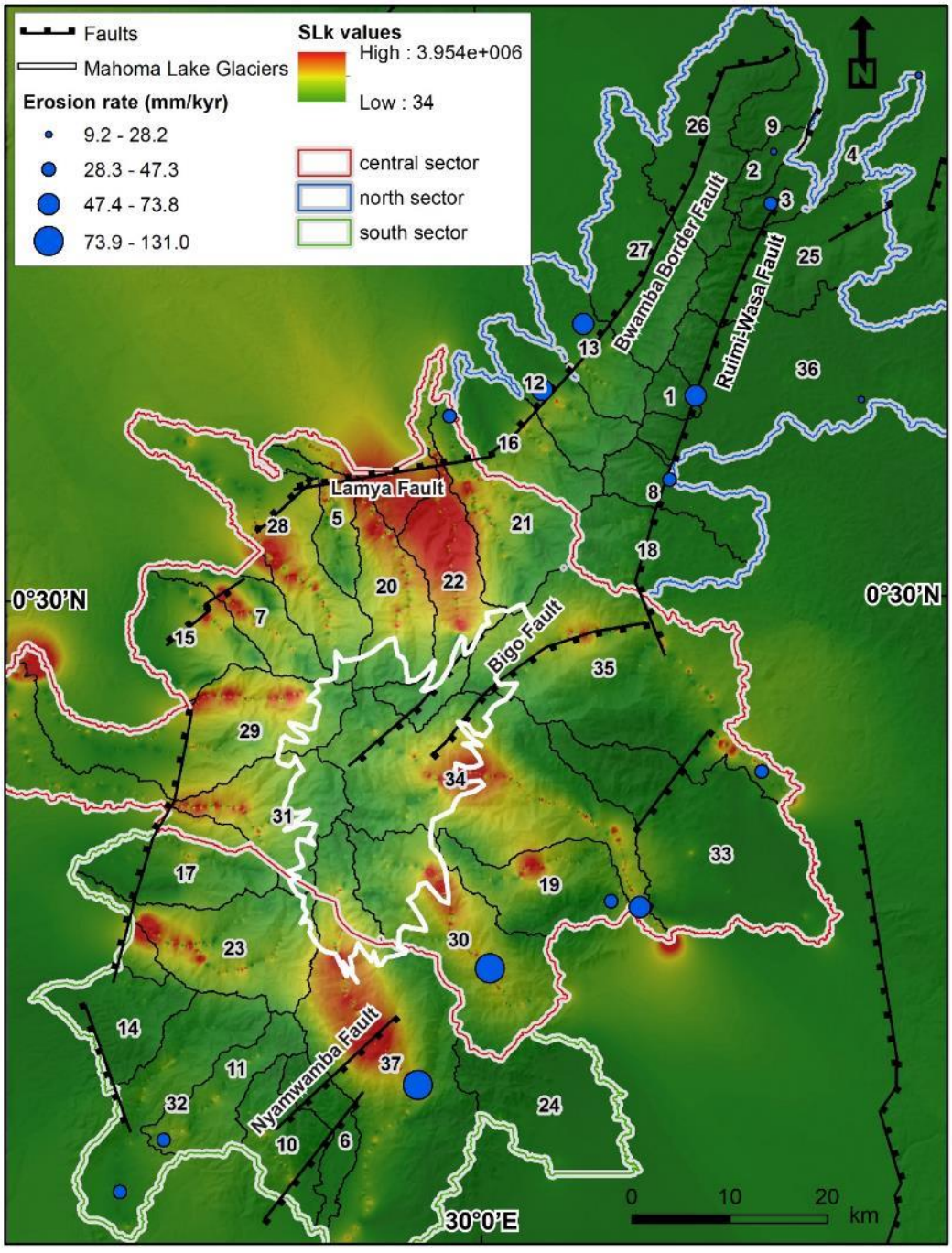

Figure 2-14 Stream length-gradient (SLk) anomaly map of the drainage basins in the Rwenzori Mountains, constructed by interpolation of SLk values that are calculated using an interval of 150 m along the main streams of the mountains. The blue circles represent the locations and magnitudes of the erosion rates determined by Roller et al. (2012) from cosmogenic 10Be analysis. The solid white line defines the extent of the Mahoma Lake glaciers.

2.4.2.3. Chi analysis (Mχ)

We found that the Mχ values of the streams within the drainage basins in the Rwenzori Mountains range between 0 and 19 (Fig. 15). In general, the streams with the highest Mχ values are located in the drainage basins on the western side of the central sector (basins 7, 15, 20, 22, 28, 29, 30, and 31). Differently, the streams within the drainage basins on the central part of the central sector have notable low Mχ values. This region coincides with the extent of Mahoma Lake glacier. Also, we found that the streams in the eastern slope on the north sector have relatively higher Mχ values compared to those in the western slope. This suggests differential erosion because of the eastward tilting of the Rwenzori Mountains. We also observed that the normal faults in the Rwenzori Mountains are depicted as divide lines between streams with low Mχ values in the hanging wall and streams with high Mχ values on the footwall of the faults (Fig. 15). We also noticed a distinct boundary separating low Mχ values for streams within the extent of Mahoma Lake glacier from relatively higher Mχ values for streams outside the glacier extent

(Fig. 15).

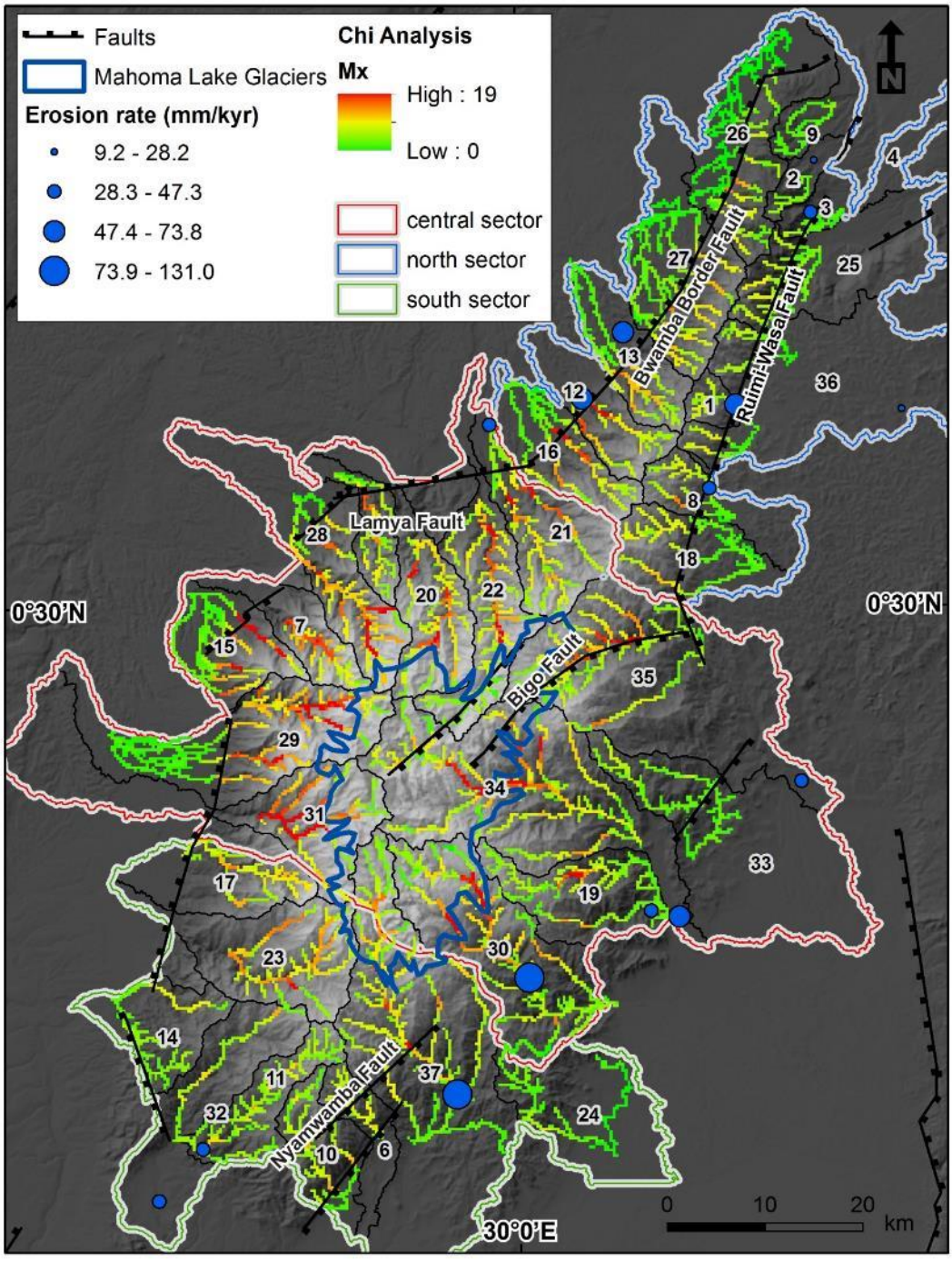

Figure 2-15 Chi ($M\chi$) map of the main streams of the drainage basins in Rwenzori Mountains computed using 100-m interval. The blue circles represent the locations and magnitudes of the erosion rates determined by Roller et al. (2012) from cosmogenic 10Be analysis. The solid blue line defines the extent of the Mahoma Lake glaciers.

2.5. Discussion

2.5.1. Areal geomorphic proxies, rock uplift, erosion rates, and drainage basin's maturity

With the exception of Shp, at the regional Rwenzori Mountains scale, we found no direct correlation between the drainage basin's maturity R^2 on the one hand and the areal geomorphic proxies on the other hand. This is reflected in the low values of the correlation coefficient r when R^2 is plotted against AF (r = 0.14); S_{mf} (r = -0.15); HI (r = 0.10); geophysical relief (r = -0.04); and Shp (r = -0.28) (Fig. 16A). However, at the local drainage basin scale, we found that some of the areal geomorphic proxies are reflective of local tectonic activities, especially fault activities. We will then discussion the proxies as follows.

2.5.1.1. Asymmetry factor (AF)

The AF values are usually used as a proxy for differential rock uplift in a given drainage basin. High AF values indicate tilting and high level of rock uplift, whereas low AF values indicate tectonic quiescence of the drainage basin (Schumm et al., 2002). We found that the drainage basins with moderate to high AF values (>12) are located in the north and south sectors of the Rwenzori Mountains as well as the western side of the central sector (Fig. 8). This can be interpreted as because of eastward tilting and asymmetrical tectonic activities in the Rwenzori Mountains. However, this interpretation is not in agreement with the high level of maturity of the streams within these basins as indicated by their high R^2 values (Fig. 7). This interpretation is also not in agreement with the low erosion rates reported from the streams within some of these drainage basins (Roller et al., 2012). Additionally, the lowest AF values are reported for the drainage basins occupying the middle and eastern parts of the central sector (Fig. 8). These drainage basins are expected to have high AF values because they occupy the part of the Rwenzori Mountains that is witnessing high tectonic activities. Below, we provide a possible

explanation for such discrepancy between the AF as a geomorphic proxy and the observed tectonic activities.

The AF is sensitive to the size of the drainage basin as well as the stream order of the channels constituting the drainage network of the basin (Ries, 2013). Hence, it is likely that the variation in the AF values of the drainage basins in the Rwenzori Mountains is a reflection of variation in the size of the drainage basins and their stream orders rather than the level of tectonic activities. We noticed that all the drainage basins with low AF values (<12) are those that have large area and higher third and fourth stream order (Fig. 8). On the other hand, the drainage basins with high AF values (>20) are the ones with small area and lower first and second stream order (Fig. 8). For example, the drainage basins in the central sector of the Rwenzori Mountains are dominated by first and second order streams, and these basins have low AF values. This leads us to conclude that the AF can be an effective geomorphic proxy for describing the rock uplift only if the drainage basins used in the computation have similar size and similar stream order. The AF values are also reported to indicate the general tilting direction of the drainage basins (Ries, 2013). However, we found it not possible to accurately define the tilting direction of the drainage basins in the Rwenzori Mountains from the AF values alone. This is because the distribution of the AF values does not match the known tilting geometry of the asymmetrical horst constituting the Rwenzori Mountains.

2.5.1.2. Mountain front sinuosity (Smf) and fault activity

We found that the distribution pattern of the S_{mf} values of the drainage basins in the Rwenzori Mountains is successful in highlighting the location of normal faults rather than the stage of drainage basin's maturity or equilibrium (compare Figs. 7 and 9). For example, basins 12, 13, 16, 21, 26, and 27 on the western side of the north sector are intersected by the Bwamaba fault. Similarly, basins 1, 3, 8, 18, 25, and 36 on the eastern side of the north sector are intersected

by the Ruimi-Wasa fault. All of these drainage basins have moderate to low S_{mf} values (Fig. 9). Additionally, in the south sector, basin 10 has an anomalously low S_{mf} value, and this basin is intersected by the Nymwamba fault (Fig. 9). Hence, we conclude that the S_{mf} geomorphic proxy is effective in detecting local fault activities.

We found that the level of maturity of the drainage basin is poorly reflected by the S_{mf} geomorphic proxy for the following reasons: (i) it is difficult to distinguish the remnants of alluvial fans formed during different tectonic events. These alluvial fans could have been deposited during an earlier rock uplift pulse. Thus, if these older alluvial fans are included in the measurement of the mountain front, the S_{mf} value will be unrealistically high (Bull, 2008); (ii) the shape and size of the drainage basin also needs to be taken into consideration when comparing the S_{mf} values of different drainage basins. The drainage basins in tectonically active regions do not always form fan shapes but sometimes form an irregular and a rather small mountain front. In this case, the length of the mountain front was not long enough compared to the size of the drainage basin. For example, the mountain front of drainage basin 34 is only 4.5 km long. This resulted in calculating a low S_{mf} value for this drainage basin regardless that it is intercepted by the Bigo fault (Fig. 9).

2.5.1.3. Hypsometric curve and hypsometric integral (HI)

We found that the HI values are consistent with the shapes of the hypsometric curves for most of the drainage basins in the Rwenzori Mountains (Figs. 10A and B). Theoretically, the concave and S-shaped hypsometric curves are considered to be associated with low HI values (<0.25), and these low values are indicative of drainage basins in their equilibrium stage. On the other hand, the convex hypsometric curves are thought to be associated with high HI values (>0.38), and these high values represent drainage basins that are developing during tectonic activities (Strahler, 1952; Willgoose and Hancock, 1998; Perez-Pena et al., 2009a). The results

we obtained for the majority (32 out of 37) of the drainage basins in the Rwenzori Mountains are in good agreement with the theoretical relationship between the HI values and the drainage basin's development stage. The drainage basins in the north and south sectors of the mountains have significantly low HI values and have concave hypsometric curves, while the basins in the central sector have moderate to high HI values and convex hypsometric curves (Figs. 10A and B).

Regardless of the success we report here, there are some drawbacks in using the HI values and hypsometric curves as geomorphic proxies for drainage basins' maturity. Willgoose and Hancock (1998) reported that the hypsometric curves and (HI) values can also be influenced by the shape of the drainage basin, hence hindering using them for the comparison between wide and narrow basins. For example, there is a close similarity between basins 12 and 13 in the north sector of the Rwenzori Mountains (Fig. 10A). They are adjacent to each other, drain within similar elevation and lithology, and have similar geographic extent (96 km^2 for basin 12 and 99 km^2 for basin 13). They also have similar erosion rates (64 mm/ky for basin 12 and 61.8 mm/ky for basin 13) as calculated from cosmogenic ^{10}Be analysis (Roller et al., 2012). However, the upstream hypsometric curves of these two drainage basins are significantly different in which basin 12 has a convex shape (Fig. 10C) and basin 13 has a linear shape (Fig 10E). This might be because of the relatively wider upstream area of basin 13, allowing for the draining of additional second order streams (Fig. 5). Hence, the shape of the drainage basin and the number of streams draining within it need to be considered when using the hypsometric curve and the (HI) values as geomorphic proxies.

Also, in addition to the three end member shapes of the hypsometric curves (concave and S-shaped, convex, and linear), we also noticed the presence of more complicated hypsometric curves for some of the drainage basins in the Rwenzori Mountains. For example, the hypsometric curve of basin 21 has a concave shape of its upstream and downstream segments and a convex shape for its middle part (Fig. 10C). It is not easy to infer the state of the drainage basin's maturity from such hypsometric curves. Nonetheless, we observed that the convex part of the

hypsometric curve of this drainage basin coincides with where the basin is intersected by the Bwambar fault (Fig. 10B). This suggests that the fault activities might have caused the convex shape of the hypsometric curve. Hence, we conclude that the interpretation of complex-shaped hypsometric curves requires detailed analysis of the drainage basin for the presence of sharp contacts between different lithological units and local faults. Also, it is possible to interpret such complex-shaped hypsometric curves using additional parameters for the drainage basin such as skewness and kurtosis, which can help distinguish between the erosion rates at the headward and lower reaches of the drainage basins (Luo, 2000).

Moreover, the HI value alone might not be the single discrete value capable of fully capturing the shape of the hypsometric curve. Generally, most drainage basins in the Rwenzori Mountains have concave hypsometric curves and low HI values or convex hypsometric curves and high HI values. However, we found some exceptions. For example, basins 9 and 29 have the same HI values of 0.32. However, the shape of their hypsometric curves is different. Basin 9 has an idealized S-shaped hypsometric curve (Fig. 10D), whereas basin 29 has a linear curve (Fig. 10E). This discrepancy might have been caused by the large difference in the size of the two drainage basins (83 km^2 for basin 9 and 239 km^2 for basin 29). This discrepancy is also recognized in previous studies (Keller et al., 1997; Hurtrez et al., 1999). These studies suggest that small drainage basins tend to have unexpectedly high HI values because of the dominance of hillslope processes that decrease as the size of the drainage basin increases. Thus, it can be misleading to consider that the high HI value calculated for every drainage basin is an indication of high rock uplift without considering the shape of the hypsometric curve and the size of the basin.

2.5.1.4. Geophysical relief

Results of our geophysical relief analysis showing the spatial variation of the minimum amount of incision of the streams within the drainage basins in the Rwenzori Mountains are in

good agreement with the erosion rates obtained from cosmogenic ^{10}Be analysis (Roller et al., 2012; Fig. 11). We observed that the most deeply incised streams (high geophysical relief values) are found in basins 7, 22, 23, 28, 29, 30, 31, 34, 35, and 37 (Fig. 11). The streams within these drainage basins are expected to have low levels of maturity because high geophysical relief values (deep incision) are an indication of active rock uplift. However, some of these drainage basins (such as basins 28, 29, and 34) have high levels of the drainage basin's maturity as indicated by their high R^2 values (Fig. 7). This reflects the uncertainties of the geophysical relief as a geomorphic proxy for evaluating the streams and drainage basins maturity.

2.5.1.5. Shape factor (Shp)

We found that the Shp values distribution pattern is relatively in good agreement with the drainage basin's maturity, especially in the central sector of the Rwenzori Mountains (compare Figs. 7 and 12). Most round-shaped drainage basins with high Shp values are also found to be in an equilibrium stage and have low erosion rates obtained from cosmogenic ^{10}Be analysis (Roller et al., 2012; Fig. 12), The only exception is basin 15, which is located in the central sector of the Rwenzori Mountains at the intersection of two segments of the Bwamba fault (Fig. 12). Because this drainage basin is tectonically active, it is expected to have a low Shp value. Nonetheless, the Shp value of this drainage basin is as high as 0.74 (Fig. 12).

2.5.2. Linear geomorphic proxies, rock uplift, erosion rates, drainage basin's maturity, and glacier extent

We found that the k_{sn}, SLk, and Mχ values for streams within the drainage basins of the Rwenzori Mountains have strong positive correlation with erosion rates measured by cosmogenic ^{10}Be analysis (Roller et al., 2012) from streams within basins 1, 3, 8, 11, 12, 13, 19, 21, 30, 32, 34, 35, and 37 (Figs. 13, 14, and 15). The r between erosion rates and k_{sn} is 0.73, between erosion

rate and SLk is 0.75, and between erosion rate and Mχ is 0.94. These geomorphic proxies predict similar tectonic implications, as they are derived from the analysis of perturbation to equilibrium state of stream channels (Keller et al., 1997; Perron and Royden, 2013; Willett et al., 2014). The linear proxies are proven to be useful in mapping the location of faults and predict their displacements in convergent tectonic settings such as Taiwan (Chen et al., 2003) and the Tibet Plateau (Kirby et al., 2003). Here, we also show that these proxies are influenced by the presence of active faults of the Rwenzori Mountains. Almost all the drainage basins of the Rwenzori Mountains that are intersected by active faults have positive k_{sn} (Fig. 13), SLk (Fig. 14), and Mχ (Fig. 15) anomalies. For example, drainage basin 37 is intersected by the Nyamwamba fault, basins 20 and 22 are intersected by the Lamya fault, and basins 34 and 35 are intersected by the Bigo fault. These basins have high k_{sn} (Fig. 13), SLk (Fig. 14), and Mχ values. However, although basins 1, 3, 9, 13, 25, 26, 27, and 36 in the north sector of the Rwenzori Mountains are intersected by Bwamba fault and Ruimi-Wasa fault, these basins do not have, as expected, high k_{sn}, SLk, and Mχ values. This may be explained by that these two faults are inactive or have rather a small displacement in the north sector compared to the central sector of the Rwenzori Mountains. This may also explain the low erosion rates (obtained by cosmogenic ^{10}Be analysis; Roller et al., 2012) of the drainage basins in the north sector (Figs. 13, 14, and 15). The erosion rates of the drainage basins intersected by these two faults decrease northward from basin 12 (67 mm/ky) to basin 2 (28 mm/ky) in the north sector. Similarly, the k_{sn}, SLk, and Mχ values also decrease northward. Hence, the linear geomorphic proxies can also provide information about the displacement of rift-related faults.

The k_{sn}, SLk, and Mχ have high potential to be used as quantitative geomorphic proxies for estimating rock uplift rates in steady-state conditions. Previous studies found k_{sn} and SLk to be proportional to local steady-state rock uplift rates when erosion rates are linearly related to uplift rates, and when rock uplift rates are high (Kirby et al., 2003; Perez-Pena et al., 2009b). In the drainage basins of the Rwenzori Mountains, the k_{sn}, SLk, and Mχ values show moderate to

high positive correlations (r > 0.7) with the erosion rates measured by cosmogenic ^{10}Be analysis by Roller et al. (2012; Fig. 16B). The positive correlation between some linear geomorphic proxies and erosion rates is also documented by Roller et al. (2012) who reported an r value of 0.63 between k_{sn} and erosion rates in the Rwenzori Mountains.

It has been suggested that using k_{sn} and SLk as geomorphic proxies for quantifying rock uplift is more successful in regions with high erosion and uplift rates (usually >300 mm/ky), especially during mountain-building activities (Nexer et al., 2015). Nonetheless, Pedrera et al. (2009) examined the relationship between the SLk and tectonic activities in the Betic Cordillera of Spain and found that it is also discernable to positively correlate the SLk values to rock uplift rates in this low uplift rates region (as low as 50 mm/ky) because the bedrock lithology is highly resistant. Our result also highlights the usability of linear geomorphic proxies for estimating rock uplift rates in continental rifting activities that cause moderate to low erosion rates.

The distribution pattern of the linear geomorphic proxies in the Rwenzori Mountains also shows strong correlation with the extent of glaciers. It is expected that high relief areas would experience more erosion by post-glacial fluvial erosion than low relief areas (Montgomery and Brandon, 2002). Hence, it is expected that streams within drainage basins in the central part of the central sector of the Rwenzori Mountains will have relatively high k_{sn}, SLk, and Mχ values. This is because linear geomorphic proxies have strong positive correlation with erosion rates. Nonetheless, the low k_{sn}, SLk, and Mχ reported for the streams in the drainage basins in the central part of the central sector of the Rwenzori Mountains (Figs. 13, 14, and 15) indicate low erosion rates. We suggest that this is caused by the retreatment of the Mahoma Lake glacier. Roller et al. (2012) also suggested that the correlation between k_{sn} and erosion rates can be biased by glacial imprinting. Therefore, care should be taken when interpreting linear geomorphic proxies in tectonically active regions that are partially covered by glaciers.

2.5.3. Relationships between geomorphic proxies and implication for morphotectonic evolution of the Rwenzori Mountains

We found no direct linear correlation between the numerical values of the areal geomorphic proxies (AF, S_{mf}, Hi, geophysical relief, and Shp) computed for the drainage basins in the Rwenzori Mountains (Fig. 16A). We found r between the numerical values of these proxies to be as low as 0.01 (between S_{mf} and geophysical relief), and it is not higher than 0.4 (between AF and geophysical relief). Differently, we found higher linear correlation between the numerical values of the linear geomorphic proxies (k_{sn}, SLk, and Mχ) calculated for the streams within the drainage basins in the Rwenzori Mountains (Fig. 16B). This is particularly true for k_{sn} and SLk where r between them is as high as 0.83 (Fig. 16B). The strong correlation between these two linear geomorphic proxies is expected because both of them describe the steepness of streams. Differently, we found the correlation between SLk and Mχ on the one hand and k_{sn} and Mχ on the other hand is relatively low where is 0.45 between k_{sn} and Mχ, and it is 0.42 between SLk and Mχ (Fig. 16B).

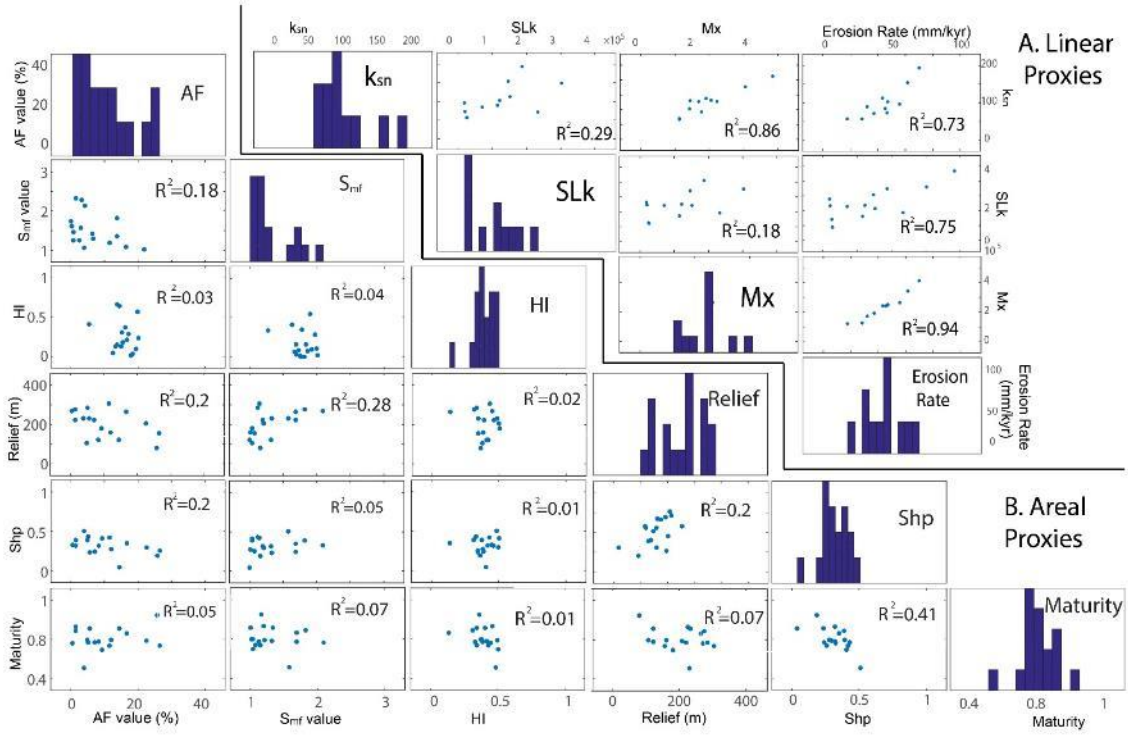

Figure 2-16 Matrix scatter plot correlating: (A) the linear geomorphic proxies (normalized steepness index (ksn), stream length-gradient (SLk), Chi (Mχ)) of the streams of the drainage basins in the Rwenzori Mountains with each other and with the erosion rate determined by Roller et al. (2012) from cosmogenic 10Be analysis; and (B) the areal geomorphic proxies (asymmetric factor (AF), mountain front sinuosity (Smf), hypsometric index (HI), geophysical relief, shape factor (Shp)) with each other and with basins maturity index expressed by the 'Good of Fitness' (R2).

Regardless of the lack of linear correlation between the numerical values of the areal geomorphic proxies, a general pattern emerges when qualitatively evaluated together. This general pattern suggests that the western side of the Rwenzori Mountains is more tectonically active than the eastern side, especially the western side of the central sector. Generally, the highest AF, S_{mf}, HI, and geophysical relief values indicative of less drainage basin's maturity, hence higher rock uplift, are computed for the basins in the western side of the Rwenzori Mountains (Figs. 8, 9, 10B, and 11). Also, the lowest Shp values are found in the drainage basins in the western side of the Rwenzori Mountains (Fig. 12). The asymmetrical nature of tectonic activities in the Rwenzori Mountains (more active western side) is even more obvious from the

linear geomorphic proxies computed for the streams within the drainage basins of the mountains. Higher k_{sn}, SLk and Mχ values indicative of relatively higher rates of erosion and tectonic uplift are observed in the western side of the Rwenzori Mountains (Figs. 13, 14, and 15). The asymmetry of the tectonic activities we report here from the geomorphic proxies is in good agreement with results from low-temperature thermochronological studies showing that the western flank of the mountains might have witnessed a higher level of rock uplift compared to their eastern flank (Bauer et al., 2013).

We note that the presence of the Mahoma Lake glacier in the center of the central sector of the Rwenzori Mountains has its localized influence on the anomalies of the geomorphic proxies and their distribution pattern. However, we do not think that the variation in lithology in the Rwenzori Mountains or precipitation rates have any influence on the anomalies of the geomorphic proxies and their distribution pattern. This is because the most prominent anomalies we observed in the geomorphic proxies are found stretching in a N-S direction in the western side of the Rwenzori Mountains. We would expect a more distributed or E-W geomorphic proxy anomaly pattern if the E-W trending Precambrian lithological units in the Rwenzori Mountains have any control on these anomalies.

Theoretically, it is possible that the orographic lifting effect of the NNE-trending Rwenzori Mountains on the east-moving moist air from the Atlantic Ocean could lead to enhanced precipitation on the western side of the mountains leaving the eastern side in the rain shadow. This could lead to higher erosion rates in the drainage basins in the western side of the Rwenzori Mountains. However, in situ measurements (Taylor et al., 2009) and remote sensing measurements from TRMM (Fig. 4) found that the orographic lifting affect all sides of the Rwenzori Mountains by enhancing precipitation as a function of increased elevation of the mountains rather than their position relative to the flow direction of moist air.

2.6. Conclusions

Results of our ASTER DEM-based morpho-tectonic analysis of the Rwenzori Mountains in the western branch of the EARS using areal (AF, S_{mf}, HI, geophysical relief, and Shp) and linear geomorphic proxies (k_{sn}, SLk, and Mχ) showed the following: (i) the areal geomorphic proxies (AF, S_{mf}, HI, relief and Shp) can be implemented to evaluate the maturity of the drainage basins in the Rwenzori Mountains when factors such as the drainage basin size and geometry, stream order, glacier extent, and local structures are considered. (ii) The linear geomorphic proxies (k_{sn}, SLk, and Mχ) calculated from streams within the drainage basins in the Rwenzori Mountains can be positively correlated with erosion rates measured from cosmogenic ^{10}Be analysis. These linear geomorphic proxies can also be effectively used for identifying fault activities. (iii) Only the numerical values of the linear geomorphic proxies k_{sn} and Mχ show strong correlation with each other. (iv) The central sector of the Rwenzori Mountains, especially its western side, is tectonically active; while the north and south sectors of the mountains are in relative tectonic quiescence.

2.7. References

Ahnert, F., 1970. Functional relationships between denudation, relief, and uplift in large, mid-latitude drainage basins. American Journal of Science 268(3), 243-263.

Baber, M.B., 2013. Surface-exposure (^{10}Be) dating of the Omurubaho moraines in the Rwenzori Mountains of Uganda. M.S. Thesis, Dartmouth College, pp. 94.

Barcos, L., Jabaloy, A., Azdimousa, A., Asebriy, L., Gomez-Ortiz, D., Rodriguez-Peces, M.J., Tejero, R., Perez-Pena, J.V., 2014. Study of relief changes related to active doming in the eastern Moroccan Rif (Morocco) using geomorphological indices. Journal of African Earth Sciences 100, 493-509.

Bauer, F.U., Glasmacher, U., Ring, U., Schumann, A., Nagudi, B., 2010. Thermal and exhumation history of the central Rwenzori Mountains, Western Rift of the East African Rift System, Uganda. International Journal of Earth Sciences 99(7), 1575-1597.

Bauer, F.U., Glasmacher, U.A., Ring, U., Karl, M., Schumann, A., Nagudi, B., 2013. Tracing the exhumation history of the Rwenzori Mountains, Albertine Rift, Uganda, using low-temperature thermochronology. Tectonophysics 599, 8-28.

Bauer, F.U., Glasmacher, U., Ring, U., Grobe, R., Mambo, V., Starz, M., 2015. Long-term cooling history of the Albertine Rift: new evidence from the western rift shoulder, DR Congo. International Journal of Earth Sciences, 1-22.

Bauer, F.U., Karl, M., Glasmacher, U., Nagudi, B., Schumann, A., Mroszewski, L., 2012. The Rwenzori Mountains of western Uganda–Aspects on the evolution of their remarkable morphology within the Albertine Rift. Journal of African Earth Sciences 73, 44-56.

Binnie, S.A., Phillips, W.M., Summerfield, M.A., Fifield, L.K., 2007. Tectonic uplift, threshold hillslopes, and denudation rates in a developing mountain range. Geology 35(8), 743-746.

Bull, W.B., 1976. Tectonic geomorphology of the Mojave Desert, California. Publisher not identified.

Bull, W.B., 2008. Tectonic geomorphology of mountains: a new approach to paleoseismology. John Wiley and Sons, pp. 316.

Bull, W.B., McFadden, L.D., 1977. Tectonic geomorphology north and south of the Garlock Fault, California. In: Proceedings Geomorphology in Arid Regions: Proceedings of the 8th annual Geomorphology Symposium, State University of New York, Binghamton, NY, pp. 115-138.

Burbank, D.W., Anderson, R.S., 2011. Tectonic geomorphology, John Wiley and Sons, pp. 454.

Burbank, D.W., Leland, J., Fielding, E., Anderson, R.S., Brozovic, N., Reid, M.R., Duncan, C., 1996. Bedrock incision, rock uplift and threshold hillslopes in the northwestern Himalayas. Nature, 379(6565), 505-510.

Carretier, S., Regard, V., Vassallo, R., Aguilar, G., Martinod, J., Riquelme, R., Pepin, E., Charrier, R., Herail, G., Farias, M., Guyot, J. L., Vargas, G., Lagane, C., 2013. Slope and climate variability control of erosion in the Andes of central Chile. Geology 41(2), 195-198.

Champagnac, J.D., Valla, P.G., Herman, F., 2014. Late-Cenozoic relief evolution under evolving climate: a review. Tectonophysics 614, 44-65.

Chen, Y.C., Sung, Q. C., Cheng, K.Y., 2003. Along-strike variations of morphotectonic features in the Western Foothills of Taiwan: tectonic implications based on stream-gradient and hypsometric analysis. Geomorphology 56(1-2), 109-137.

Cheng, K.Y., Hung, J.H., Chang, H.C., Tsai, H., Sung, Q.C., 2012. Scale independence of basin hypsometry and steady state topography. Geomorphology 171, 1-11.

Clark, M.K., Royden, L.H., Whipple, K.X., Burchfiel, B.C., Zhang, X., Tang, W., 2006. Use of a regional, relict landscape to measure vertical deformation of the eastern Tibetan Plateau. Journal of Geophysical Research 111(F3), DOI: 10.1029/2005JF000294.

Daxberger, H., Riller, U., 2015. Analysis of geomorphic indices in the southern Central Andes (23°–28° S): Evidence for pervasive Quaternary to Recent deformation in the Puna Plateau. Geomorphology 248, 57-76.

Delunel, R., Van Der Beek, P.A., Carcaillet, J., Bourlès, D.L., Valla, P.G., 2010. Frost-cracking control on catchment denudation rates: Insights from in situ produced 10 Be concentrations in stream sediments (Ecrins–Pelvoux massif, French Western Alps). Earth and Planetary Science Letters 293(1), 72-83.

Dominguez-Gonzalez, L., Andreani, L., Stanek, K.P., Gloaguen, R., 2015. Geomorpho-tectonic evolution of the Jamaican restraining bend. Geomorphology 228, 320-334.

Duvall, A., Kirby, E., Burbank, D., 2004. Tectonic and lithologic controls on bedrock channel profiles and processes in coastal California. Journal of Geophysical Research Earth Surface 109(F3), DOI: 10.1029/2003JF000086.

Eggermont, H., Van Damme, K., and Russell, J.M., 2009. Rwenzori mountains (Mountains of the Moon): headwaters of the White Nile. The Nile, Springer, pp. 243-261.

Flint, J.J., 1974. Stream gradient as a function of order, magnitude, and discharge. Water Resources Research 10(5), 969-973.

Gani, N.D., 2015. Erosion history from incision modeling and river profile morphologies: example from the Tekeze River System, Ethiopian Plateau, East Africa. Arabian Journal of Geosciences 8(12), 11293-11305.

Gani, N.D., Gani, M.R., Abdelsalam, M.G., 2007. Blue Nile incision on the Ethiopian Plateau: pulsed plateau growth, Pliocene uplift, and hominin evolution. GSA today 17(9), 4.

Giaconia, F., Booth-Rea, G., Martinez-Martinez, J.M., Azanon, J.M., Perez-Pena, J.V., 2012. Geomorphic analysis of the Sierra Cabrera, an active pop-up in the constrictional domain of conjugate strike-slip faults: The Palomares and Polopos fault zones (eastern Betics, SE Spain). Tectonophysics 580, 27-42.

Goldrick, G., and Bishop, P., 2007. Regional analysis of bedrock stream long profiles: evaluation of Hack's SL form, and formulation and assessment of an alternative (the DS form). Earth Surface Processes and Landforms 32(5), 649-671.

Hack, J.T., 1973. Stream-profile analysis and stream-gradient index. Journal of Research of the US Geological Survey 1(4), 421-429.

Hare, P.W., Gardner, T.W., 1985. Geomorphic indicators of vertical neotectonism along converging plate margins, Nicoya Peninsula, Costa Rica. In: Morisawa, M., and Hack, J. T., eds., Tectonic geomorphology: Proceedings of the 15th Geomorphology Symposia Series: Boston, Allen and Unwin, pp. 75-104.

Hurtrez, J.E., Sol, C., Lucazeau, F., 1999. Effect of drainage area on hypsometry from an analysis of small-scale drainage basins in the Siwalik Hills (Central Nepal). Earth Surface Processes and Landforms 24(9), 799-808.

Ismail, E.H., Abdelsalam, M.G., 2012. Morpho-tectonic analysis of the Tekeze River and the Blue Nile drainage systems on the Northwestern Plateau, Ethiopia. Journal of African Earth Sciences 69, 34-47.

Jacobs, L., Dewitte, O., Poesen, J., Delvaux, D., Thiery, W., Kervyn, M., 2015. The Rwenzori Mountains, a landslide-prone region? Landslides, 1-18.

Kale, V.S., Shejwalkar, N., 2008. Uplift along the western margin of the Deccan Basalt Province: is there any geomorphometric evidence? Journal of Earth System Science 117(6), 959-971.

Karner, G.D., Byamungu, B.R., Ebinger, C.J., Kampunzu, A.B., Mukasa, R.K., Nyakaana, J., Rubondo, E.N., Upcott, N.M., 2000. Distribution of crustal extension and regional basin architecture of the Albertine rift system, East Africa. Marine and Petroleum Geology 17(10), 1131-1150.

Kaser, G., Noggler, B., 1991. Observations on Speke Glacier, Ruwenzori Range, Uganda. Journal of Glaciology 37(127), 513-518.

Kaser, G., Osmaston, H., 2002. Tropical Glaciers. Cambridge University Press, pp. 188.

Katumwehe, A.B., Abdelsalam, M.G., Atekwana, E.A., 2015. The role of pre-existing Precambrian structures in rift evolution: The Albertine and Rhino grabens, Uganda. Tectonophysics 646, 117-129.

Kaufmann, G., Romanov, D., 2012. Landscape evolution and glaciation of the Rwenzori Mountains, Uganda: insights from numerical modeling. Geomorphology 138(1), 263-275.

Keller, E.A., Pinter, N., 2002. Active Tectonics: Earthquakes, Uplift, and Landscape. New Jersey, Prentice Hall, pp. 362.

Keller, E.A., Pinter, N., Green, D.J., 1997. Active Tectonics, Earthquakes, Uplift, and Landscape. Environmental and Engineering Geoscience 3(3), 463-463.

Kelly, M.A., Russell, J.M., Baber, M.B., Howley, J.A., Loomis, S.E., Zimmerman, S., Nakileza, B., Lukaye, J., 2014. Expanded glaciers during a dry and cold Last Glacial Maximum in equatorial East Africa. Geology 42(6), 519-522.

Kirby, E., Whipple, K.X., 2001. Quantifying differential rock-uplift rates via stream profile analysis. Geology 29(5), 415-418.

Kirby, E., Whipple, K.X., 2012. Expression of active tectonics in erosional landscapes. Journal of Structural Geology 44, 54-75.

Kirby, E., Whipple, K.X., Tang, W.Q., Chen, Z.L., 2003. Distribution of active rock uplift along the eastern margin of the Tibetan Plateau: Inferences from bedrock channel longitudinal profiles. Journal of Geophysical Research: Solid Earth 108(B4), DOI: 10.1029/2001JB000861.

Koehn, D., Link, K., Sachau, T., Passchier, C., Aanyu, K., Spikings, A., Harbinson, R., 2016. The Rwenzori Mountains, a Palaeoproterozoic crustal shear belt crossing the Albertine rift system. International Journal of Earth Sciences, 1-13.

Kusznir, N.J., Roberts, A.M., Morley, C.K., 1995. Forward and reverse modelling of rift basin formation. Geological Society, London, Special Publications 80(1), 33-56.

Lifton, N.A., Chase, C.G., 1992. Tectonic, climatic and lithologic influences on landscape fractal dimension and hypsometry: implications for landscape evolution in the San-Gabriel Mountains, California. Geomorphology 5(1-2), 77-114.

Luo, W., 2000. Quantifying groundwater-sapping landforms with a hypsometric technique. Journal of Geophysical Research: Planets, 105(E1), 1685-1694.

Mahmood, S.A., Gloaguen, R., 2012. Appraisal of active tectonics in Hindu Kush: Insights from DEM derived geomorphic indices and drainage analysis. Geoscience Frontiers 3(4), 407-428.

Molin, P., Corti, G., 2015. Topography, river network and recent fault activity at the margins of the Central Main Ethiopian Rift (East Africa). Tectonophysics 664, 67-82.

Molnar, P., 2009. The state of interactions among tectonics, erosion, and climate: A polemi. GSA Today 19(7), 44-45.

Montgomery, D.R., Brandon, M.T., 2002. Topographic controls on erosion rates in tectonically active mountain ranges. Earth and Planetary Science Letters 201(3-4), 481-489.

Mudd, S.M., Attal, M., Milodowski, D.T., Grieve, S. W.D., Valters, D.A., 2014. A statistical framework to quantify spatial variation in channel gradients using the integral method of channel profile analysis. Journal of Geophysical Research: Earth Surface 119(2), 138-152.

Nexer, M., Authemayou, C., Schildgen, T., Hantoro, W.S., Molliex, S., Delcaillau, B., Pedoja, K., Husson, L., Regard, V., 2015. Evaluation of morphometric proxies for uplift on sequences of coral reef terraces: A case study from Sumba Island (Indonesia). Geomorphology 241, 145-159.

Nyakecho, C., Hagemann, S. G., 2014. An overview of gold systems in Uganda. Australian Journal of Earth Sciences 61(1), 59-88.

Ohmori, H., 1993. Changes in the hypsometric curve through mountain building resulting from concurrent tectonics and denudation. Geomorphology 8(4), 263-277.

Osmaston, H., 1989. Glaciers, glaciations and equilibrium line altitudes on the Ruwenzori. In: Mahaney, W. H., Ed., Quaternary and Environmental Research on East African Mountains: Balkema, CRC Press, pp. 31-104.

Ouchi, S., 1985. Response of alluvial rivers to slow active tectonic movement. Geological Society of America Bulletin 96(4), 504-515.

Pederson, J. L., Tressler, C., 2012. Colorado River long-profile metrics, knickzones and their meaning. Earth and Planetary Science Letters 345, 171-179.

Pedrera, A., Pérez-Peña, J.V., Galindo-Zaldívar, J., Azañón, J.M., Azor, A., 2009. Testing the sensitivity of geomorphic indices in areas of low-rate active folding (eastern Betic Cordillera, Spain). Geomorphology 105(3), 218-231.

Perez-Pena, J.V., Azanon, J.M., Azor, A., 2009a. CalHypso: An ArcGIS extension to calculate hypsometric curves and their statistical moments: Applications to drainage basin analysis in SE Spain. Computers and Geosciences 35(6), 1214-1223.

Perez-Pena, J.V., Azanon, J.M., Azor, A., Delgado, J., Gonzalez-Lodeiro, F., 2009b. Spatial analysis of stream power using GIS: SLk anomaly maps. Earth Surface Processes and Landforms 34(1), 16-25.

Perez-Pena, J.V., Azor, A., Azanon, J.M., Keller, E.A., 2010. Active tectonics in the Sierra Nevada (Betic Cordillera, SE Spain): Insights from geomorphic indexes and drainage pattern analysis. Geomorphology 119(1-2), 74-87.

Perron, J. T., Royden, L., 2013. An integral approach to bedrock river profile analysis. Earth Surface Processes and Landforms 38(6), 570-576.

Ries, W. F., 2013. Location of active faults using geomorphic indices in eroded landscapes, South Taranaki, New Zealand. M.S. Thesis, Victoria University of Wellington, pp. 158.

Ring, U., 2008. Extreme uplift of the Rwenzori Mountains in the East African Rift, Uganda: Structural framework and possible role of glaciations. Tectonics 27(4), DOI: 10.1029/2007TC002176.

Roller, S., Wittmann, H., Kastowski, M., Hinderer, M., 2012. Erosion of the Rwenzori Mountains, East African Rift, from in situ-produced cosmogenic ^{10}Be. Journal of Geophysical Research: Earth Surface 117(F3), DOI: 10.1029/2011JF002117.

Saria, E., Calais, E., Stamps, D.S., Delvaux, D., Hartnady, C.J., 2014. Present-day kinematics of the East African Rift. Journal of Geophysical Research: Solid Earth 119(4), 3584-3600.

Schumm, S.A., Dumont, J.F., Holbrook, J. M., 2002. Active tectonics and alluvial rivers. Cambridge University Press, pp. 276.

Sembroni, A., Molin, P., Pazzaglia, F.J., Faccenna, C., Abebe, B., 2016. Evolution of continental-scale drainage in response to mantle dynamics and surface processes: an example from the Ethiopian Highlands. Geomorphology 261, 12-29.

Silva, P.G., Goy, J.L., Zazo, C., Bardaji, T., 2003. Fault-generated mountain fronts in southeast Spain: geomorphologic assessment of tectonic and seismic activity. Geomorphology 50(1-3), 203-225.

Small, E.E., Anderson, R.S., 1998. Pleistocene relief production in Laramide mountain ranges, western United States. Geology 26(12), 1151-1152.

Snyder, N.P., Whipple, K.X., Tucker, G.E., Merritts, D.J., 2000. Landscape response to tectonic forcing; digital elevation model analysis of stream profiles in the Mendocino triple junction region, Northern California. Geological Society of America Bulletin 112(8), 1250-1263.

Sternai, P., Herman, F., Champagnac, J.D., Fox, M., Salcher, B., Willett, S.D., 2012. Pre-glacial topography of the European Alps. Geology 40(12,), 1067-1070.

Strahler, A.N., 1952. Hypsometric (Area-Altitude) Analysis of Erosional Topography. Geological Society of America Bulletin 63(11), 1117-1142.

Struth, L., Babault, J., Teixell, A., 2015. Drainage reorganization during mountain building in the river system of the Eastern Cordillera of the Colombian Andes. Geomorphology 250, 370-383.

Taylor, R.G., Mileham, L., Tindimugaya, C., Mwebembezi, L., 2009. Recent glacial recession and its impact on alpine riverflow in the Rwenzori Mountains of Uganda. Journal of African Earth Sciences 55(3), 205-213.

Van Damme, D., Pickford, M., 2003. The late Cenozoic Thiaridae (Mollusca, Gastropoda, Cerithioidea) of the Albertine Rift Valley (Uganda-Congo) and their bearing on the origin and evolution of the Tanganyikan thalassoid malacofauna. Hydrobiologia 498(1-3), 1-83.

Wallner, H., Schmeling, H., 2010. Rift induced delamination of mantle lithosphere and crustal uplift: a new mechanism for explaining Rwenzori Mountains' extreme elevation? International Journal of Earth Sciences 99(7), 1511-1524.

Westerhof, A.B., Härmä, P., Isabirye, E., Katto, E., Koistinen, T., Kuosmanen, E., Lehto, T., Lehtonen, M. I., Mäkitie, H., Manninen, T., 2014. Geology and Geodynamic Development of Uganda with Explanation of the 1: 1,000,000 Scale Geological Map, Uganda. Geological Survey of Finland, Special Paper 55.

Whipple, K.X., 2004. Bedrock rivers and the geomorphology of active orogens. Annual Review of Earth and Planetary Sciences 32, 151-185.

Whipple, K.X., Tucker, G.E., 1999. Dynamics of the stream-power river incision model: Implications for height limits of mountain ranges, landscape response timescales, and research needs. Journal of Geophysical Research-Solid Earth 104(B8), 17661-17674.

Willett, S.D., McCoy, S.W., Perron, J.T., Goren, L., Chen, C.Y., 2014. Dynamic reorganization of river basins. Science 343(6175), 1248765.

Willgoose, G., Hancock, G., 1998. Revisiting the hypsometric curve as an indicator of form and process in transport-limited catchment. Earth Surface Processes and Landforms 23(7), 611-623.

Wobus, C., Whipple, K.X., Kirby, E., Snyder, N., Johnson, J., Spyropolou, K., Crosby, B., Sheehan, D., 2006. Tectonics from topography: procedures, promise, and pitfalls. Geological Society of America Special Papers 398, 55-74.

Yang, R., Willett, S.D., Goren, L., 2015. In situ low-relief landscape formation as a result of river network disruption. Nature 520(7548), 526-529.

CHAPTER III

SPATIAL AND TEMPORAL VARIATION OF TECTONIC UPLIFT IN THE SOUTHEASTERN ETHIOPIAN PLATEAU FROM MORPHOTECTONIC ANALYSIS

3.0. Abstract

We use morphotectonic analysis to study the tectonic uplift history of the southeastern Ethiopian Plateau (SEEP). Based on studies conducted on the Northwestern Ethiopian Plateau, steady-state and pulsed tectonic uplift models were proposed to explain the growth of the plateau since ~30 Ma. We test these two models for the largely unknown SEEP. We present the first quantitative morphotectonic study of the SEEP. First, in order to infer the spatial distribution of the tectonic uplift rates, we extract geomorphic proxies including normalized steepness index k_{sn}, hypsometric integral *HI*, and chi integral χ from the Advanced Spaceborne Thermal Emission and Reflection Radiometer (ASTER) digital elevation model (DEM). Second, we compare these rates with the thickness of flood basalt that we estimated from geological maps. Third, to constrain the timing of regional tectonic uplift, we develop a knickpoint celerity model. Fourth, we compare our results to those from the Northwestern Ethiopian Plateau to suggest a possible mechanism to explain regional tectonic uplift of the entire Ethiopian Plateau. We find an increase in tectonic uplift rates from the southeastern escarpments of the Afar Depression in the northeast to that of the Main Ethiopian Rift to the southwest.

We identify three regional tectonic uplift events at ~11.7, ~6.5, and ~4.5 Ma recorded by the development of regionally distributed knickpoints. This is in good agreement with ages of tectonic uplift events reported from the Northwestern Ethiopian Plateau.

3.1. Introduction

The development of geomorphic features in response to tectonic uplift provides important information regarding nature and spatial and temporal distributions of tectonic forces in contractional and extensional tectonic regimes. The distribution of tectonic activities in regions experiencing tectonic uplift can be mapped through geomorphic proxies, including normalized steepness index k_{sn} (Whipple, 2004; Kirby and Whipple, 2012), hypsometric integral *HI* (Strahler, 1952; Gao et al., 2016), and chi integral χ (Perron and Royden, 2013; Willett et al., 2014). In addition, celerity modeling of knickpoints allows for establishing end-member time constraint for the changes of tectonic uplift rates (Berlin and Anderson, 2007; Miller et al., 2012). Here, we use these approaches (in addition to information about precipitation and lithology) to establish the spatial and temporal distribution of the tectonic uplift in the tectonically active southeastern Ethiopian Plateau (SEEP).

The Ethiopian Plateau is divided by the Main Ethiopia Rift (MER) and the Afar Depression into the Northwestern Ethiopian Plateau and the SEEP (Fig. 1A). The landscape of this region has been shaped by tectonic uplift, volcanism, and extensional deformation associated with the development of the East African Rift System (EARS) (Fig. 1A; Wolfenden et al., 2004; Simmons et al., 2007; Prave et al., 2016). The development and preservation of such an anomalously high plateau (average elevation of ~2.5 km) within a continental rift setting are caused by the dynamics of the Afar mantle plume (Ebinger and Casey, 2001; Sengor, 2001; Faccenna et al., 2013). Morphotectonic studies to constrain the tectonic uplift history of the Ethiopian Plateau have remained considerably sparse. Hence, several fundamental questions regarding the tectonic uplift history of the plateau remain unanswered. These include:

- Was the growth of the Ethiopian Plateau steady or episodic? Results from (U-Th)/He thermochronology studies by Pik et al. (2003) suggest steady-state plateau growth for the Northwestern Ethiopian Plateau since ~29 Ma resulting in ~1 km uplift since then. Conversely, morphotectonic analysis by Gani et al. (2007) and Ismail and Abdelsalam (2012) reported multistage and accelerated growth of the Northwestern Ethiopian Plateau at 30–10 Ma, 10–6 Ma, and 6 Ma – present. This excludes the portion of the plateau away from the escarpment of the MER and the Afar Depression (toward the lowlands of Sudan) where the steady-state model is applicable.

- What is the distribution pattern of the tectonic uplift in relation to the MER and the Afar Depression? The $^{40}Ar/^{39}Ar$ ages and seismic data suggest northeastward propagation of the MER into the Afar Depression. This implies a more active extension into the northern MER than in the southern MER (Wolfenden et al., 2004; Mackenzie et al., 2005). Nevertheless, structural analysis, numerical models, and ^{14}C radiometric dating suggest that extension in the northern MER and the Afar Depression is more advanced than the central and southern MER. This is evidenced from the presence of more pronounced within-rift faults in the former. This proposes a southwestward rift propagation from the northern MER to the southern MER (Hayward and Ebinger, 1996; Keranen and Klemperer, 2008; Agostini et al., 2011; Philippon et al., 2014).

We aim to answer these questions using morphotectonic analysis through the application of various geomorphic proxies (k_{sn}, *HI*, and χ) and knickpoint celerity modeling. For this, we (i) map the spatial and temporal distribution pattern of the tectonic uplift rates in the SEEP; (ii) establish the timing of tectonic uplift in the plateau since ~12 Ma; (iii) examine the relationship between the tectonic uplift and volcanism; and (iv) compare the tectonic uplift history of the SEEP to that of the Northwestern Ethiopian Plateau.

3.2. Geologic settings

The topography of the SEEP results from geological events that include the development of a Precambrian orogenic belt (the Arabian-Nubian Shield), Paleozoic-Mesozoic rifting and sedimentation (the Karoo rifting event), and Cenozoic rifting and magmatism (the EARS). Notably, the topography of SEEP is highly influenced by the Cenozoic tectono-magmatic events of the EARS. The plateau is bordered in the northwest by the MER and the Afar Depression, which represent the tectonic boundary between the Nubian and Somalian plates. The two plates are currently moving away from each other at a rate of 4 to 6 mm/y (Kogan et al., 2012). The MER and the Afar Depression asymmetrically divide the ~1000-km-wide Ethiopian Plateau into the SEEP and the Northwestern Ethiopian Plateau (Fig. 1A). Based on its general orientation, the MER is divided into northern, central, and southern segments that developed at different times during the Miocene (Fig. 1B; Boccaletti et al., 1998).

3.2.1. Geomorphological setting of the southeastern Ethiopian Plateau (SEEP)

The SEEP is bounded by the southeastern escarpment of the MER and the Afar Depression in the northwest and by the Ogaden Basin to the southeast (Fig. 1A). It is deeply incised by the drainage systems of the Jubba and Shabele rivers, which originate respectively from the Bale and Ahmar mountains. Within the SEEP, these rivers span over an area of ~373,000 km^2 (Fig. 1B). Drainage incision reaches up to 900 m in the Bale and Ahmar mountains, reflecting rapid tectonic uplift along the southeastern escarpment of the MER and the Afar Depression (Mège et al., 2015).

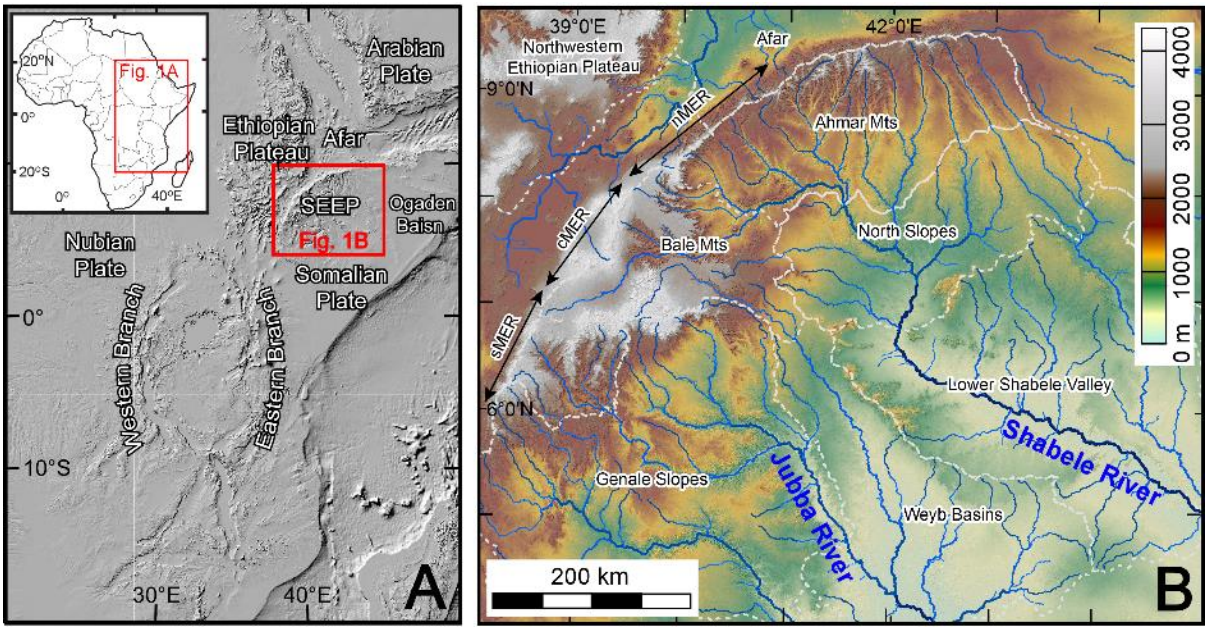

Figure 3- 1(A) Digital elevation model (DEM), extracted from the Earth Topography 1 arc second (ETOPO 1) data (1 km spatial resolution), showing the locations of the Arabian Plate, Nubian Plate, Somalian Plate, western and eastern branches, Afar Depression, and Ethiopian Plateau. (B) Digital elevation model (DEM) extracted from the Advanced Spaceborne Thermal Emission and Reflection Radiometer (ASTER) data (30-m spatial resolution) showing major geomorphological features of the southeastern Ethiopian Plateau (SEEP). The white dot lines show the physiographic segments of the SEEP, and the black lines with arrows show the southern (sMER), central (cMER), and northern (nMER) segments of the Main Ethiopian Rift (MER).

The SEEP and the Northwestern Ethiopian Plateau form a broad dome, hypothesized to be the result of the impinging of the Afar mantle plume beneath the lithosphere of the Arabian-Nubian Shield (Sembroni et al., 2016a). The highest regions in the plateau are the Bale and Ahmar mountains, reaching over 4.0 km in elevation. The elevation decreases toward the southeast, and it is only about 300 m at the Ethiopia–Somalia border (Mège et al., 2015). For the purpose of the description of the variation in geomorphic proxies, we divide the SEEP into six physiographic provinces. These are the Bale and Ahmar mountains, the Genale and North slopes, and the Weyb basins and the lower Shabele valley (Fig. 1B).

3.2.2. Lithology

The SEEP is dominated by (i) Precambrian basement rocks, (ii) Paleozoic – Mesozoic sedimentary rocks, and (iii) Cenozoic volcanic rocks. The Precambrian basement rocks are

exposed mostly in the Genale slopes and the Ahmar mountains from uplift and exhumation along the southeastern escarpment of the MER and the Afar Depression (Fig. 2). These rocks include variably metamorphosed volcano-sedimentary and plutonic rocks that were formed during the 900–500 Ma East African orogeny (Stern, 1994). The Precambrian basement rocks are overlain by Paleozoic–Mesozoic sedimentary rocks deposited in two sedimentary episodes. These include the late Carboniferous– Jurassic Karoo rifting episode and the Late Jurassic Gondwana fragmentation episode (e.g., Worku and Astin, 1992). The Karoo sedimentary rocks are strictly continental in nature and were deposited in narrow grabens between horst structures dominated by the Precambrian basement rocks. No Karoo sedimentary rocks are exposed to the surface in the SEEP, but they are found in the subsurface as reported from drilling and seismic data (Worku and Astin, 1992). Extensive exposures of Mesozoic sedimentary rocks are found in the SEEP, especially in the Ahmar mountains, the North slopes, the lower Shabele valley, and the Weyb

basins (Fig. 2).

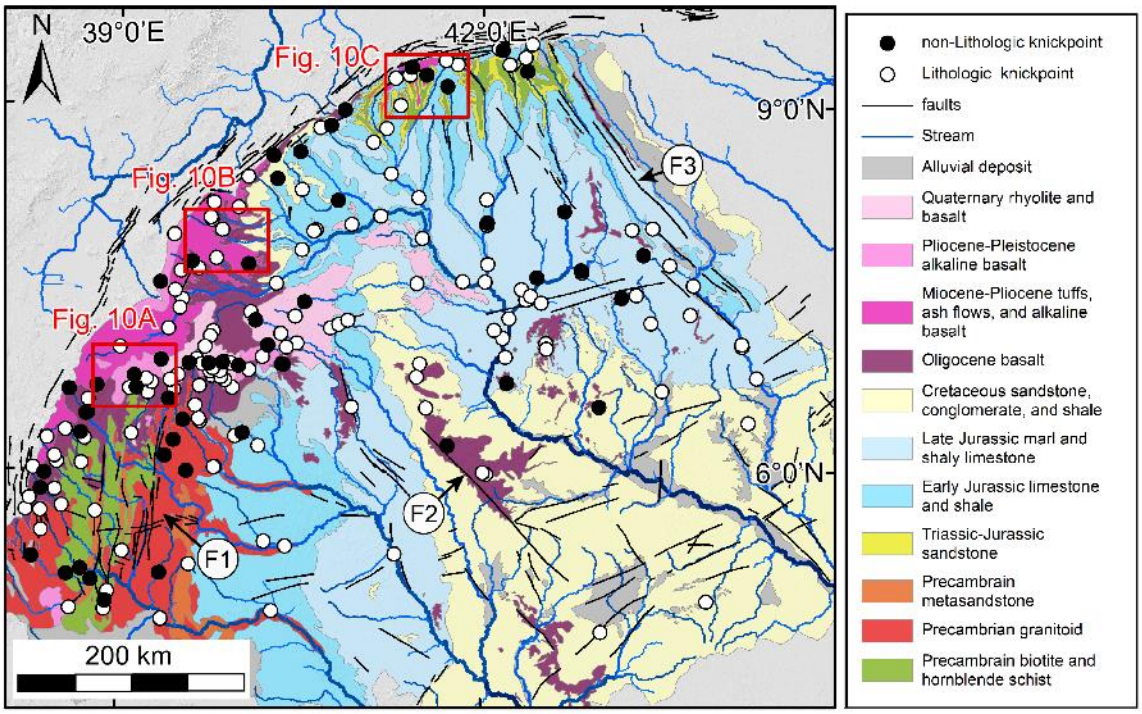

Figure 3- 2 Geologic map of the southeastern Ethiopian Plateau (SEEP), modified from the geologic map of Ethiopia (Kazmin, 1973;Tefera et al., 1996). F1 = Genale Fault Belt. F2 = Weyb Fault Belt. F3 = Marda fault belt.

Isolated basaltic remnants of different sizes are found in different parts of the SEEP unconformably overlying the Mesozoic sedimentary rocks or the Precambrian basement rocks (Fig. 2). These basalts range in age from Oligocene to Quaternary (Tefera et al., 1996; Hofmann et al., 1997; Corti, 2009; Furman et al., 2016). The Oligocene basalts are scattered as isolated outcrops in the parts of the SEEP that are preserved from the southeastern escarpment (Fig. 2). Miocene and Pliocene shield volcanoes supplied lava flows to the Northwestern Ethiopian Plateau (Kieffer et al., 2004; Nelson et al., 2008), while Quaternary basalts are mostly restricted to the MER axis and southeastern escarpment, especially the Bale mountains (Fig. 2; Rooney et al., 2012).

3.2.3. Major structural elements

The SEEP is affected by three sets of faults. The first set is NW-trending and comprises the Marda fault belt, which dissects the eastern portion of the Ahmar mountains and the North slopes (Fig. 2). The second set of faults is the Weyb Fault Belt, which is exposed dominantly between the Weyb basins and the Shabele valley (Fig. 2). The third set is the Genale fault belt, which is found on the western side of the Genale slopes (Fig. 2). The Marda fault belt is ~150 km long and up to 2 km wide (Mège et al., 2015). It is reported as a Precambrian deformation zone that has been reactivated during the Phanerozoic (Purcell, 1976; Boccaletti et al., 1991).

Another dominant structural element in the SEEP is the NE-trending border faults of the MER and the Afar Depression, which form the boundary between the rift basin and the SEEP (Fig. 2). The orientation of these border faults changes gradually from ~N40°E in the northern MER to N20-35°E in the southern MER (Corti, 2009).

3.2.4. Uplift history of the southeastern Ethiopian Plateau (SEEP)

The topography of the Ethiopian Plateau is shaped by several major tectonic and magmatic events including (i) the upwelling of one or two mantle plumes that impinged the base of the Arabian-Nubian shield lithosphere during the Oligocene (Simmons et al., 2007) and triggered the eruption of more than 600,000 km^2 of flood basalt (Ukstins et al., 2002; Bonini et al., 2005; Abebe et al., 2010). As much as 1 to 2 km of uplift is suggested to have occurred before the emplacement of the flood basalt ~30 Ma. Geophysical data suggest that half of the 1-2 km Oligocene uplift was formed caused by thermal perturbation of the lithosphere above the rising mantle plume (Sengor, 2001; Dugda et al., 2007). Another ~1 km of uplift is suggested to have occurred after the emplacement of the flood basalt from denudation-derived crustal unloading (Gani et al., 2007). These events also includes (ii) more localized volcanic activity from 30 Ma to about 10 Ma leading to the formation of shield volcanoes (Corti, 2009), and (iii) the initiation of

the MER in the late Miocene that proceeded until present, leading to the development of rift border faults and rift-flank uplift (Woldegabriel et al., 1990; Ebinger and Casey, 2001; Bonini et al., 2005; Pik et al., 2008).

3.3. Climate

The climate of Ethiopia is mainly controlled by the seasonal migration of the Intertropical Convergence Zone (ITCZ) and related atmospheric circulations (Beltrando and Camberlin, 1993). Because of the large variation of topography in the SEEP, the change in climate between the lowlands and the highlands is considerable (Fig. 3). Based on the Köppen climate classification, the SEEP can be classified into four major categories (Peel et al., 2007; Mège et al., 2015). The North and the Genale slopes have tropical A type climate with constant high temperature, whereas the Weyb basins and the lower Shabele valley have an arid to semiarid B type climate. The Bale and the Ahmar mountains have a temperate C type climate and, the peaks of these

mountains have low temperature H type climate (Fig. 3; Fazzini et al., 2015).

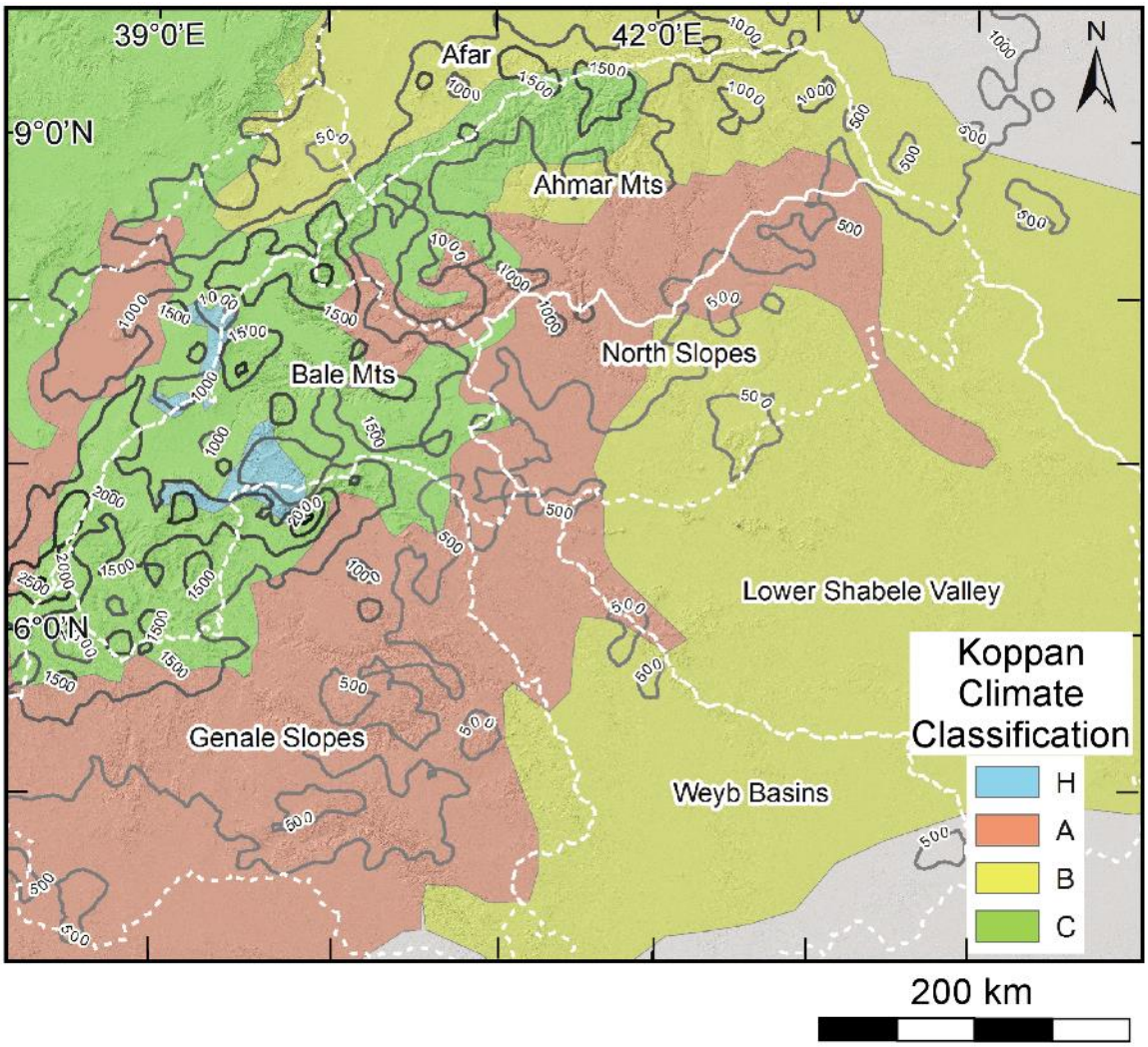

Figure 3- 3 Averaged precipitation in last 10 years from Tropical Rainfall Measuring Mission (TRMM) and Köppen Climate classification (Fazzini et al., 2015) of the southeastern Ethiopian Plateau (SEEP), including types A, B, C, and H.

The annual precipitation in the SEEP also varies significantly. From Tropical Rainfall Measuring Mission (TRMM) satellite data, the 10-year average rainfall in the SEEP is ~700 mm/y whereas ~817 mm/y is recorded for entire Ethiopia (Fazzini et al., 2015). The highest precipitation rate of ~2500 mm/y is received at the peaks of Bale mountains, and the precipitation rate decreases southeastward with decreasing elevation.

3.4. Data and methods

First, we used the geomorphic proxies including k_{sn}, *HI*, and χ to estimate the pattern of tectonic uplift rates in the SEEP. Second, we estimated the thickness of the Cenozoic basaltic flows to examine the relationship between magmatism and tectonic uplift rates. Third, we calculated end-members time constraints for different tectonic uplift stages using knickpoint celerity modeling. We used the Advanced Spaceborne Thermal Emission and Reflection Radiometer (ASTER) digital elevation model (DEM) that has a spatial resolution of 30 m, Sentinel-2 satellite multispectral remote sensing data that have a spatial resolution of 20 m, and 1:2,000,000 geological map of Ethiopia (Kazmin, 1973; Tefera et al., 1996). We used a total of 140 drainage basins and 121 streams from the entire SEEP in this study (Fig. 4). The drainage basins are labeled 1 to 140 from northeast to southwest (Fig. 4).

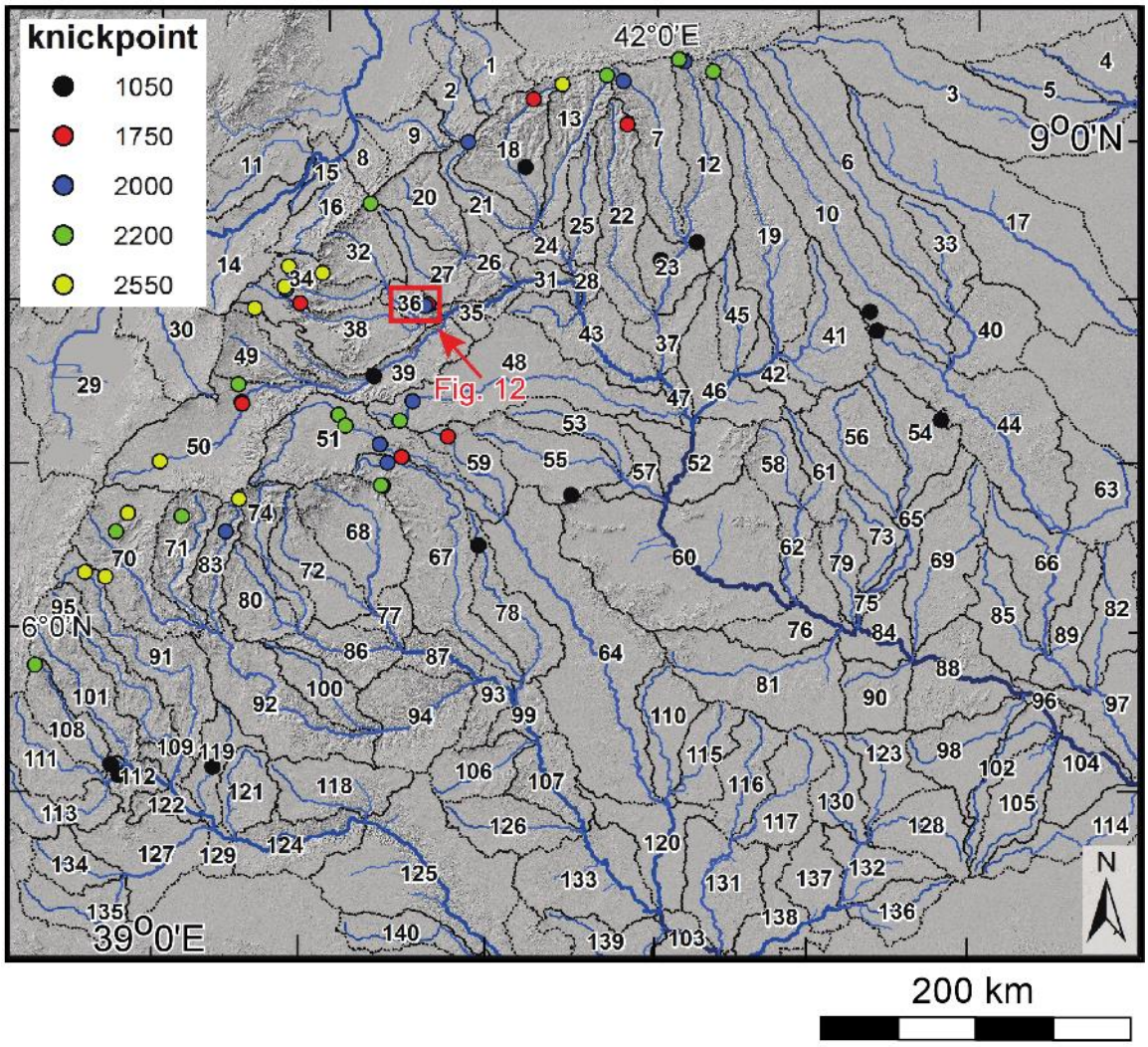

Figure 3- 4 Digital elevation model (DEM) extracted from the Advanced Spaceborne Thermal Emission and Reflection Radiometer (ASTER) data (30m spatial resolution) of the southeastern Ethiopian Plateau (SEEP), showing the Jubba and the Shabele rivers and the 140 drainage basins used in this study. The knickpoints with different elevations are also shown along the streams.

3.4.1. Geomorphic proxies

3.4.1.1. Normalized steepness index k_{sn}

The k_{sn} of streams can be used as an indicator of the amount of fluvial incision caused by the change in tectonic uplift, base level, climate, and lithology (Hack, 1973; Flint, 1974; Wobus et al., 2006). The fluvial bedrock incision rate E taken to be the power-law function of the drainage area A and the channel slope S (Howard et al., 1994; Snyder et al., 2000):

$$E = KA^m S^n \quad (8)$$

where *K* describes the erosional efficiency that depends on lithology, hydraulic roughness of the stream bed, precipitation, and associated climate characteristics (Whipple and Tucker, 1999). The exponents *n* and *m* are positive empirical constants (Whipple and Tucker, 1999). Also, the rate of change of elevation of the stream bed *dz/dt* records the difference between the rate of tectonic uplift rate and the incision rate (Whipple, 2004; Cyr et al., 2010). Thus, the time variation of the stream elevation can be described as

$$\frac{dz}{dt} = U - E = U - KA^m S^n \quad (9)$$

where *U* denotes the tectonic uplift rate. Under steady-state, $U = E$. Hence, Eq. (2) can be solved for the equilibrium slope S_e:

$$S_e = (U/K)^{1/n} A^{-m/n} \quad (10)$$

where *m/n* defines the concavity θ of the stream longitudinal profile at the equilibrium state of uniform tectonic uplift and erodibility, whereas the coefficient $(U/K)^{1/n}$ defines the steepness of the stream longitudinal profile. The power-law function described in Eq.(3) is found in different tectonic settings to be empirically expressed as

$$S = k_s A^{-\theta} \quad (11)$$

where $k_s = (U/K)^{1/n}$, and $\theta = m/n$.

The steepness of the stream longitudinal profile k_s is found to be proportional to the tectonic uplift rate in steady-state topography (Snyder et al., 2000; Wobus et al., 2006; Kirby and Whipple, 2012). The variation in θ of the stream longitudinal profile results in a large variation in the k_s values. Therefore, it has become accepted practice to use a mean representative value of θ as a reference for the calculation of the normalized steepness index k_{sn}. Here, we first extracted the k_{sn} values from the ASTER DEM for the streams on the shoulder of the SEEP using

the stream profiler software (Snyder et al., 2000; Kirby et al., 2003; Wobus et al., 2006; Fig 5A). Subsequently, to illustrate their distribution pattern throughout the plateau, we interpolated the k_{sn}

values from all streams in each 1000 m of the SEEP using the nearest-neighbor algorithm (Fig. 5B).

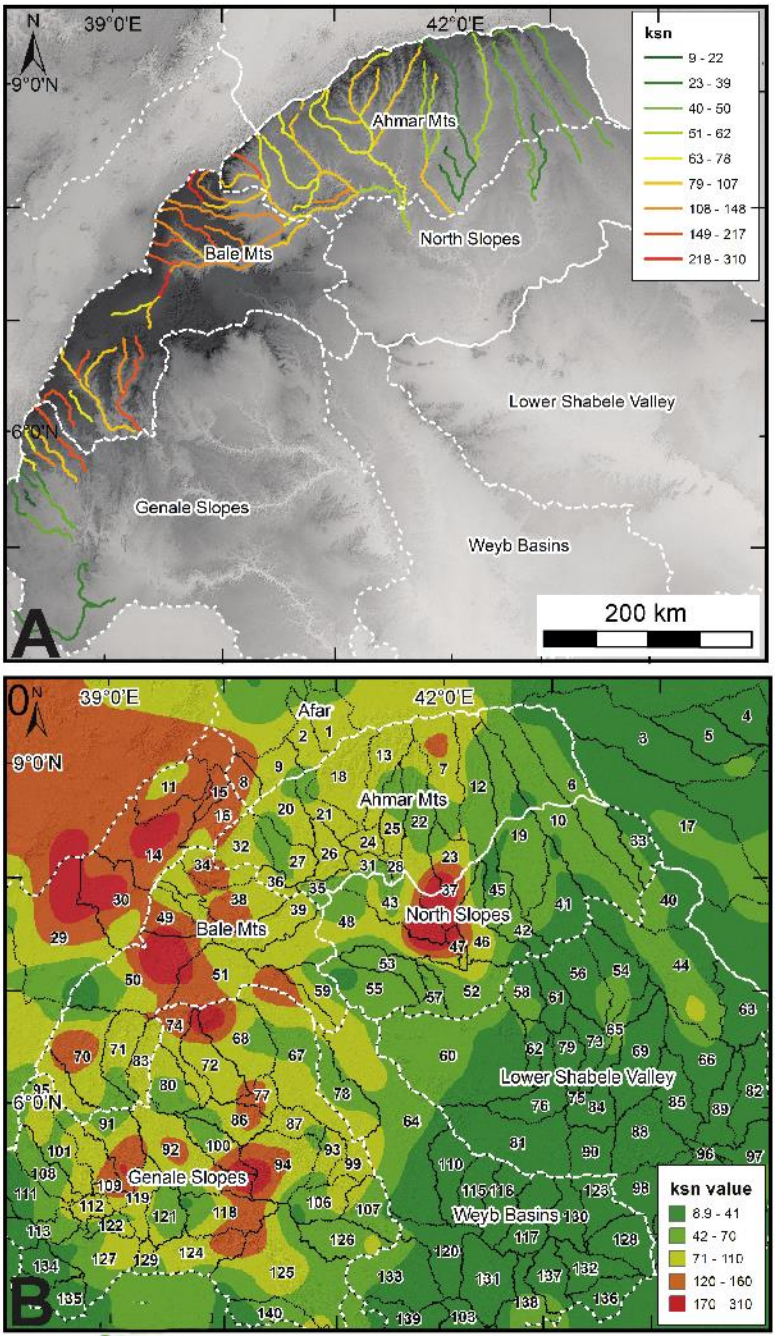

Figure 3- 5 Normalized steepness index k_{sn} maps with streams along the southeastern escarpment of the Main Ethiopian Rift (MER) (A) and nearest-neighbor interpolated ksn map (B) of all streams (stream order >3) (B) of the southeastern Ethiopian Plateau (SEEP).

3.4.1.2. Hypsometric integral HI

The *HI* evaluates the surface distribution of landmass at different elevations within a drainage basin (Strahler, 1952). It is calculated as the proportion of the volume of the landmass within the drainage basin contained within a horizontal slab with a given thickness *h* (Strahler, 1952). It can be expressed as

$$HI = \int_{Min\ el.}^{Max\ el.} A_e\ \Delta h \tag{6}$$

where A_e is the ratio of the basin drainage area at a given elevation *h* to the area of the entire drainage basin. The *HI* is the cumulative volume of the landmass within the drainage basin contained between a contour line representing a maximum elevation *Max el.* and a contour line representing a minimum elevation *Min el.* With constraints on climate and lithology within drainage basins under consideration, high *HI* values are interpreted to be associated with drainage basins that are tectonically young and active. Alternatively, low *HI* values are interpreted to be associated with drainage basins dominated by mature topography (Lifton and Chase, 1992; Ohmori, 1993; Chen et al., 2003).

We extracted *HI* values for all of the drainage basins in the SEEP from the ASTER DEM using CalHypso software (Perez-Pena et al., 2009) (Fig. 6).

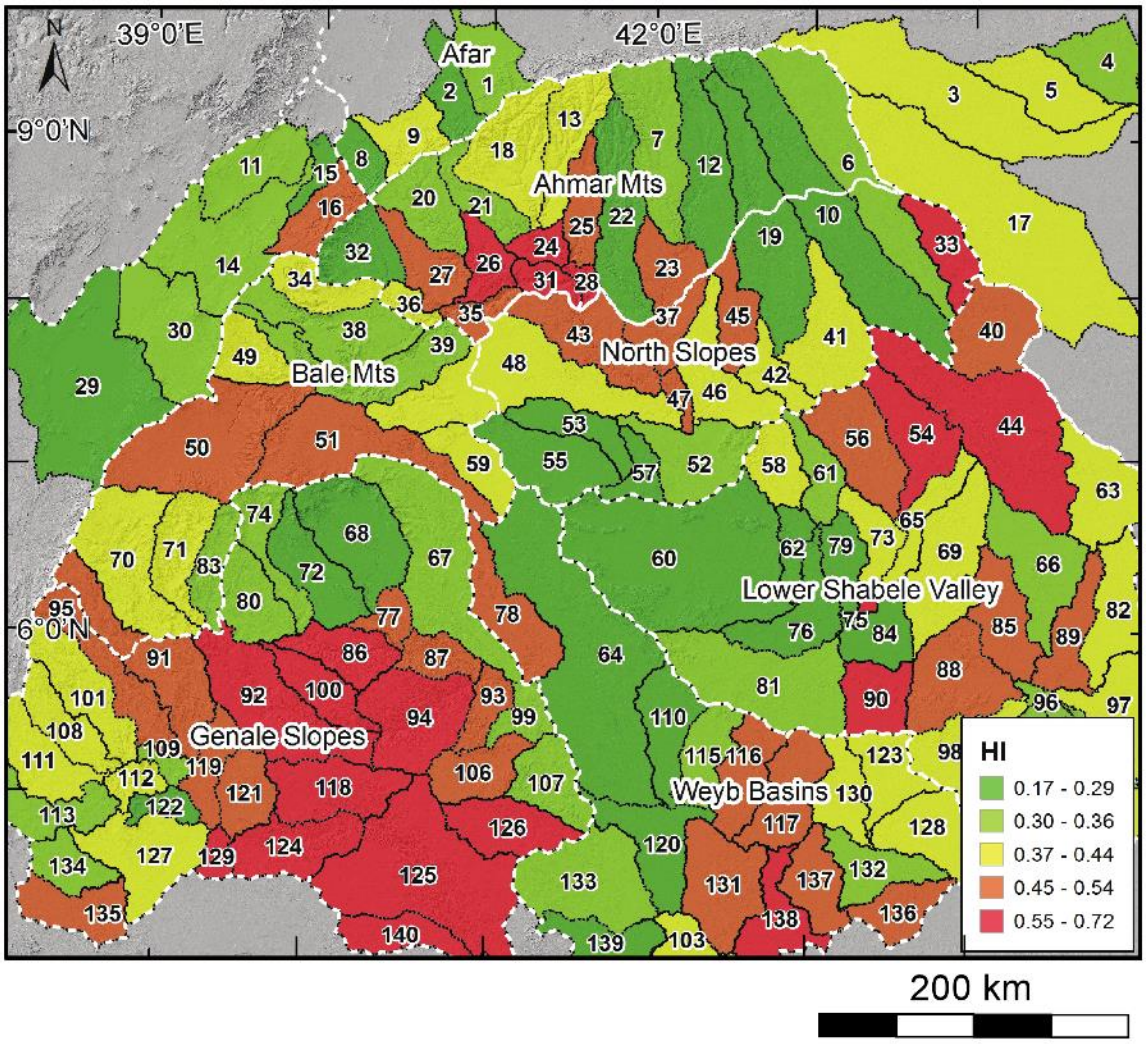

Figure 3- 6 Hypsometric integral (HI) map of the southeastern Ethiopian Plateau (SEEP), showing individual value for each drainage basin.

3.4.1.3. Chi analysis χ

The geomorphic proxy χ is useful to evaluate the dynamic state of the divide of drainage basins (Harkins et al., 2007; Perron and Royden, 2013; Willett et al., 2014). Under steady-state, Eq. (1) can also be expressed as

$$S = \frac{dz}{dx} = (\frac{E}{K})^{\frac{1}{n}} A^{\frac{-m}{n}} \quad (7)$$

where z is the elevation and x is the longitudinal coordinate (Whipple and Tucker, 1999). The χ can be expressed by integrating both sides of Eq. (3):

$$z(x) = z_b + (\frac{E}{KA_0^m})^{\frac{1}{n}}\boldsymbol{\chi} \tag{8a}$$

with

$$\chi = \int_{x_b}^{x} (\frac{A_0}{A(x)})^{\frac{m}{n}}\, dx \tag{8b}$$

$$M\chi = (\frac{E}{KA_0^m})^{\frac{1}{n}} \tag{8c}$$

where A_0 is a reference area within the drainage basin and z_b is the elevation at the outlet of the basin (Perron and Royden, 2013). Hence, given the linear form of Eq. (8a), χ describes the modern distribution of drainage area, in the units of length (Willett et al., 2014). Although recent work from Whipple et al. (2017) reported that local metrics of across drainage divide difference in erosion rate (e.g., mean headwater local relief and channel bed elevation at a reference drainage area) may be more useful to predict instantaneous divide motion, various χ values are suggestive of long-term divide migration direction from low χ value toward high χ value (Willett et al., 2014). Such divide migration usually leads to measurable perturbation of channel profiles

and local relief as demonstrated by Whipple et al. (2017).

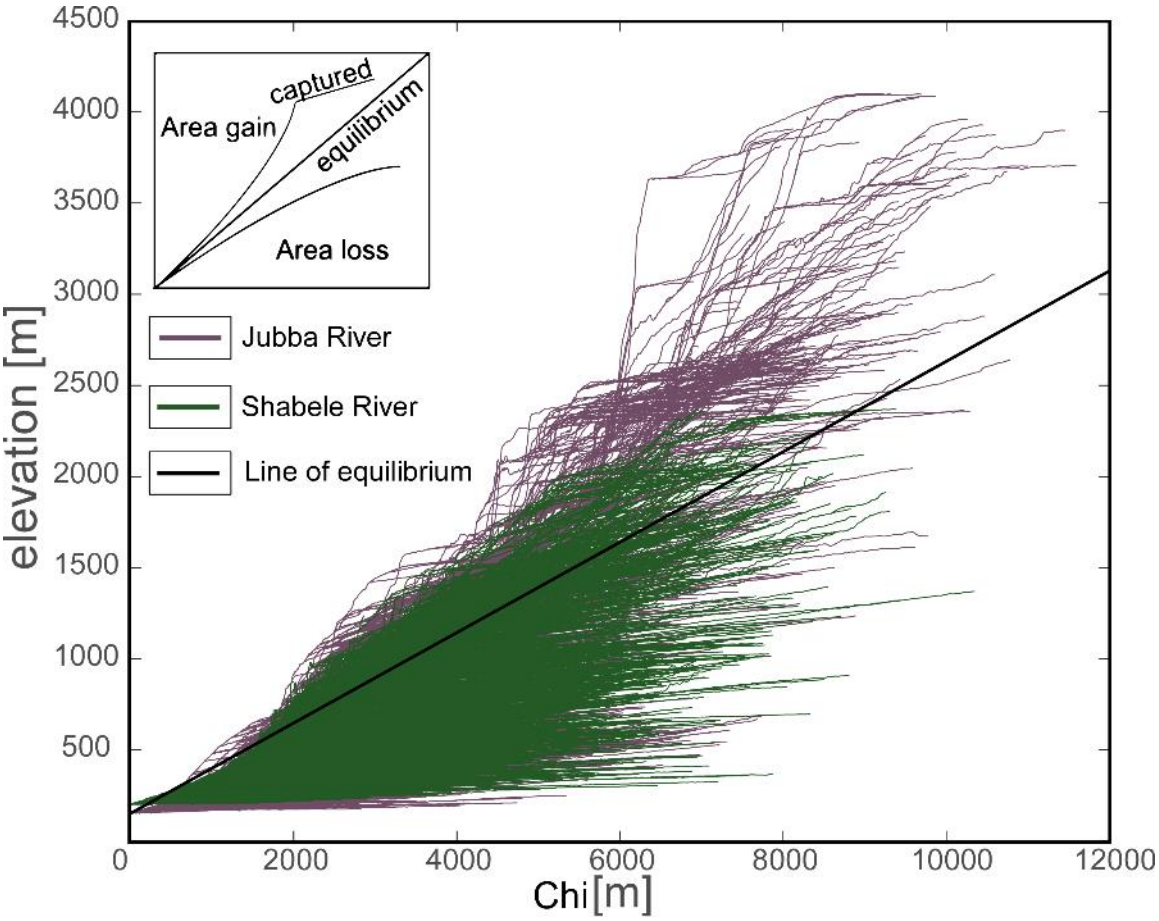

Figure 3- 7 χ-elevation plot of the Jubba (purple) and the Shabele rivers (green), showing corresponding aggressor (basins that are gaining area) and victim (basins that are losing area) respectively. The inset image illustrates the characteristic signature, modified from Willett et al. (2014).

We extracted the χ values from the ASTER DEM for the drainage basins of the SEEP (Fig. 7) using the code of Mudd et al. (2014). We applied the AICC-collinearity tests, as suggested by Mudd et al. (2014). We also explored the m/n ratio from 0.15 to 0.75 with an interval of 0.05 and found the best fit for this ratio to be 0.4 (Appendice 1). Additionally, we generated a χ vs. elevation plot for the Shabele and Jubba river drainage basins (Fig. 8). We used this plot to understand migration of drainage divides that might be caused by shifting of tectonic uplift, climate, and sediment dynamics. The tributaries within a given drainage basin that have reached steady-state will have straight lines on such a plot (Willett et al., 2014). In contrast,

drainage basins that have tributaries under transient differential fluvial erosion (possibly caused by high tectonic uplift rate) will have lines with more than one slope and their plot will depart from the line of equilibrium (Schmidt et al., 2015).

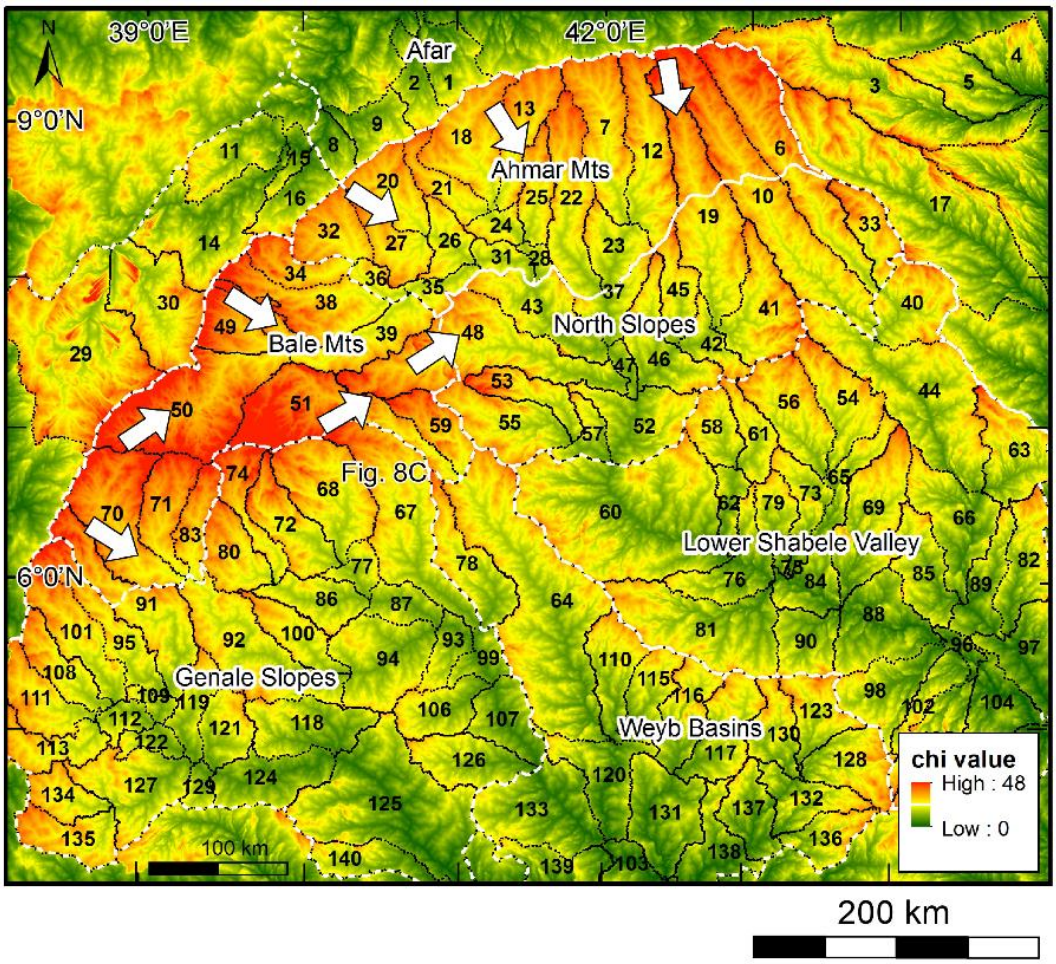

Figure 3- 8 A) Chi (χ) map of the southeastern Ethiopian Plateau (SEEP). The arrows illustrate the migrating direction of the drainage divides.

3.4.2. Oligocene flood basalt flood

The Oligocene (~30 Ma) volcanic event (Hofmann et al., 1997) resulted in the extrusion of extensive flood basalt within the Ethiopian Plateau (Mengesha et al., 1996). Here, we reconstructed the thickness of the flood basalt within the SEEP (Fig. 9A) by integrating

geological data from the 1:2,000,000 geological map of Ethiopia (Kazmin, 1973; Tefera, 1996) with our observations from multispectral Sentinel-2 images (Drusch et al., 2012) and elevation data from the ASTER DEM. This flood basalt, which can be as thick as ~1.5 km, is underlain by the Mesozoic sedimentary rocks or the Precambrian basement rocks and is overlain by isolated plateaus of Miocene-Quaternary basaltic flows (Fig. 2). Assuming no erosional unconformity in the flood basalt, we established its basal surface by first identifying this contact at different locations using the geological map of Ethiopia (Kazmin, 1973; Tefera, 1996) and our interpretation from the Sentinel-2 images. Some of the Oligocene basalt is preserved along the Marda fault belt and the southeastern border fault of MER in the form of dike swarms rather than volcanics (Mège et al., 2015). Hence, these are excluded from the construction of the lower contact of the flood basalt. Additionally, because of difficulty in accurately identifying the upper contact, this surface is contracting with fewer discrete points compared to the lower contact (Fig. 9A). Then we interpolated the elevations of these discrete points (green in Fig. 9A) in the ASTER DEM by the nearest-neighbor method. Similarly, we established the top surface of the Oligocene flood basalt with the same procedure we used for the basal surface, by identifying discrete points (red dots in Fig. 9A) presenting the contact between the Oligocene flood basalt and the overlying Miocene-Quaternary basalt. Here, we present four examples highlighting how we used the Sentinel- 2A images to identify the basal and top contacts of the Oligocene flood basalt. Figures 9B and C are examples of determining these contacts within incised channel, whereas Figs. 9D and E are examples of identifying these contacts within inverted valleys. Subsequently, we estimated the thickness of the Oligocene flood basalt by subtracting the elevation of its basal surface from the elevation of its top surface.

3.4.3. Knickpoint celerity model

We developed a knickpoint celerity model for the SEEP to examine whether or not the topographic growth of the plateau (hence the tectonic uplift rate) is steady or episodic. We utilized the knickpoints identified in the longitudinal profiles of the tributaries of the Shabele River because of the availability of geochronological data for the Quaternary flood basalt (Woldegabriel et al., 1990; Alemu and Abebe, 2007). Knickpoints that are regionally preserved within a limited range of elevation are indicative of changes in lithology, precipitation, tectonic uplift rate, or drainage reorganization related to change in base level. In this case, the upstream maintains the slope that existed before the occurrence of the change, while the slope in the downstream is continuously adjusted to the ongoing change (Crosby and Whipple, 2006; Kirby and Whipple, 2012). This will result in the migration of knickpoints in the direction of upstream along the entire fluvial drainage network as a wave of erosion (Niemann et al., 2001). Derived from Eq. (1), knickpoint celerity *dx/dt* can be expressed as

$$\frac{dx}{dt} = KA^m \tag{9}$$

where *A* is the basin drainage area, *m* is the nondimensional constant, and *K* is the erosion coefficient. Previous works (Whipple et al., 2000; Berlin and Anderson, 2007; Sembroni et al., 2016b; Beeson et al., 2017) considered *n* to equal 1 in Eq. (1).

To estimate the ages of different tectonic uplift events in the SEEP, we used Eq. (9) to build the knickpoint celerity model for the SEEP following a three-step approach:

- Using the longitudinal profiles, we identified knickpoints along the major streams (streams with order >3) in the drainage basins of the SEEP. We used the geologic map in Fig. 2 to eliminate the knickpoints associated with lithological contacts and faults as exemplified by Figs. 10A-C. These include examples from the Bale mountains (Fig. 10A and B) and the Ahmar mountains (Fig. 10D). As has been used by Kirby and Whipple (2012), we used the plot of log S -

log A of the longitudinal profile of streams to identify the locations of slope-break pattern knickpoints within similar rock units (Appendix 2).

- Using the knickpoints along the Shabele River within the Quaternary flood basalt that gave $^{40}Ar/^{39}Ar$ ages that range between 1.88 and 0.83 Ma (Woldegabriel et al., 1990; Alemu and Abebe, 2007) and using the technique of Schoenbohm et al. (2004), Crosby and Whipple (2006), and Berlin and Anderson (2007), we calculate the parameters K and m in Eq. (9) in the range from 1×10^{-7} to 1×10^{-3} $(m^{0.08}\ y)^{-1}$ and from 0.1 to 0.7.
- We calculated the end-member ages and their uncertainty for each group of knickpoints found within the longitudinal profile of the Shabele River using Eq. (9). Such ages can be suggestive of the time of change in regional tectonic uplift rate or climates. Besides the possibility that the value of *n* might depart from 1 in our development of the knickpoint celerity model for the SEEP, additional sources of uncertainty might be because of the limited ^{40}Ar-^{39}Ar age data that is available to us.

3.5. Results

3.5.1. Geomorphic proxies

3.5.1.1. Normalized steepness index (k_{sn})

In the SEEP, we found k_{sn} ranging between 8.9 and 310 (Fig. 5B). We found the highest k_{sn} values to be associated with the high elevation segments of the SEEP, such as Bale mountains, the North slopes, and the Genale slopes (Fig. 5B). We also found high k_{sn} values in relatively low elevation regions such as the northwest-facing slopes of the MER escarpment and within the rift itself to the northwest of the Bale mountains (basins 14, 29, and 30 in Fig. 5B). We suggest that this is likely caused by the propagation of the border faults of MER. Additionally, we found the southeastern escarpment of the Afar depression to be characterized by low k_{sn} values (Fig. 5B). Along the rift shoulder, k_{sn} values show an increase from northeast of the Ahmar mountains to

southwest of the Bale mountains (Fig. 5A). In addition, we found that the k_{sn} values decrease toward the southeast from the elevated region of the SEEP toward the low region of the plateau, reaching their lowest values within the Weyb basins and the lower Shabele valley (Fig. 5B).

3.5.1.2. Hypsometric integral (HI)

In the SEEP, we found the *HI* values ranging between 0.17 and 0.72. The pattern of *HI* values of individual drainage basins does not follow the pattern of the k_{sn} values, which decreases from northwest to southeast (compare Fig. 5B with Fig. 6). Rather, the *HI* values display distinctive clusters in which most of the drainage basins in the Genale slopes are characterized by the highest *HI* values (Fig. 6). Similarly, we found the drainage basins in the southeastern part of the Weyb basins and the eastern side of the lower Shabele valley to be characterized by high *HI* values (Fig. 6). Also, we found the drainage basins in the southwestern part of the Ahmar mountains and the northern part of the North slopes to be characterized by high *HI* values (Fig. 6). These drainage basins with unexpected high *HI* are affected by the activities of the Genale, Weyb, and Marda fault zones (compare Fig. 6 with Fig. 2).

3.5.1.3 Chi (χ) analysis

In the SEEP, we found χ values ranging between 0 and 48 (Fig. 7). We observed higher χ values along the entire southeastern escarpment of the MER and the Afar Depression dominated by the Bale and Ahmar mountains (Fig. 7). This greatly differs from the floor of the MER, Weyb basin, lower Shabele valley, and the southeastern part of the Genale slopes, which are characterized by low χ (Fig. 7). The presence of low χ values within the floor of the MER and high χ values at its southeastern escarpment indicates that the drainage divide lines between the basins of these two regions are migrating southeastward. We also noticed that the drainage basins in the northeastern part of the Bale mountains (basins 50 and 51 in Fig. 7) have higher χ values

compared to those in the southwestern part of the Bale mountains and the northern part of the Genale slopes (basins 67, 68, 70, 71, 72, 74, and 83 in Fig. 7), showing the drainage divide between the Jubba and Shabele rivers (shown with a blue line in Fig. 7) is migrating northeastward. Such low χ contrast across divides suggests that drainage networks are near equilibrium (e.g., the drainage basins in the Weyb basins, lower Shabele valley, and the southern part of the Genale slopes).

We observed from the χ-elevation relationship (Fig. 8) a sharp difference between the Jubba and Shabele rivers. The χ-elevation lines of the tributaries of the Shabele River are straight, have one consistent slope, and for the most part are concentrated below the line of equilibrium (Fig. 8). In contrast, the χ-elevation lines for the Jubba River are irregular, different segments of them have different slopes, and are concentrated above the line of equilibrium (Fig. 8). These differences suggest a transient nature of the rivers, where the Jubba drainage basin is capturing the Shabele drainage basin northeastward. Also, it suggests that the Shabele River is more adjusted to base level than the Jubba River.

3.5.2. Oligocene flood basalt

The Oligocene flood basalt thickness map of the SEEP shows a general decrease southeastward toward the Weyb basins and the lower Shabele valley (Fig. 9A). Also, we found the thickest Oligocene flood basalt (~1400 m) in the most regions of the Bale mountains and, to a

lesser extent, the Ahmar mountains (Fig. 9A).

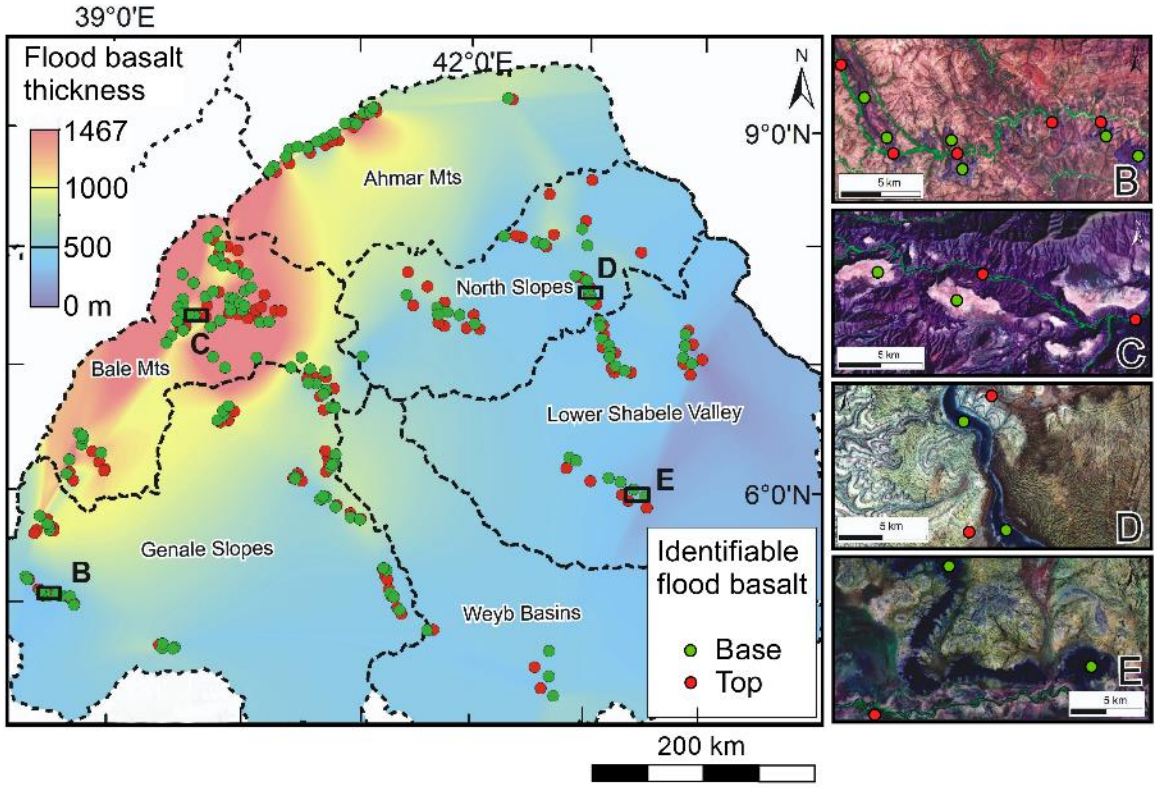

Figure 3- 9 (A) Map of thickness of the Oligocene flood basalt in the southeastern Ethiopian Plateau (SEEP) produced by nearest-neighbor interpolation of the discrete locations of the lower (green dot) and upper (red dot) contacts of the basalt. (B-E) 12-8-3 (Red-Green-Blue) Sentinel 2A images showing examples of identifying the flood basalt contacts within incised valleys (B and C) and inverted valleys (D and E). See Fig. 9 for location.

3.5.3. Knickpoint celerity model

In the SEEP, we found four groups of regionally distributed knickpoints preserved at ~2200, ~2000, ~1750, and ~1050 m elevation (Figs. 11A and B). Also, we found one group of local knickpoints preserved at ~2550 m elevation (Figs. 11A and B). These knickpoints are selected away from lithological contact and faults; hence, they are most likely formed by a persistent change in tectonic uplift rate or change in precipitation (Fig. 10A; Kirby and Whipple, 2012). We found 45 knickpoints within upstream drainage basins of the Shabele and Jubba rivers. These drainage basins have areas ranging between 0.9 and 980 km^2. The existence of knickpoints in the basins of such varying dimensions indicates that they are actively migrating from

downstream to upstream as a transient response to base-level change. The four major clusters of knickpoints at ~2200, ~2000, ~ 1750, and ~1050 m elevations spread regionally in the Bale and the Ahmar mountains and the northwestern part of the North slopes (Figs. 1B and 4). These knickpoints are selected as nonlithologic knickpoints (Figs. 2 and 10), hence their development could have been related to change in regional tectonic uplift rate; while the knickpoints at 2550 m are localized mostly at the Bale mountains (Fig. 4) and have ~50 m higher elevation than these of the Ahmar mountains (Fig. 11).

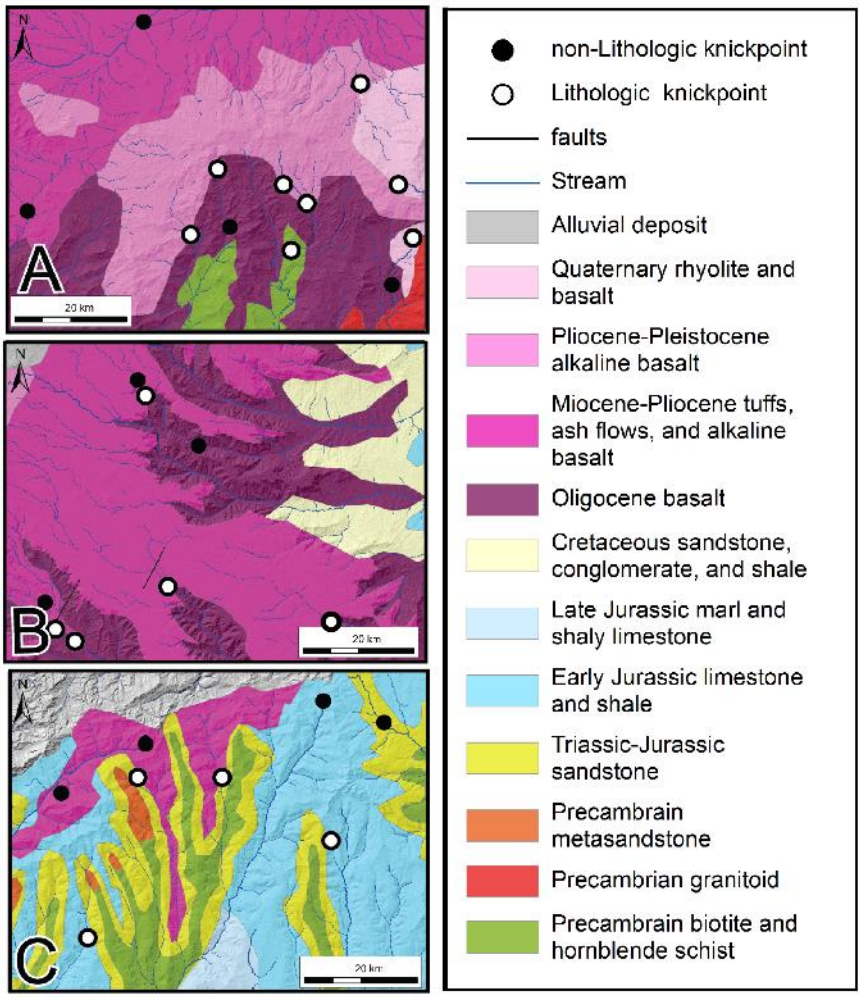

Figure 3- 10 Geologic maps of portions of the Bale (A and B) and Ahmar mountains (C) produced from the modification of the Geological Map of Ethiopia (Kazmin, 1973; Tefera et al., 1996) with observations from the Sentinel-2A images showing examples of differentiating between lithologic and nonlithologic knickpoints. See Fig. 2 for locations for the Bale and Ahmar mountains, constructed from geologic maps and Sentinel-2A satellite data. The geologic map is used to differentiate lithologic knickpoints (white dots) from the nonlithologic knickpoints (black dots). Here, we provide three examples showing the difference

between lithologic knickpoints and nonlithologic knickpoints in the Genale slopes (B), Bale mountains (C), and Ahmar mountains (D).

The drainage basins where Quaternary flood basalt with known ages are exposed were selected in order to establish the knickpoint celerity model and to obtain the parameters m and *K* in Eq. (9). Here, we use basin 36 (Figs. 4 and 12) as an example to show how the model is constructed. This drainage basin was chosen because its streams are incising within Quaternary flood basalt where $^{40}Ar/^{39}Ar$ geochronological data are available to constrain their age between 1.88 and 0.83 Ma (Woldegabriel et al., 1990; Alemu and Abebe, 2007). Figure 12 is a 12-8-3 red-green-blue (RGB) Sentinel-2 image. The green color illustrates the geographical extent of the Quaternary flood basalts and the pink color represents the Mesozoic sedimentary rocks. Two knickpoints are found at ~1723 and ~2034 m elevation along a stream that is incising into the Quaternary flood basalt. These knickpoints belong to the groups of regionally distributed knickpoints at average elevations of ~1750 and ~2000 m, respectively. We used this knickpoint at the ~1723 m elevation with the assumption that this knickpoint was formed by the regression from the nose of the Quaternary flood basalt. Thus, we used the age of 1.88 Ma of the Quaternary flood basalt (Woldegabriel et al., 1990) as the beginning time of the migration of the knickpoint. We therefore measured the migration distance of the knickpoint and hence calculated the celerity in Eq. (9). We followed methods outlined in previous studies (Crosby and Whipple, 2006; Berlin and Anderson, 2007; Sembroni et al., 2016a) to calculate the best fit results of the residuals of the minimum sum of squares for seven modeled knickpoints in basins 48, 51, 68, and 74 (Fig. 4). Subsequently, we established the values for *m* and *K* in Eq. (9) to be 0.221 and $2.49 \times 10^{-4} \pm 1.29$

$\times 10^{-4}$ $(m^{0.08}\ y)^{-1}$ respectively.

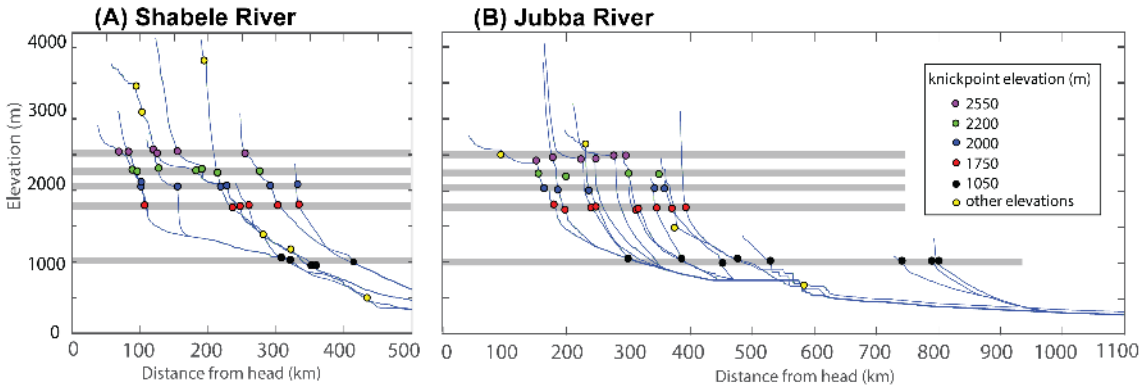

Figure 3- 11 The nonlithologic knickpoints plotted on the longitudinal profiles of the Shabele (A) and the Jubba (B) rivers tributaries, showing most of the knickpoints are preserved at 2550, 2200, 2000, 1750, and 1050 m elevations.

Despite the limited age constraints, this model provides an important insight into the time framework of incision history in the SEEP. We show the age of the formation of these groups of knickpoints on the Shabele River in Table 1. Noticeably, the end-member ages of the group of knickpoints at 2000 and 2200 m elevation have higher accuracy and smaller variation (from 4.56 to 4.75 Ma for the group of knickpoints at 2000 m elevation and from 6.04 to 9.43 Ma for the group of knickpoints at 2200 m elevation) than the group of knickpoints at 2550 m elevation (from 8.83 to 15.02 Ma). This is because the drainage area at the higher elevation is significantly smaller than that at the lower elevation. This results in a larger age difference in the celerity model calculated by Eq. (9).

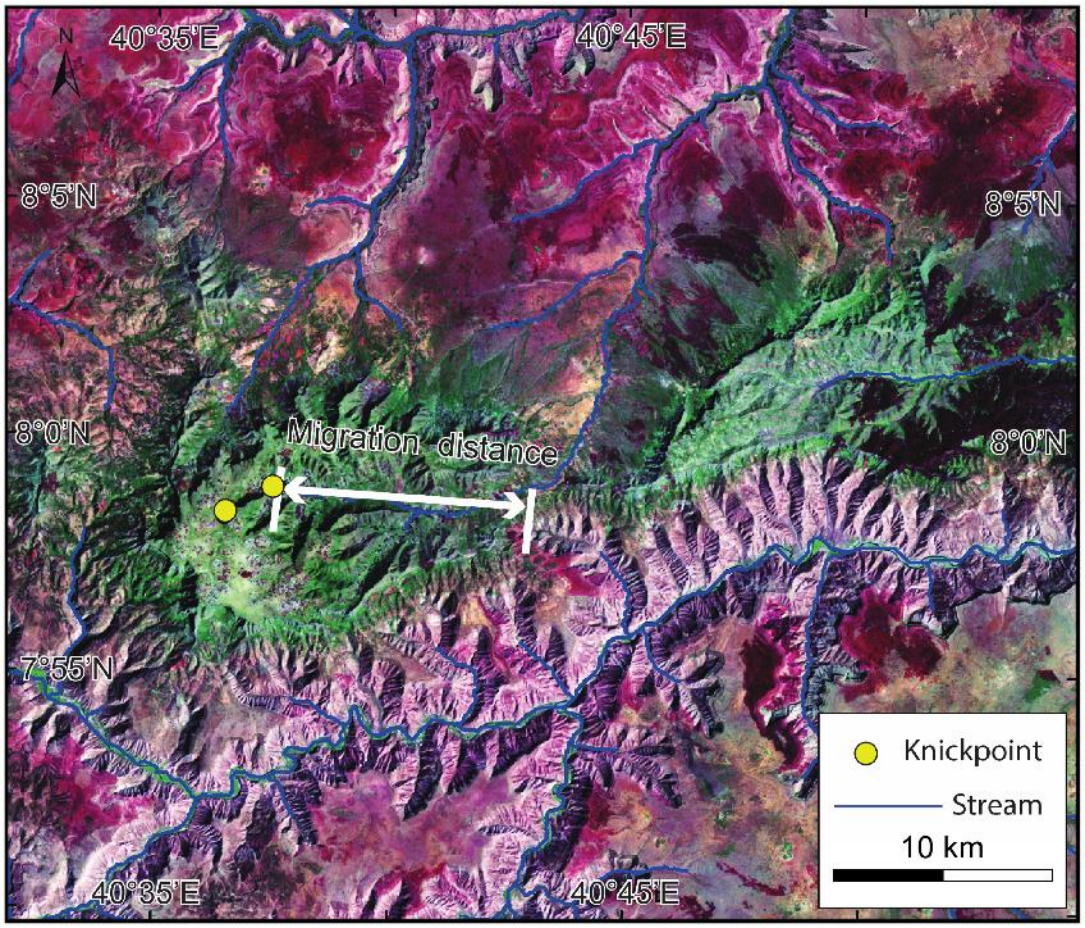

Figure 3- 12 12-8-3 Red-Green-Blue Sentinel-2A image showing the extent of the Quaternary basaltic flow with green color because of the presence of vegetation and the underlying Jurassic limestone pinkish color. See Fig. 4 for location. The knickpoint has regressed upstream from the base of the Quaternary basaltic flow indicating that this knickpoint retreat started no later than 1.88 Ma, which is the oldest 40Ar/39Ar age of the flow (Woldegabriel et al., 1990; Alemu and Abebe, 2007).

Table 2 Knickpoints used for the knickpoint celerity model

Knickpoint group	Basin	Migration Distance(m)	Elevation (m)	Drain area (km^2)	Easting	Northing	Age (Ma)	Age err (Ma)
2000	7	66905	1977	101530611	147459.6	1035153	4.569	1.559
	27	36866	2034	5716989	15496.26	883661	4.754	1.623

	34	70135	2065	114408972	-77315.1	894727	4.665	1.592
2200	48	113954	2141	318283200	-1522.27	806287	6.045	2.063
	12	83070	2201	10136628	184751.5	1049754	9.439	3.221
	50	90717	2222	70247178	-108934	830931	6.720	2.293
	13	63914	2276	20904633	136485.9	1039059	6.189	2.112
	49	98089	2284	99792162	-105679	848136	6.724	2.295
2550	91	170879	2547	357705342	-211324	704083	8.834	3.015
	70	161097	2568	24796683	-197654	701107	15.022	5.127
	18	74837	2494	2170899	107098.7	1033107	11.954	4.080

3.6. Discussion

3.6.1. Geomorphic proxies, spatial distribution of tectonic uplift rates, and drainage basin maturity

Before discussing our geomorphic proxy results within the context of the tectonic uplift rate in the SEEP, we will address the possible influence of precipitation and rock erodibility on these results. Despite the lithological variation and, hence, the heterogeneity in the mechanical strength of the rocks in the SEEP, lithological changes (Figs. 2 and10A-C) do not appear to have exerted a first-order control on the pattern of various geomorphic proxies (Figs. 5-7).

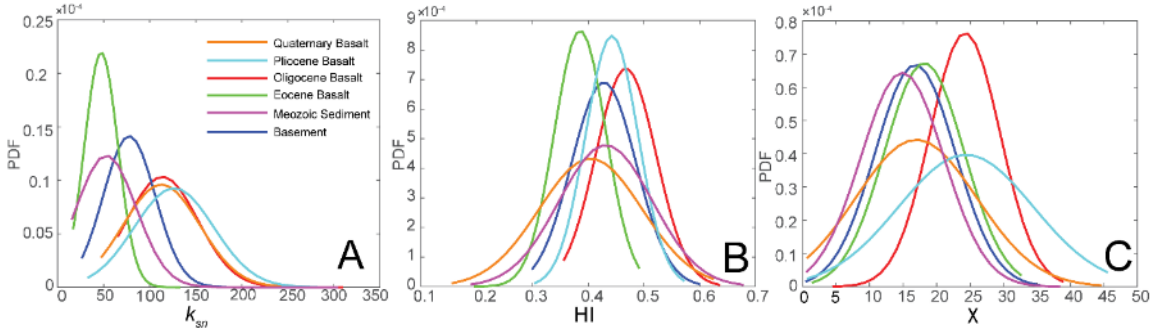

Figure 3- 13 Plot of the probability density function (PDF) of the normalized steepness index (ksn) (A), the hypsometric integral (HI) (B), and the Chi integral (χ) (C) for different lithological units of the southeastern Ethiopian Plateau (SEEP).

Further, to quantify the dependency (or lack of it) of geomorphic proxy patterns on lithological variation, we calculated the absolute frequency of each geomorphic proxy in different lithological units including the Quaternary basalt, the Pliocene basalt, the Oligocene basalt, the Mesozoic sedimentary rocks, and the Precambrian basement rocks (Figs.13A-C). We used the k_{sn}, *HI*, and χ values to construct the probability density function (PDF). Generally, the frequencies of the three geomorphic proxies are consistent within most of the lithological units showing similar PDF pattern (Figs. 13A-C). However, the k_{sn} values show higher PDF for the Eocene flood basalt and that this lithological unit is characterized by a relatively lower k_{sn} value (Fig. 13A). The χ values of the Oligocene basalt and the Pliocene basalt are higher than those of other rock units (Fig. 13C). Therefore, except for the k_{sn} values of the drainage basins within the Eocene basalt, all other geomorphic proxies fail to exhibit positive correlation with the lithology.

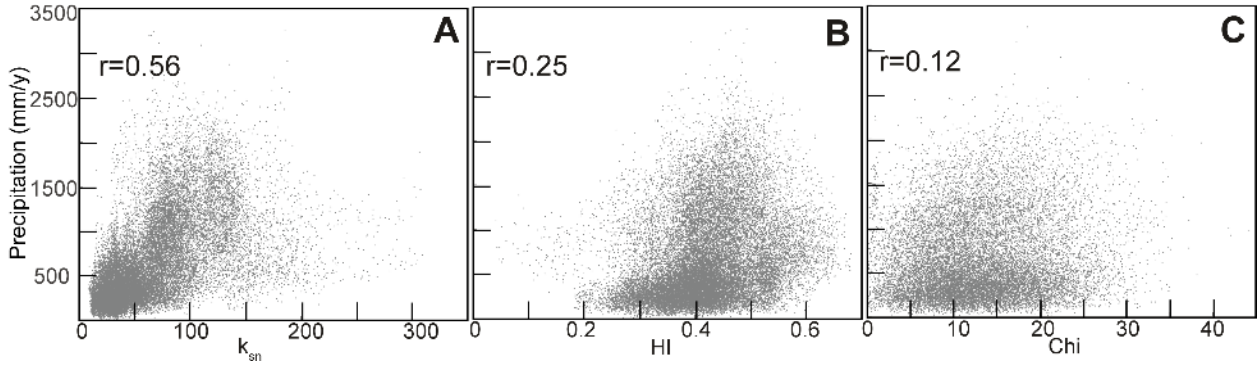

Figure 3- 14 Plots of the precipitation in the southeastern Ethiopian Plateau (SEEP) vs. the values of normalized steepness index (ksn) (A), the hypsometric integral (HI) (B), and the Chi integral (χ) (C). The precipitation data are the average of the last 10 years from the Tropical Rainfall Measuring Mission (TRMM).

Furthermore, we found that modern precipitation has limited effect on the pattern of geomorphic proxies in the SEEP. The only exception is the extreme orographic effect on the precipitation that is confined to the Ahmar and Bale mountains (Fig. 3). The Bale mountains receive high precipitation (>1500 mm/y), and the geomorphic proxies indicate high rates of erosion. However, the geomorphic proxies also indicate high erosion rate and unstable stages of drainage development in the Genale slopes and the North slopes where precipitation is much lower (Fig. 3). Moreover, we found median to low correlation coefficient *r* between the values of different geomorphic proxies and the average precipitation in the last 10 years in the SEEP (Fig. 14). The r values are 0.56 between precipitation and k_{sn} (Fig. 14A), 0.25 between precipitation and *HI* (Fig. 14B), and 0.12 between precipitation and χ (Fig. 14C).

Our results are in agreement with recent cosmogenic studies supporting the dominance of tectonic uplift over climate in the erosion of active mountain ranges (Godard et al., 2014; Fuchs et al., 2015). Accordingly, we believe precipitation plays only a minor role compared to regional tectonic uplift in the development of drainage basins in the SEEP. Hence, we argue that variability in the drainage incision indicated by the geomorphic proxies is more related to the tectonic uplift than climate. With this understanding, we evaluated the regional distribution of tectonic uplift from the southeastern escarpments of the MER to the lowlands of the SEEP in the

southeast and from southwest to northeast along the southeastern escarpment of the MER and the Afar depression.

First, we found that the geomorphic proxies are suggestive of different tectonic uplift rates from the southeastern escarpment of the MER toward the southeastern part of the plateau. We noticed a decrease in the precipitation (Figs. 5A and B), elevation (Figs. 5C and D), and the thickness of the Oligocene flood basalt (Figs. 15E and F) the MER escarpment toward the southeastern part of SEEP. Most of the geomorphic proxies indicate high tectonic uplift rates within the Bale mountains, the eastern side of the North slopes, and the Genale slopes (Figs. 5-7 and 15G-J). This indicates that the tectonic uplift occurred dominantly within the southeastern escarpment of the MER and gradually decreased toward the lower Shabele valley and the Weyb basins possibly because of the flexural uplift of the rift shoulder.

Second, the values of the k_{sn} and *HI* geomorphic proxies suggest that the southeastern escarpment of the northern MER and the Afar depression are experiencing a relatively lower rate of tectonic uplift compared to the southeastern escarpment of the central and southern MER (Figs. 5 and 6). The k_{sn} values extracted from longitudinal profiles of individual streams suggest low incision rate and tectonic uplift rate in the southeastern escarpment of the northern MER compared to that of the central and southern MER (Fig. 5A). Also, the *HI* values of basins 6, 7, 10, 12, and 22 found within the southeastern escarpment of the northern MER are lower than those of basins 91, 95, 101, 108, 111, 113, and 114 on the southeastern escarpment of the central and southern MER (Fig. 6). In addition, results from the χ analysis show that the Shabele River (which originates from the southeastern escarpment of the northern MER) is closer to equilibrium than the Jubba River (which originated from the southeastern escarpment of the central MER at the foot of the Bale mountains) (Figs. 7 and 8).This pattern of tectonic uplift rate is supported by a number of studies inferring that the southeastern escarpment of the northern MER is closer to the steady state than that of the southern MER (Keranen and Klemperer, 2008; Corti, 2009; Agostini et al., 2011; Philippon et al., 2014).

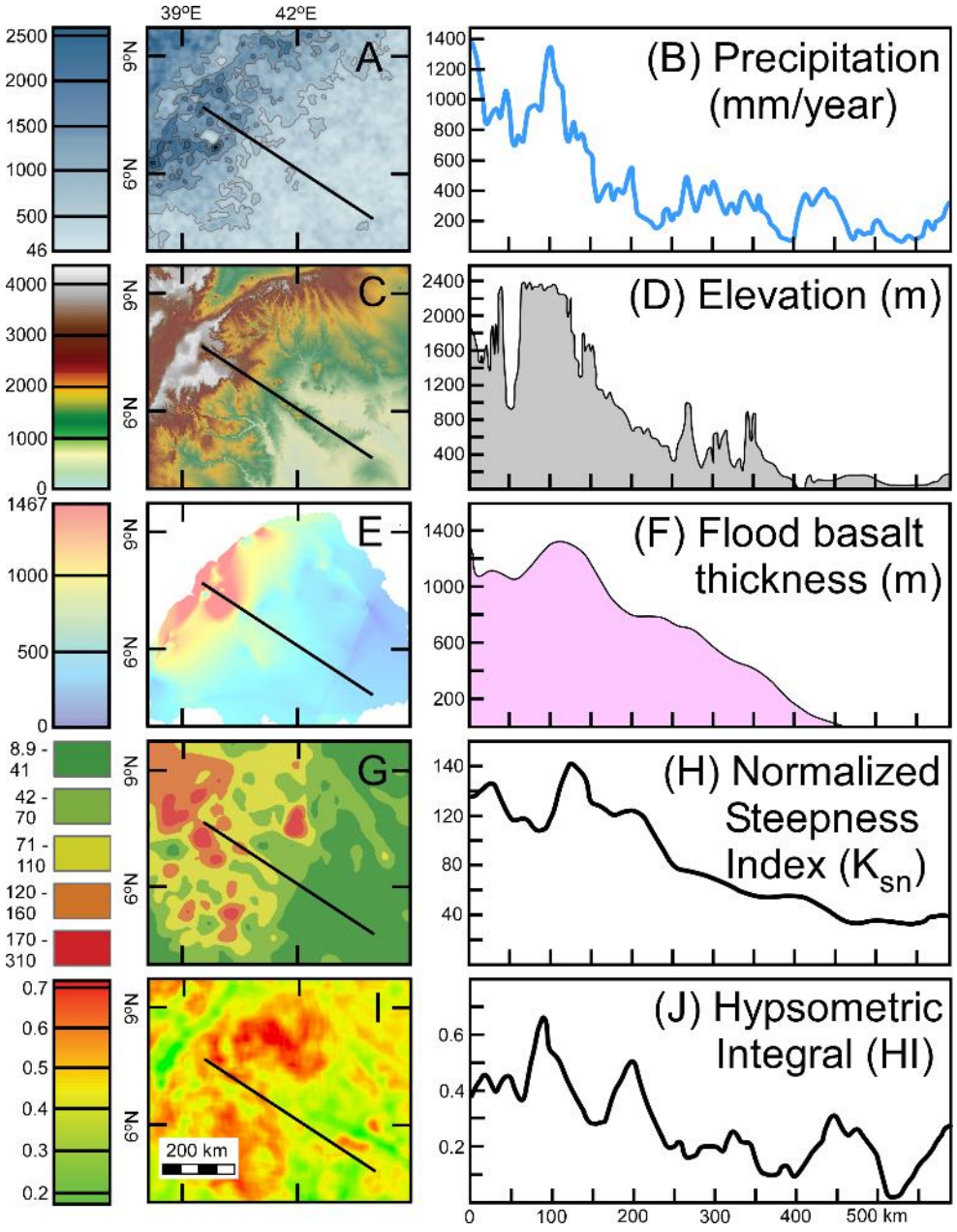

Figure 3- 15 Maps and northwest-southeast profiles of the southeastern Ethiopian Plateau showing variation in precipitation from the average of the last ten years from the Tropical Rainfall Measuring Mission TRMM (A and B), elevation from the Advanced Spaceborne Thermal Emission and Reflection Radiometer (ASTER) digital elevation model (DEM) (C and D), Oligocene flood basalt thickness (E and F), normalized steepness index (ksn) (G and H), and hypsometric integral (HI) (I and J).

Our inferred tectonic uplift pattern provides new insights into the tectonic activities in the different segments of the MER and the Afar depression. The geomorphic proxy analysis shows differential tectonic uplift rates (as inferred by the drainage basin's maturity) within the southeastern escarpment of the northern MER and the Afar Depression and the southeastern

escarpment of the central and the southern MER (Figs. 5-7). This indicates that the northern MER and the Afar depression southeastern border faults are less tectonically active compared to those of the southeastern border fault of the central and southern MER. This might, in turn, suggest that extension in the northern MER and the Afar depression has been transferred from being accommodated by displacement along the border faults to the rift floor. Such change may be related to the transition from mechanical stretching to magma-assisted rifting as suggested by several authors (e.g., Ebinger and Casey, 2001). Geochronological studies suggest that the initiation of extension and tectonic uplift is younger in the central and the southern MER compared to its northern segment. For example, Wolfenden et al. (2004) suggested from an $^{40}Ar/^{39}Ar$ geochronological study that extension in the northern MER started ~11 Ma, while it started ~8 Ma in the central MER. Also, fission-track geochronological studies suggested that tectonic uplift started at 10-12 Ma in the northern MER and ~8 Ma in the southern MER (Balestrieri et al., 2016). Southwestward younging of extension and tectonic uplift is attributed to the southwestward propagation of the MER, likely related to the clockwise rotation of the Somalian Plate (Collet et al., 2000).

The regional distribution of the geomorphic proxy possibly also indicates a reactivation of regional structures. The structural framework of the SEEP is discussed in section 2.3 and shows various faults (dominated by the Marda, Weyb, and Genale fault belts) cross-cutting the plateau (Fig. 2). The Marda fault belt is a Precambrian intercontinental structure that was known to have been reactivated multiple times (Purcell, 1976; Mège et al., 2015). The Marda fault belt might have influenced the Pleistocene volcano-tectonic events in the SEEP (Purcell, 1976). However, our geomorphic proxy analysis in drainage basins near the fault belt such as the Amher Mountains and the eastern part of the North slopes is indicative of tectonic quiescence. We noticed high geomorphic proxy values, especially the *HI*, in the eastern part of the lower Shabele valley (Fig. 6), and this could be related to neotectonic activities in the southeastern part of the Marda fault belt (Fig. 2). We also found high geomorphic proxy values in the drainage basins

within the Genale slopes and the Weyb Basins, where the Genale and the Weyb fault belts are localized. Such high geomorphic proxy values may suggest reactivation of these major fault belts, forming a transient adjustment of hillslope gradient. This is in agreement with observations from apatite fission track data that suggested possible reactivation of old structures in the southern MER during the last 5 Ma (Philippon et al., 2014).

3.6.2. Knickpoint celerity model and implication for episodic tectonic uplift of the Ethiopian Plateau

The knickpoint celerity model of the SEEP presents four groups of regional knickpoints at ~2200, ~2000, ~1750, and ~1050 m elevations and one group of local knickpoints at ~2550 m elevation. Preservation of a group of knickpoints at similar elevations indicates uniform drainage system response in the Jubba and the Shabele rivers and that the region experienced at least three phases of drainage incision triggered by base-level change. The end-member ages of these incision episodes extracted from the knickpoint celerity model are ~4.5, ~6.5, and ~11.7 Ma. These results suggest that after the emplacement of the Oligocene flood basalt, the steady incision of the drainage systems was interrupted episodically, at least four times. We also identified a local knickpoint group at ~2550 m elevation, localized only at the drainage basins of the Bale mountains and the Genale slopes rather than along the whole MER southeastern escarpment. We suggest that a local and older tectonic uplift and/or climatic event might have affected the development of the drainage system of the Jubba River prior to ~11.7 Ma.

Apart from the difference in erodibility of lithological units, two other principal factors that result in the development of a regional group of knickpoints at similar elevation are tectonic uplift and variations of the ratio between discharge to sediment flux induced by increased precipitation (Tucker and Slingerland, 1997; Kirby and Whipple, 2012). Two significant climatic change events have been documented since the formation of the SEEP. The oldest event is related

to the tectonic uplift in the Miocene-Pliocene (8 Ma), leading to the development of high topography in the Ethiopian Plateau and the Lake Plateau to the south (Wall of Africa) (Cerling et al., 1997; Sepulchre et al., 2006). Such a topographic barrier permitted a considerable reorganization of atmospheric circulation and reduced the moist air coming from the Atlantic Ocean across Africa, resulting in a decrease of precipitation and a transition from woodland to grassland in East Africa (Sepulchre et al., 2006). Moreover, analysis of pollen data and fossil mammals suggest another climate shift in the Pliocene (4 Ma to 3 Ma), leading to an expansion of grassland ecosystems in East Africa (Bobe and Behrensmeyer, 2004; Bonnefille et al., 2004). Studies in global scale also indicated a climate oscillation during the Pliocene- Pleistocene, resulting in a shift in African climate, vegetation, and faunal assemblages (DeMenocal, 2004). These two major climate change events greatly impact the Ethiopian Plateau in terms of rainfall pattern and amount. Our knickpoint celerity model end-member age of 6.5 Ma coincides with the formation of the central MER between 10 and 5 Ma (Bonini et al., 2005), and the 4.5 Ma end-member age coincides with regional climate shift and the expansion of grassland during the 4 to 3 Ma period (Table 1). These regionally distributed groups of knickpoints provide evidence of an episodic tectonic uplift pattern associated with at least two tectonic events rather than a steady uplift pattern in the SEEP.

3.6.3 The role of preexisting structure in the distribution pattern of the rate of tectonic uplift

Our geomorphic proxy analysis indicates a higher tectonic uplift rate along the southeastern escarpment of the MER and the Afar Depression than the low land of the SEEP (e.g. lower Shabele valley, Genale slopes, and Weyb basins). The geomorphic proxies also show a high value at the Bale mountains and the Genale slopes, with a general decrease in the geomorphic proxy values southeastward (Figs.15G-J). This southeastward increase in uplift may be related to the flexural uplift along the shoulder of the MER, which can be up to 200 km from

the rift shoulder (Sembroni et al., 2016a). The Ahmar mountains have a relatively lower geomorphic proxy values compared to the Bale mountains adjacent to it. Moreover, the channel morphology of the Shabele River and χ data is additional evidence for the difference in tectonic uplift rates between the Ahmar and the Bale mountains (Fig. 7). Most tributaries of the Jubba and the Shabele rivers flow from the MER escarpment to the southeast because of the elevation gradient (Fig. 1B). The exception is a few tributaries of the Shabele River in basins 51, 50, 39, 37, 36, 32, and 40 that flow northeastward parallel to the strike of the MER. The redirection of these streams was likely caused by uneven tectonic uplift of the sources of these rivers in the Bale and Ahmar mountains. Such uneven tectonic uplift along the shoulder of the MER was also reported by Bonini et al. (2005), who addressed that the deformation with the southern Afar was accommodated while the southern MER was still in the stage of tectonic quiescence between the Miocene and Pliocene. Also, the χ map shows that the drainage basin divide between the Jubba and the Shabele rivers (at the Bale mountains, basins 48, 51 in Fig. 7) are migrating eastward, suggesting higher uplift rates in the Bale mountains than that in the Ahmar mountains. This variation may be explained by the pattern of the thickness distribution of the Oligocene flood basalt, where the thickness of flood basalt in the Bale mountains is larger and more expressed than that of Ahmar mountains (Fig. 9).

3.6.4. Correlation between the tectonic uplift history of the southeastern and northwestern Ethiopian Plateau

The elevations at which the groups of regional knickpoints are located on the SEEP and the northwestern Ethiopian Plateau suggest a possible similar tectonic uplift history of the two plateaus. Previous geomorphological studies conducted in the Blue Nile and the Tekeze River on the northwestern Ethiopian Plateau found groups of regional knickpoints at 1050, 2000, and 2500 m elevations (Ismail and Abdelsalam, 2012; Sembroni et al., 2016b). These are similar to the groups of regional knickpoints we found on the SEEP at 1050 and 2000 m elevations and a group

of local knickpoints at 2550 m elevation. The preservation of groups of knickpoints at the same elevation in the major drainage systems in the SEEP and in the northwestern Ethiopian Plateau (the Jubba River, the Shabele River, the Blue Nile, and the Tekeze River) suggests that they were formed during pulses of tectonic uplift or global climate change that affected the broad region that encompasses both plateaus.

Geomorphic analysis carried out in the Blue Nile River (Gani et al., 2007; Gani and Neupane, 2017)—using field data, GIS-based DEM and published isotopic ages, and river longitudinal profiles and mantle tomography—and in the Tekeze River (Ismail and Abdelsalam, 2012) —using quantitative geomorphology—have shown three phases of incision in the northwestern Ethiopian Plateau at 29–10, 10–6, and 6 Ma to present. More recently, Sembroni et al. (2016b) applied the knickpoint celerity model analysis in the Blue Nile and the Tekeze River and suggested the presence of three base level changes that were superimposed at 20-10 Ma, 10-5 Ma, and Quaternary on the broadly and regionally uplifted northwestern Ethiopian Plateau. The ages of the pulses of tectonic uplift that affected the northwestern Ethiopian Plateau is similar to the ages of tectonic uplift pulses that we found to have affected the SEEP at 11.7, 6.5, and 4.5 Ma.

3.7. Conclusions

By integrating geomorphic proxy analysis (including k_{sn}, *HI*, and χ), a knickpoint celerity model, and the thickness of flood basalt, we estimated the spatial and temporal patterns in the tectonic uplift rate in the SEEP. We found that (i) The spatial distribution of the geomorphic proxy values is suggestive of a more tectonically active southeastern escarpment of the central and southern MER compared to the northern MER. (ii) The distribution of geomorphic proxy values along the Shabele River is closer to a steady-state than the Jubba River. These geomorphic proxies show a higher tectonic uplift rate in the Bale mountains, and in the Genale slopes and

possible reactivation in the areas dominated by the Genale and Weyb faults. (iii) The knickpoint celerity model suggests at least three groups of knickpoints related to regional pulses of tectonic uplift at 11.7 Ma, 6.5 Ma, and 4.5 Ma. (iv) We infer that the SEEP has a pulsed tectonic uplift history similar to that of the northwestern Ethiopian Plateau, indicative of common broad regional tectonic events.

3.8. Reference

Agostini, A., M. Bonini, Corti, G., Sani, F., Manetti, P., 2011. Distribution of Quaternary deformation in the central main Ethiopian rift, East Africa. Tectonics, 30(4), TC4010.

Alemu, T., Abebe, T., 2007, Geology and tectonic evolution of the Pan-African Tulu Dimtu Belt, Western Ethiopia. Online Journal of Earth Sciences, 1(1), 24-42.

Balestrieri, M.L., Bonini, M., Corti, G., Sani, F., Philippon, M., 2016. A refinement of the chronology of rift-related faulting in the Broadly Rifted Zone, southern Ethiopia, through apatite fission-track analysis. Tectonophysics, 671, 42-55.

Beeson, H.W., McCoy, S.W., Keen-Zebert, A., 2017. Geometric disequilibrium of river basins produces long-lived transient landscapes. Earth and Planetary Science Letters, 475, 34-43.

Beltrando, G., Camberlin, P., 1993. Interannual variability of rainfall in the Eastern Horn of Africa and indicators of atmospheric circulation. International Journal of Climatology, 13(5), 533-546.

Berlin, M.M., Anderson, R.S., 2007. Modeling of knickpoint retreat on the Roan Plateau, western Colorado. Journal of Geophysical Research: Earth Surface, 112(F3).

Bobe, R., Behrensmeyer, A.K., 2004. The expansion of grassland ecosystems in Africa in relation to mammalian evolution and the origin of the genus Homo. Palaeogeography, Palaeoclimatology, Palaeoecology, 207(3), 399-420.

Boccaletti, M., Getaneh, A., Bonavia, F., 1991. The Marda Fault: A remnant of an incipipient aborted rfit in the Paleo-African Arabian Plate. Journal of Petroleum Geology, 14(1), 79-91.

Boccaletti, M., Bonini, M., Mazzuoli, R., Abebe, B., Piccardi, L., Tortorici, L., 1998. Quaternary oblique extensional tectonics in the Ethiopian Rift (Horn of Africa). Tectonophysics, 287(1), 97-116.

Bonini, M., Corti, G., Innocenti, F., Manetti, P., Mazzarini, F., Abebe, T., Pecskay, Z., 2005. Evolution of the Main Ethiopian Rift in the frame of Afar and Kenya rifts propagation. Tectonics, 24(1).

Bonnefille, R., Potts, R., Chalié, F., Jolly, D., Peyron, O., 2004. High-resolution vegetation and climate change associated with Pliocene Australopithecus afarensis. Proceedings of the National Academy of Sciences, 101(33), 12125-12129.

Cerling, T.E., Harris, J.M., MacFadden, B.J., Leakey, M.G., Quade, J., Eisenmann, V., Ehleringer, J.R., 1997. Global vegetation change through the Miocene/Pliocene boundary. Nature, 389(6647), 153-158.

Chen, Y.C., Sung, Q.C., Cheng, K.Y., 2003. Along-strike variations of morphotectonic features in the Western Foothills of Taiwan: tectonic implications based on stream-gradient and hypsometric analysis. Geomorphology, 56(1-2), 109-137.

Collet, B., Taud, H., Parrot, J., Bonavia, F., Chorowicz, J., 2000. A new kinematic approach for the Danakil block using a Digital Elevation Model representation. Tectonophysics, 316(3), 343-357.

Corti, G., 2009. Continental rift evolution: from rift initiation to incipient break-up in the Main Ethiopian Rift, East Africa. Earth-Science Reviews, 96(1), 1-53.

Crosby, B.T., Whipple, K.X., 2006. Knickpoint initiation and distribution within fluvial networks: 236 waterfalls in the Waipaoa River, North Island, New Zealand. Geomorphology, 82(1), 16-38.

Cyr, A.J., Granger, D.E., Olivetti, V., Molin, P., 2010. Quantifying rock uplift rates using channel steepness and cosmogenic nuclide–determined erosion rates: Examples from northern and southern Italy. Lithosphere, 2(3), 188-198.

DeMenocal, P. B., 2004. African climate change and faunal evolution during the Pliocene–Pleistocene. Earth Planet Science Letters, 220(1-2), 3-24.

Drusch, M., Del Bello, U., Carlier, S., Colin, O., Fernandez, V., Gascon, F., Hoersch, B., Isola, C., Laberinti, P., Martimort, P., 2012. Sentinel-2: ESA's optical high-resolution mission for GMES operational services. Remote Sensing of Environment, 120, 25-36.

Dugda, M.T., Nyblade, A.A., Julia, J., 2007. Thin lithosphere beneath the Ethiopian Plateau revealed by a joint inversion of Rayleigh wave group velocities and receiver functions. Journal of Geophysical Research: Solid Earth, 112(B8).

Ebinger, C., Casey, M., 2001. Continental breakup in magmatic provinces: An Ethiopian example. Geology, 29(6), 527-530.

Faccenna, C., Becker, T.W., Jolivet, L., Keskin, M., 2013. Mantle convection in the Middle East: Reconciling Afar upwelling, Arabia indentation and Aegean trench rollback. Earth Planet Science Letters, 375, 254-269.

Fazzini, M., Bisci, C., Billi, P., 2015. The climate of Ethiopia, Landscapes and Landforms of Ethiopia. Springer, 65-87.

Flint, J.J., 1974. Stream gradient as a function of order, magnitude, and discharge. Water Resources Research, 10(5), 969-973.

Fuchs, M., Gloaguen, R., Merchel, S., Pohl, E., Sulaymonova, V., Andermann, C., Rugel, G., 2015. Denudation rates across the Pamir based on 10 Be concentrations in fluvial sediments: dominance of topographic over climatic factors. Earth Surface Dynamics, 3(3), 423.

Furman, T., Nelson, W.R., Elkins-Tanton, L.T., 2016. Evolution of the East African rift: Drip magmatism, lithospheric thinning and mafic volcanism. Geochimica et Cosmochimica Acta, 185, 418-434.

Gani, N. D., Neupane, P. C., 2017. Understanding transient landscape of the Ethiopian Plateau in relation to mantle dynamics. Geological Journal, 53(1).,371-385.

Gani, N.D., Abdelsalam, M.G., Gera, S., Gani, M.R., 2009. Stratigraphic and structural evolution of the Blue Nile Basin, Northwestern Ethiopian Plateau. Geological Journal, 44(1), 30-56.

Gani, N.D., Gani, M.R., Abdelsalam, M.G., 2007. Blue Nile incision on the Ethiopian Plateau: pulsed plateau growth, Pliocene uplift, and hominin evolution. GSA today, 17(9), 4.

Gao, M., Zeilinger, G., Xu, X., Tan, X., Wang, Q., Hao, M., 2016. Active tectonics evaluation from geomorphic indices for the central and the southern Longmenshan range on the Eastern Tibetan Plateau, China. Tectonics, 35(8), 1812-1826.

Godard, V., Bourlès, D.L., Spinabella, F., Burbank, D.W., Bookhagen, B., Fisher, G.B., Moulin, A., Léanni, L., 2014. Dominance of tectonics over climate in Himalayan denudation. Geology, 42(3), 243-246.

Hack, J.T., 1973. Stream-profile analysis and stream-gradient index. Journal of Research of the US Geological Survey, 1(4), 421-429.

Harkins, N., Kirby, E., Heimsath, A., Robinson, R., Reiser, U., 2007. Transient fluvial incision in the headwaters of the Yellow River, northeastern Tibet, China. Journal of Geophysical Research: Earth Surface, 112(F3).

Hayward, N., Ebinger, C., 1996. Variations in the along-axis segmentation of the Afar Rift system. Tectonics, 15(2), 244-257.

Hofmann, C., Courtillot, V., Feraud, G., Rochette, P., Yirgu, G., Ketefo, E., Pik, R., 1997. Timing of the Ethiopian flood basalt event and implications for plume birth and global change. Nature, 389(6653), 838-841.

Howard, A.D., Dietrich, W.E., Seidl, M.A., 1994. Modeling Fluvial Erosion on Regional to Continental Scales. J Geophys Res-Sol Ea, 99(B7), 13971-13986.

Ismail, E.H., Abdelsalam, M.G., 2012. Morpho-tectonic analysis of the Tekeze River and the Blue Nile drainage systems on the Northwestern Plateau, Ethiopia. Journal of African Earth Sciences, 69, 34-47.

Kazmin, V., 1973, Geological map of Ethiopia, Geological Survey of Ethiopia.

Keir, D., Bastow, I.D., Pagli, C., Chambers, E.L., 2013. The development of extension and magmatism in the Red Sea rift of Afar. Tectonophysics, 607, 98-114.

Keranen, K., Klemperer, S., 2008. Discontinuous and diachronous evolution of the Main Ethiopian Rift: Implications for development of continental rifts. Earth Planet Sc Lett, 265(1), 96-111.

Kieffer, B., Arndt, N., Lapierre, H., Bastien, F., Bosch, D., Pecher, A., Yirgu, G., Ayalew, D., Weis, D., Jerram, D.A., 2004. Flood and shield basalts from Ethiopia: magmas from the African superswell. Journal of Petrology, 45(4), 793-834.

Kirby, E., Whipple, K.X., 2012. Expression of active tectonics in erosional landscapes. Journal of Structural Geology, 44, 54-75.

Kirby, E., Whipple, K.X., Tang, W.Q., Chen, Z.L., 2003. Distribution of active rock uplift along the eastern margin of the Tibetan Plateau: Inferences from bedrock channel longitudinal profiles. Journal of Geophysical Research: Solid Earth, 108(B4).

Kogan, L., Fisseha, S., Bendick, R., Reilinger, R., McClusky, S., King, R., Solomon, T., 2012. Lithospheric strength and strain localization in continental extension from observations of the East African Rift. Journal of Geophysical Research: Solid Earth, 117(B3).

Lifton, N.A., Chase, C.G., 1992. Tectonic, climatic and lithologic influences on landscape fractal dimension and hypsometry: implications for landscape evolution in the San-Gabriel Mountains, California. Geomorphology, 5(1-2), 77-114.

Mackenzie, G., Thybo, H., Maguire, P., 2005. Crustal velocity structure across the Main Ethiopian Rift: results from two-dimensional wide-angle seismic modelling. Geophys J Int, 162(3), 994-1006.

Mège, D., Purcell, P., Pochat, S., Guidat, T., 2015. The landscape and landforms of the Ogaden, Southeast Ethiopia, Landscapes and Landforms of Ethiopia. Springer, pp. 323-348.

Mengesha, T., Tadios, C., Workneh, H., 1996, Explanation of the geological map of Ethiopia, Ethiopian Geological Survey, Addis Ababa, Ethiopia.

Miller, S.R., Baldwin, S.L., Fitzgerald, P.G., 2012. Transient fluvial incision and active surface uplift in the Woodlark Rift of eastern Papua New Guinea. Lithosphere, 4(2), 131-149.

Mudd, S. M., Attal, M., Milodowski, D. T., Grieve, S. W. D., Valters, D. A., 2014. A statistical framework to quantify spatial variation in channel gradients using the integral method of channel profile analysis. Journal of Geophysical Research. Earth Surface, 119(2), 138-152.

Nelson, W., Furman, T., Hanan, B., 2008. Sr, Nd, Pb and Hf evidence for two-plume mixing beneath the East African Rift System. Geochimica et Cosmochimica Acta, 72, A676.

Niemann, J.D., Gasparini, N.M., Tucker, G.E., Bras, R.L., 2001. A quantitative evaluation of Playfair's law and its use in testing long-term stream erosion models. Earth Surface Processes and Landforms, 26(12), 1317-1332.

Ohmori, H., 1993. Changes in the hypsometric curve through mountain building resulting from concurrent tectonics and denudation. Geomorphology, 8(4), 263-277.

Peel, M.C., Finlayson, B.L., McMahon, T.A., 2007. Updated world map of the Köppen-Geiger climate classification. Hydrology and earth system sciences discussions, 4(2), 439-473.

Perez-Pena, J.V., Azanon, J.M., Azor, A., 2009. CalHypso: An ArcGIS extension to calculate hypsometric curves and their statistical moments: Applications to drainage basin analysis in SE Spain. Computers & Geosciences -Uk, 35(6), 1214-1223.

Perron, J.T., Royden, L., 2013. An integral approach to bedrock river profile analysis. Earth Surf Proc Land, 38(6), 570-576.

Philippon, M., Corti, G., Sani, F., Bonini, M., Balestrieri, M.L., Molin, P., Willingshofer, E., Sokoutis, D., Cloetingh, S., 2014. Evolution, distribution, and characteristics of rifting in southern Ethiopia. Tectonics, 33(4), 485-508.

Pik, R., B. Marty, Carignan, J., Lavé, J., 2003. Stability of the Upper Nile drainage network (Ethiopia) deduced from (U–Th)/He thermochronometry: implications for uplift and erosion of the Afar plume dome. Earth Planet Science Letters, 215(1), 73-88.

Pik, R., Marty, B., Carignan, J., Yirgu, G., Ayalew, T., 2008. Timing of East African Rift development in southern Ethiopia: Implication for mantle plume activity and evolution of topography. Geology, 36(2), 167-170.

Prave, A., Bates, C., Donaldson, C., Toland, H., Condon, D., Mark, D., Raub, T., 2016. Geology and geochronology of the Tana Basin, Ethiopia: LIP volcanism, super eruptions and Eocene–Oligocene environmental change. Earth Planet Science Letters, 443, 1-8.

Purcell, P., 1976. The Marda fault zone, Ethiopia.Nature, 261(5561), 569-571.

Rooney, T.O., Hart, W.K., Hall, C.M., Ayalew, D., Ghiorso, M.S., Hidalgo, P., Yirgu, G., 2012. Peralkaline magma evolution and the tephra record in the Ethiopian Rift. Contributions to Mineralogy and Petrology, 164(3), 407-426.

Schmidt, J.L., Zeitler, P.K., Pazzaglia, F.J., Tremblay, M.M., Shuster, D.L., Fox, M., 2015. Knickpoint evolution on the Yarlung river: Evidence for late Cenozoic uplift of the southeastern Tibetan plateau margin. Earth Planet Science Letters, 430, 448-457.

Schoenbohm, L., Whipple, K., Burchfiel, B., Chen, L., 2004. Geomorphic constraints on surface uplift, exhumation, and plateau growth in the Red River region, Yunnan Province, China. GSA Bulletin, 116(7-8), 895-909.

Sembroni, A., Faccenna, C., Becker, T.W., Molin, P., Bekele, A., 2016a. Long-term, deep-mantle support of the Ethiopia-Yemen Plateau. Tectonics.

Sembroni, A., Molin, P., Pazzaglia, F.J., Faccenna, C., Abebe, B., 2016b. Evolution of continental-scale drainage in response to mantle dynamics and surface processes: an example from the Ethiopian Highlands. Geomorphology, 261, 12-29.

Sengor, A.C., 2001. Elevation as indicator of mantle-plume activity. Mantle plumes: their identification through time, 352, 183.

Sepulchre, P., Ramstein, G., Fluteau, F., Schuster, M., Tiercelin, J.-J., Brunet, M., 2006. Tectonic uplift and Eastern Africa aridification. Science, 313(5792), 1419-1423.

Simmons, N.A., Forte, A.M., Grand, S.P., 2007. Thermochemical structure and dynamics of the African superplume. Geophysics Research Letter, 34(2).

Snyder, N.P., Whipple, K.X., Tucker, G.E., Merritts, D.J., 2000. Landscape response to tectonic forcing; digital elevation model analysis of stream profiles in the Mendocino triple junction region, Northern California. GSA Bulletin, 112(8), 1250-1263.

Stern, R.J., 1994. Arc assembly and continental collision in the Neoproterozoic East African Orogen: implications for the consolidation of Gondwanaland. Annual Review of Earth and Planetary Sciences, 22(1), 319-351.

Strahler, A.N., 1952. Hypsometric (Area-Altitude) Analysis of Erosional Topography. GSA Bulletin, 63(11), 1117.

Tefera, M., Cherenet, T., Haro, W., 1996. Geological map of Ethiopia (1: 2, 000, 000), Ethiopian Institute of Geological Survey, Addis Ababa, Ethiopia.

Tucker, G.E., Slingerland, R., 1997. Drainage basin responses to climate change. Water Resources Research, 33(8), 2031-2047.

Ukstins, I.A., Renne, P.R., Wolfenden, E., Baker, J., Ayalew, D., Menzies, M., 2002. Matching conjugate volcanic rifted margins: 40 Ar/39 Ar chrono-stratigraphy of pre-and syn-rift bimodal flood volcanism in Ethiopia and Yemen. Earth and Planetary Sciences, 198(3), 289-306.

Whipple, K.X., Forte, A.M., DiBiase, R.A., Gasparini, N.M., Ouimet, W.B., 2017. Timescales of landscape response to divide migration and drainage capture: Implications for the role of divide mobility in landscape evolution. Journal of Geophysical Research: Earth Surface, 122(1), 248-273.

Whipple, K.X., 2004. Bedrock rivers and the geomorphology of active orogens. Annual Review of Earth and Planetary Sciences 32, 151-185.

Whipple, K.X., Hancock, G.S., Anderson, R.S., 2000. River incision into bedrock: Mechanics and relative efficacy of plucking, abrasion, and cavitation. GSA Bulletin, 112(3), 490-503.

Whipple, K.X., Tucker, G.E., 1999. Dynamics of the stream-power river incision model: Implications for height limits of mountain ranges, landscape response timescales, and research needs. Journal of Geophysical Research-Solid Earth, 104(B8), 17661-17674.

Willett, S.D., McCoy, S.W., Perron, J.T., Goren, L., Chen, C.Y., 2014. Dynamic reorganization of river basins. Science, 343(6175), 1248765.

Wobus, C., Whipple, K.X., Kirby, E., Snyder, N., Johnson, J., Spyropolou, K., Crosby, B., Sheehan, D., 2006. Tectonics from topography: procedures, promise, and pitfalls. Geological Society of America Special Papers, 398, 55-74.

Woldegabriel, G., Aronson, J.L., Walter, R.C., 1990. Geology, geochronology, and rift basin development in the central sector of the Main Ethiopia Rift. GSA Bulletin, 102(4), 439-458.

Wolfenden, E., Ebinger, C., Yirgu, G., Deino, A., Ayalew, D., 2004. Evolution of the northern Main Ethiopian rift: birth of a triple junction. Earth Planet Science Letters, 224(1), 213-228.

Worku, T., Astin, T.R., 1992. The Karoo sediments (Late Palaeozoic to Early Jurassic) of the Ogaden Basin, Ethiopia. Sedimentary Geology, 76(1-2), 7-21.

CHAPTER IV

DRAINAGE INCISION, TECTONIC UPLIFT, AND MAGMATISM OF THE KENYA RIFT, EAST AFRICAN RIFT SYSTEM: A MORPHO-TECTONIC ANALYSIS APPROACH

4.0. Abstract

This work examines the tectonic uplift history of the Kenya Rift (divided into a northern, a central, and a southern segment; henceforth NKR, CKR, and SKR) within the East African Rift System (EARS) by: (1) estimating the long-term (since Miocene - ~15 Ma) drainage incision pattern within the Kenya Rift by first obtaining the difference between modern topography and paleo-datum and then dividing the resulting regional incision by published ages of volcanic rocks; (2) characterizing the short-term (since Pliocene - ~4.5 Ma) drainage incision pattern and drainage basin divide migration using the chi integral geomorphic proxy; and (3) correlating the spatial and temporal drainage incision pattern with known magmatic, tectonic, and climatic events in the Kenya Rift. The long-term incision analysis shows that the incision rate is higher in the CKR averaging ~300 mm/ky since 4.5 Ma. Such Pliocene increase is also observed in other parts of the EARS. The short term incision analysis shows that the NKR is approaching steady state, while the CKR and SKR are still in transit state with active drainage basin divides migration. This work found that the spatial and temporal pattern of the tectonic uplift inferred from the drainage incision is well-correlated with known phases of magmatic activities.

Also, this work found that the rapid increase in drainage incision since ~4.5 Ma correlated well with major change in vegetation from grassland to woodland. This suggests that the tectonic uplift coupled with Pliocene magmatic activities have caused a major shift in the ecosystem in the region.

4.1. Introduction

The incision of bedrock drainage systems (henceforth drainage incision) due to tectonic uplift is one of the main processes that shape the Earth landscape in unglaciated and tectonically-active regions [e.g., *Howard et al.*, 1994]. Under similar erodibility conditions of bedrock, the variation in the rate of drainage incision can be used to constrain the change in tectonic uplift and/or erosion rate that accompanies variation of precipitation driven by climate change [e.g., *Kirby and Whipple*, 2012; *Montgomery and Brandon*, 2002; *Whipple*, 2004]. Therefore, to achieve a comprehensive understanding of landscape evolution, constraints on the spatial and temporal patterns of drainage incision over multiple time intervals are desired. On the one hand, the short term (10^3-10^6 yr) drainage incision rate can be estimated using models based on stream-power equations integrated with knowledge on the formation of knickpoints observed in the stream's longitudinal profiles and their headward migration [*Hilley and Arrowsmith*, 2008; *Kirby et al.*, 2003; *Willett et al.*, 2014; *Wobus et al.*, 2006]. On the other hand, the long-term (10^6-10^7 yr) drainage incision rate can be estimated from computing the difference between modern topography and paleo-datum then dividing the resulting regional incision by known ages of marker horizons such as the base of volcanic remnants or stream's terraces [*Grimaud et al.*, 2014; *Lavé and Avouac*, 2001]. Documenting drainage incision history using this approach has been proven to be effective in non-orogenic settings where the tectonic uplift rate is not rapid enough in the time scale of 10^6-10^7 yr to be detected by thermochronological studies [*Beauvais and Chardon*, 2013; *Grimaud et al.*, 2014].

The East African Rift System (EARS) consists of three segments, including the Northern Branch (the Afar Depression and the Main Ethiopian Rift) , the Eastern Branch, and the Western Branch [*Chorowicz*, 2005] (Fig. 1A). The Kenya Rift, the focus of this study, is located within the Eastern Branch between the Turkana Depression in the north and the North Tanzania Divergence to the south (Fig. 1B). The landscape of the Kenya Rift (which constitutes a northern, a central, and a southern segment; henceforth NKR, CKR, and SKR) provides a unique opportunity for the documentation of the interplay between drainage incision, tectonic uplift, magmatic activities, and climate change. [*Smith and Mosley*, 1993; *Spiegel et al.*, 2007; *Torres Acosta et al.*, 2015; *Veldkamp et al.*, 2012]. However, both the short-term (10^3-10^6 yr) and the long-term (10^6-10^7 yr) drainage incision history of the rift are poorly constrained. Specifically, the spatial and temporal scales at which the tectonic uplift and the magmatic activities interact with each other as well as their influence on drainage incision have not been fully explained.

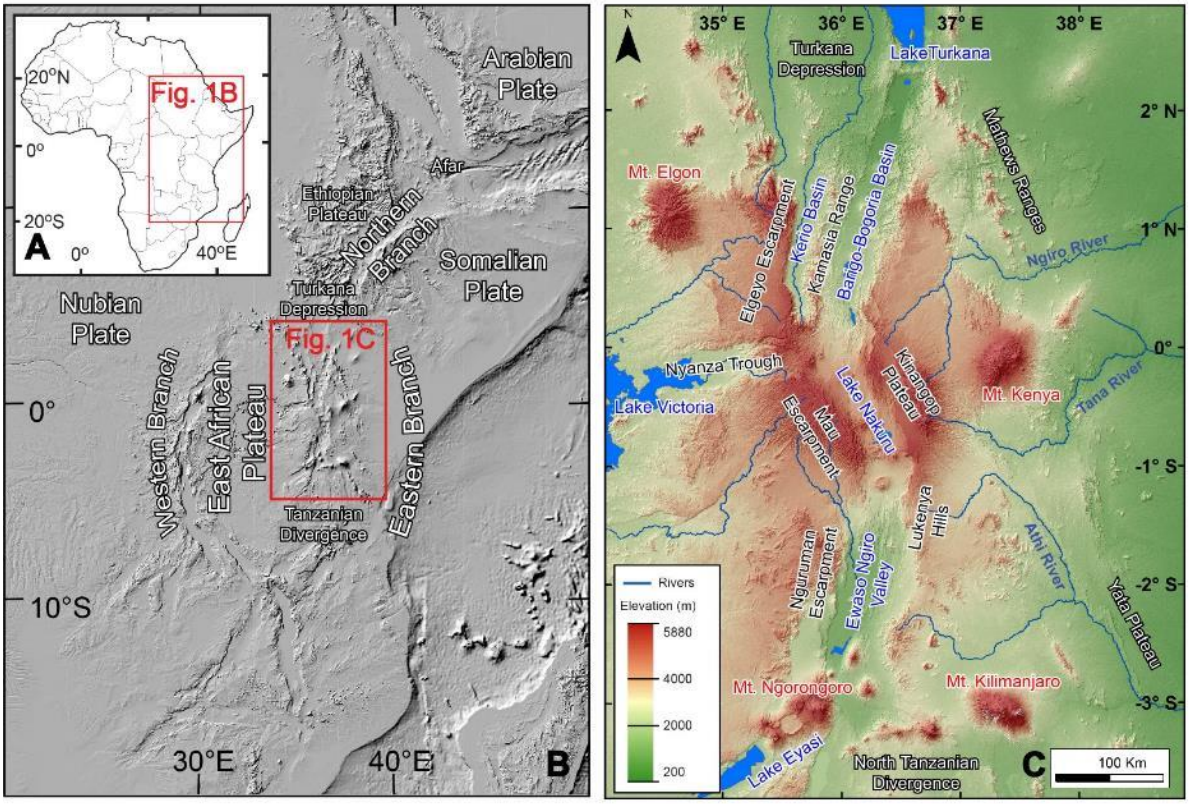

Figure 4- 1 (A) Index map of the East African Rift System (EARS). (B) ETOPO1 DEM of the EARS, showing the locations of the Arabian, Nubian, Somalian Plates, Eastern and Western Branches, the Main Ethiopian Rift, and the Afar Depression. (C) SRTM DEMs of the Kenya Rift, showing the North, Central, and South Kenya Rifts, and three major streams, including Ngiro River, Tana River, and Athi Rivers. This map also illustrates the locations of Lake Turkana, Lake Nakuru, Lake Victoria, Lake Eyasi, Mathews Ranges, Kamasia Range, Mau Escarpment, Nguruman Escarpment, Yatta Plateau, Elgeyo Escarpment, Kinangop Plateau, Nyanza Trough, Lukenya Hill, Mt. Elgon, Mt. Kenya, Mt. Kilimanjaro, Mt. Ngorongoro, Ewaso Ngiro Valley, Kerio Basin, and Baringo-Bogoria Basin.

Studies implenting ^{40}Ar-^{39}Ar and K-Ar ages of basaltic flows surfacing the Eastern Branch suggest southward migration of magmatic activities since the Eocene, where the ages of volcanic rocks decrease from the Turkana Depression in the north to the North Tanzania Divergence to the south (Fig. 1B) [e.g., *C J Ebinger and Sleep*, 1998; *Furman et al.*, 2004; *Moucha and Forte*, 2011; *Wichura et al.*, 2015]. This is further supported by numerical modeling suggesting that the dynamic topography associated with the EARS was developing since the Oligocene (~30 Ma) from north (the Ethiopia – Yemen plateau) to south (the East African plateau) [*Moucha and Forte*, 2011]. This southward migration of the dynamic topography has been explained as due to

northward movement of the African plate above the East African plume [*Moucha and Forte*, 2011]. However, (U-Th)/He and apatite/zircon fission track thermochronological analysis by [*Torres Acosta et al.*, 2015] have suggested that there exists an overlap in the timing of the development of the southern Main Ethiopian Rift in the north and the Kenya Rift to the south rather than southward propagation of the rifting processes thought to be driven by mantle plume activities.

This study aims at: (1) Using the short-term and long-term drainage incision to constrain the spatial and temporal variation in the tectonic uplift on the flanks of the Kenya Rift. (2) Comparing the variation in the tectonic uplift with the spatial and temporal distribution of volcanic flows of known ages in order to establish the relationship between the tectonic uplift and magmatic activities. (3) Correlating the drainage incision history of the rift flanks with major paleoenvironmental changes represented by vegetation shifting events.

4.2. Tectonic Setting and Evolution of the Kenya Rift

4.2.1. Regional Setting of the Kenya Rift

The Kenya Rift is localized in the center the Eastern Branch of the EARS on the eastern edge of the East Africa Plateau (Fig. 1A). The Eastern Branch represents part of the boundary between the Somalia Plate and the Victoria Plate, the latter is bounded in the west by the Western Branch which separates it from the Nubia Plate (Figs. 1A and B). The Eastern Branch of EARS is characterized by shallow seismicity where the seismogenic depth ranges between 5 and 15 km and more voluminous volcanism than the Western Branch [*Craig et al.*, 2011]. The Kenya Rift represents a N-S trending extensional structure that stretches for ~900 km starting from the Turkana Depression in the north to the North Tanzanian Divergence to the south (Figs. 1B, C and 2). Based on Global Positioning System (GPS) studies, the Victoria plate is currently moving

eastward away from the Nubian plate with a velocity of 1.1 mm/yr in the north and 2.9 mm/y in the south [*Saria et al.*, 2014]. Differently, the Somali Plate is currently moving with a velocity of 3.1 mm/yr in the north and 0.9 mm/yr in the south.

4.2.2.Precambrian Geology and its Influence on the Evolution of the Kenya Rift

The Kenya Rift stretches in a N-S direction along the Neoproterozoic East African orogen, which is represented by the juvenile crust of the Arabian-Shield in the north and the reworked and juvenile crust of the Mozambique belt to the south, which is represented by the Eastern and Western Granulite belts (Fig. 3) [*Fritz et al.*, 2013; *Katumwehe et al.*, 2016; *Stern*, 1994]. *Fritz et al.* [2013] considered the Eastern Granulite belt as a juvenile Neoproterozoic crust and the Western Granulite belt as an Archean – Paleoproterozoic crust that was reworked during the Neoproterozoic (Fig. 3). The East African orogen is found on the eastern side of Archean – Paleoproterozoic cratonic and metacratonic blocks represented, from north to south, by the Saharan Metacraton [*Abdelsalam et al.*, 2002], the Northeast Congo Block (which represents the northeastern extension of the Congo craton), and the Tanzania craton (Fig. 3; Katumwehe et al., 2016). The Western Granulite belt is a W-verging nappe that was thrust onto the eastern edge of the Tanzania craton (Fig. 3) [*Fritz et al.*, 2013]. Similarly, the Eastern Granulite belt is considered a W-verging nappe that was thrust westward onto different Precambrian tectonic entities (Fig. 3) [*Fritz et al.*, 2013]. *Katumwehe et al.* [2016] proposed that the boundary between the Northeast Congo craton and the Saharan Metacrton is the NW-trending sinistral strike-slip Aswan shear zone, which extends beneath the Miocene – Recent volcanic pile of the Kenya Rift to connect with the NW-trending sinistral strike-slip Nyangere shear zone which represent the boundary between the Eastern Granulite belt and the Arabian-Nubian Shield (Fig. 3) [*Fritz et al.*, 2013]. It is worth noting here that the CKR follows the projected trace that connects the two shear zone beneath the Miocene – recent volcanic pile of the Kenya Rift (Fig. 3).

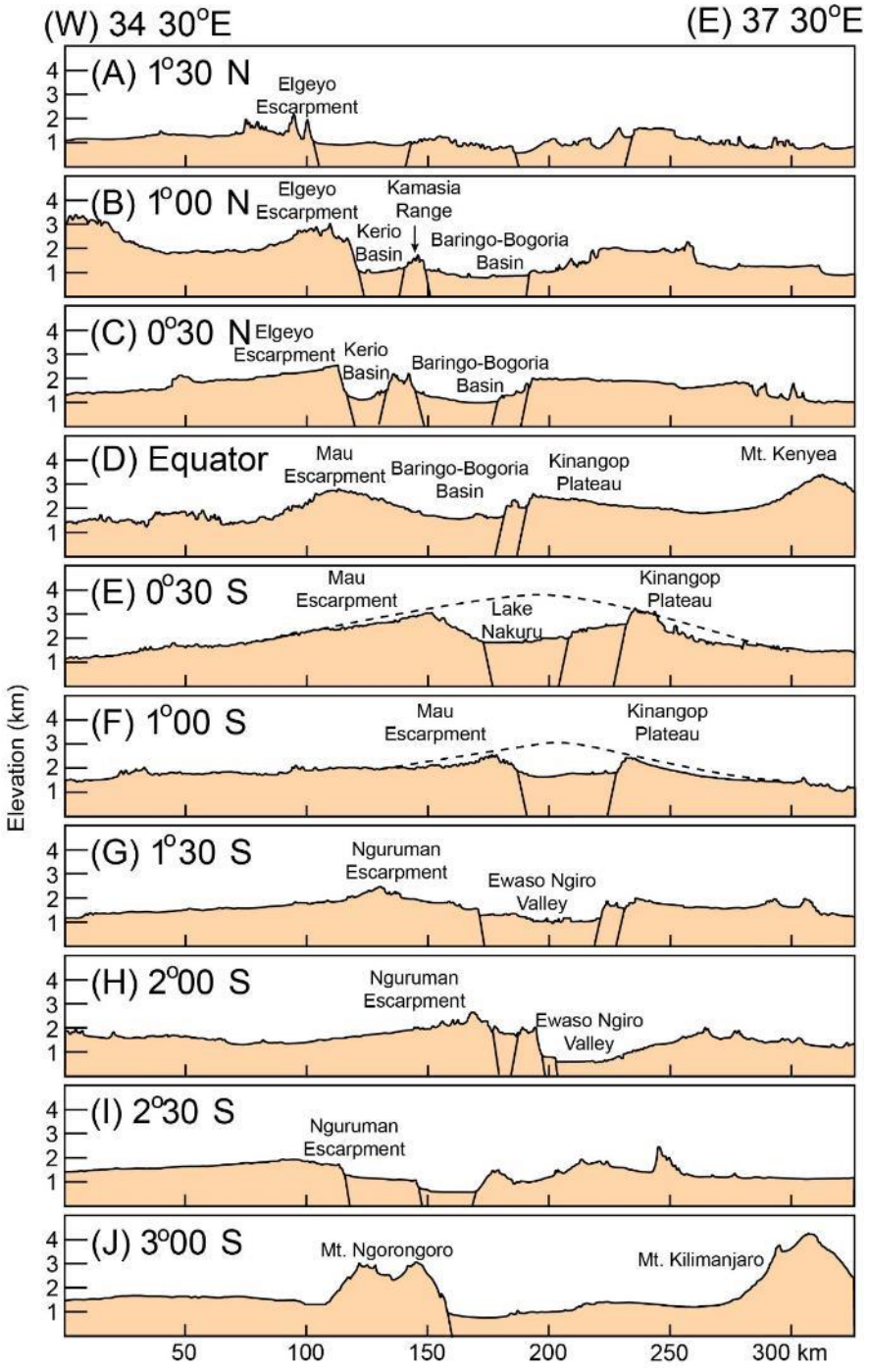

Figure 4- 2 Idealized east-west trending cross-sessions across the Kenya Rift spaced at 30' from 1°30' N to 3°00' S. The topography profiles are extracted from SRTM DEM. The location of rift basins and escarpments are based on the maps of Fig. 1C.

The Neoproterozoic East African orogen is considered the collision zone between East Gondwana (represented by the Galana terrane in Fig. 3) and West Gondwana (represented by the Saharan

Metacraton, Northeast Congo craton and Tanzania craton in Fig. 3) [*Abdelsalam and Stern*, 1996; *Fritz et al.*, 2013; *Shackleton*, 1984; *Shackleton and Ries*, 1984; *Stern*, 1994]. The geological variation along the orogenic belt, especially the grade of metamorphism, is explained as that Tibetan-type collision occurred in the south along the Mozambique Belt after the complete consumption of the Mozambique ocean whereas Andean-type orogeny occurred in the north allowing for the preservation of elements of the Mozambique ocean in the Arabian-Nubian Shield in the form of juvenile island arcs and ophiolites [*Abdelsalam and Stern*, 1996; *Stern*, 1994]. Recently, based on U-Pb zircon geochronological and isotopic data, Thomas et al. [2016], proposed that the Western Granulite belt represents the metacratonized portion of the eastern edge of the Tanzania craton and that this metacratonization occurred in association with the Neoproterozoic East African orogenic event.

It has been suggested that the lithospheric heterogeneity between the cratons and metacratons in the west (the Saharan metacraton, the Northeast Congo block, and the the Tanzania craton) and the East African orogen to the east might have influenced the development and propagation of the Kenya Rift [*C Ebinger et al.*, 1997; *Smith and Mosley*, 1993]. Seismic and gravity data indicated that the pre-existing lithospheric contrast between the two Precambrian tectonic entities might have also controlled the localization of extension, and the emplacement of magma since early Miocene [*Simiyu and Keller*, 2001; *Smith*, 1994].

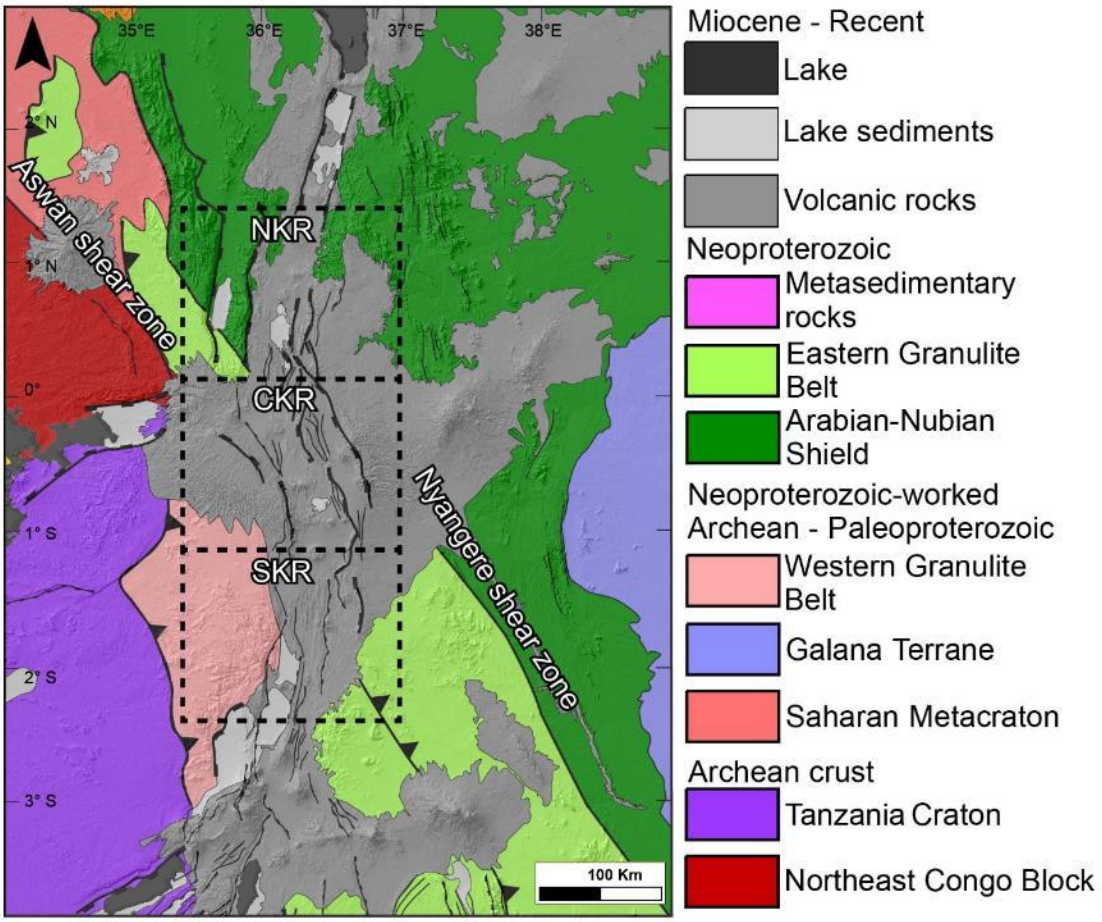

Figure 4- 3 Tectonic map of the Kenya Rift modified from Katumwehe et al., [2016], showing the locations of Aswan shear zone and Nyangere shear zone and sections of North, Central, and South Kenya.

Recently, using satellite gravity data to image the depth to Moho and the lithosphere – asthenosphere boundary (LAB), Fletcher et al. (Submitted) observed a NNE-trending zone of thin lithosphere on the eastern margin of the Tanzania craton. The eastern extent of this zone coincides with the thrust front of the Western Granulite belt. Fletcher et al. (Submitted) attributed the presence of this zone of thin lithosphere to sub-continental lithospheric mantle delamination that was controlled by the presence of a suture zone and that this delamination occurred during the East African orogenic event due to collision between East and West Gondwana.

Following Thomas et al. [2016] initial proposal, Fletcher et al. (Submitted) proposed that delamination might have resulted in metacratonization of the eastern edge of the Congo craton to

transform it into the Neoproterozoic-reworked Archean – Paleoproterozoic crust of the Western Granulite belt (Fig. 3). Further, Fletcher et al. [Submitted] proposed that the zone of thin lithosphere might have allowed the channelization of a mantle plume material that is deflected eastward due to the presence of the thicker root of the Tanzania craton as initially suggested by *Koptev et al.* [2015]. Fletcher et al. (Submitted), concluded that softening of the lithosphere at the eastern margin of the Tanzania craton through repeated geological event allowed for localization of extensional strain driven by the eastward movement of the Somali plate, hence the onset of the Eastern Branch of the EARS.

4.2.3. The Architecture of the Kenya Rift

The Kenya Rift is divided into the NKR, the CNR, and the SNR. The three segments are distinctively different in terms of orientation and geometry (Figs. 1C and 2). The region north of the Kenya Rift is dominated by the southern part of the Turkana Depression, which forms at its transition with the Kenya Rift a ~125 km wide depression bounded in the west by the ~1.0 km high Elgeyo escarpment (Fig. 2A). The NKR is composed of two N10°E striking grabens including the ~50 km wide Baringo-Bogoria Basin in the east and the ~20 km wide Kerio Basin to the west (Figs. 1C and 2B and C). These basins form parallel rift valleys separated by a horst structure referred to as the Kamasia Range (Fig. 2B and C [*Chorowicz*, 2005]. The Baringo-Bogoria Basin has an almost full graben geometry where the escarpments representing the border faults on both its eastern and western sides ~ 0.6 km high (Figs. 2B and C). The northern part of the Kerio Basin is a W-dipping half-graben in which the height of the Elgeyo escarpment in the west reaches ~2.0 km (Fig. 2B). Further south, the Kerio half- graben transition into an asymmetrical graben with better developed escarpment in the west (~1.2 km high) compared to the escarpment in the east (~0.8 km high) (Fig. 1C). The Baringo-Bogoria Basin extends southward to Lake Bogoria, while the Kerio Basin ends west of this lake (Fig. 1C).

The transition from the NKR to the CKR is marked by a shallow (0.5 km deep), E-dipping and ~50 km wide half-graben bounded by the Kinangop plateau in the east and the Mau Escarpment to the west (Fig. 2D). This is also where the Kenya Rift intersects with the N80^{o}E trending Nyanza Trough (Fig. 1C) [*Chorowicz*, 2005]. The N10°W CKR extends from south of the Baringo - Bogoria Basin, through the Lake Nakuru, to the northern part of the Ewaso Ngiro Valley surrounded by the Kinangop escarpment in the east and the Mau Escarpment to the west (Figs. 1C and 2D-F). The central part of the CKR is dominated by an ~80 km wide full graben where the escarpments representing the border faults in the east and west are ~1.0 km high (Fig. 2D). The elevation of this escarpment at the margins of the CKR is ~3.0 km, and this elevation gradually decreases to the east and west away from the rift to reach ~1.0 km. This suggests that the CKR was superimposed on a broad domal topography (Fig. 2E). Further south, the CKR narrows to a width of ~50 km and forms a full graben bounded between ~0.9 km high escarpments (Fig. 2F). Similar to its central part, the southern part of the CKR seem to be superimposed on a broad domal topography where the Kinangap plateau in the east and the Mau Escarpment to the west have elevations of ~2.5 km at the eastern and western escarpment, and they become progressively lower in elevation eastward and westward away from the rift reaching ~1.5 km (Fig. 2F).

The transition between the CKR and the SKR is marked by the northern part of the N-S trending Ewaso Ngiro Valley (Fig. 1C). Here, the Kenya Rift is defined by a ~60 km wide full graben bounded by the ~0.8 km high Lukenya Hills in the east and the Mau – Nguruman escarpment to the west (Fig. 2G). The central part of the N15°E striking SKR is represented by a W-dipping half graben in which the surface expression of the border fault is defined by the ~1.0 km high eastern edge of the Nguruman escarpment (Fig. 2H). Further south, the SKR is defined by a ~60 km wide and relatively poorly defined graben bounded in the west by the Nguruman escarpment, the eastern edge of it has a height of only ~0.5 km (Fig. 2I). The boundary between the SKR and the

North Tanzania Divergence can be assigned to an E-W trending volcanic belt dominated in the east by Mount Kilimanjaro and in the west by Mount Ngorongoro (Fig. 2J)

4.2.4. Magmatic Activities, Tectonic Uplift, and Rifting

Based on available $^{40}Ar/^{39}Ar$ and K/Ar ages, this work produced a geological map showing the spatial distribution of magmatic activities covering the epochs between Eocene and Holocene (Fig. 4). This will be discussed in more details in section 4.4.1. Earlier, *Nyblade and Brazier* [2002] proposed that magmatic activities commenced between 45 and 37 Ma in the southern Main Ethiopian Rift, between 39 and 45 Ma in the NKR, at ~15 Ma in the CKR, and at ~8 Ma in North Tanzania Divergence. Based on the oldest magnetic activity recorded in the Kenya Rift, it is suggested that the initiation of rifting in the Kenya Rift started during the Eocene [*Cynthia Ebinger and Scholz*, 2012; *C K Morley et al.*, 1992]. This is because it is considered that magmatic activities occurred at the same time of rifting [*C Ebinger*, 1989]. However, studies aimed at determining the onset of fault activities in the Kenya Rift revealed much younger ages. For example, by using K-Ar dating and palaeomagnetic polarity measurements on the Nguruman escapement in the SKR (Fig. 1C), *Robert Crossley* [1979] suggested that the activity on the border faults started at ~7 Ma. Additionally, *Macdonald* [2002] suggested, from geochrnology, that rifting in the CKR and the SKR started latter than ~10 Ma, and it propagated southward to reach the North Tanzania Divergence between ~8 and ~5 Ma.

Using thermal models from apatite fission track and zircon (U-Th)/He thermochronology, *Torres Acosta et al.* [2015] revealed a three-phase cooling history on the flanks of the NKR and the CKR. This includes rapid cooling between ~65 and ~50 Ma, a very slow cooling between ~45 and ~15 Ma, and a renewed rapid cooling starting at ~15 Ma.

4.2.5. Mantle Dynamics beneath the Kenya Rift

It is suggested that a significant part of the tectonic uplift and magmatic activities in the EARS is associated with mantle plume activities [e.g., *C Ebinger*, 1989]. However, there remain uncertainties about the nature of these mantle plume activities. *C J Ebinger and Sleep* [1998] suggested that the EARS is impacted by a single mantle plume beneath the Ethiopia-Yemen plateau since the Cenozoic. The presence of a single mantle plume is further supported by geochemical studies from the Turkana Depression suggesting the presence of a long-lived mantle plume beneath the Ethiopia-Yemen plateau and the East Africa plateau [Furman et al., 2004]. These geochemical observations implied a single, large, but chemically heterogeneous plume with small (<500 km diameter) and isolated plume heads [Furman et al., 2006; Pik et al., 2006]. The presence of a single mantle plume is further supported by time-dependent dynamic topography modeling for the past ~30 Ma that explained the development of dynamic topography associated with the EARS is due to northward movement of the African plate above a stationary and deep-seated superplume that resulted first in the development of the Ethiopia-Yemen plateau in the north and then the East Africa plateau to the south [Moucha and Forte, 2011].

However, geochemical studies have shown distinct differences between volcanic rocks in the Ethiopia-Yemen plateau and the East Africa plateau implying the existence of at least two (Afar and Kenya) different mantle plumes beneath the EARS [*George et al.*, 1998; *Rogers et al.*, 2000]. The Kenya mantle plume is considered to have reached the base of African continent lithosphere earlier (at least 45 Ma) than the Ethiopia mantle plume (~30 Ma) [*Rogers et al.*, 2000]. It is also suggested that the Kenya mantle plume is responsible for the magmatism extending from the southern Main Ethiopian Rift, through the Kenya Rift, to the North Tanzania Divergence [*Rogers et al.*, 2000]. The Afar mantle plume is considered to be associated with magmatism of the Afar Depression and the northern Main Ethiopian Rift Ma [*Pik et al.*, 2006].

Further, *Koptev et al.* [2015] using numerical modeling explained the development of the Eastern Branch as a magma-rich continental rift due to eastward deflection of a mantle plume rising

beneath the thick root of the Tanzania craton. *Emishaw et al.* [2017] considered the magmatic activities and the tectonic uplift in the Main Ethiopian Rift and the Afar Depression to be associated with an NE-directed mantle flow that is rising from the northern part of the Turkana Depression.

4.3. Data and Methods

Three types of data are used in this study: (1) Published geological and $^{40}Ar/^{40}Ar$ and K/Ar geochronological data [e.g., *Brotzu et al.*, 1984; *A Foster et al.*, 1997; *Guth*, 2016; *Opdyke et al.*, 2010; *Smith*, 1994, full reference please refer to the Appendix 3; *Wilkinson et al.*, 1986] to map the spatial distribution of remnants of different volcanic rocks and assign specific ages for them (Fig. 4). (2) Sentinel-2A multi-spectral remote sensing data to further map the detailed spatial distribution of the volcanic remnants. This is a high spatial resolution (10 m - 20 m), multi-spectral imaging mission initiated by European Space Agency [*Drusch et al.*, 2012]. (3) 30 m spatial resolution SRTM DEM to establish (in connection with the location and age of various volcanic remnants) a paleo-datum. The SRTM DEM is also used to produce a regional incison map by subtracting modern topography from the paleo-datum. Subsequently, the long-term drainage incision rate is calculated by dividing the amount of regional incision by the ages of the volcanic remnants following *Gallen et al.* [2013], *Schoenbohm et al.*[2004], and *Thouret et al.*, [2007]. The SRTM DEM is also used to establish the short-term incision rate and drainage divide

movement using chi-integral geomorphic proxy [*Perron and Royden*, 2013; *Willett et al.*, 2014].

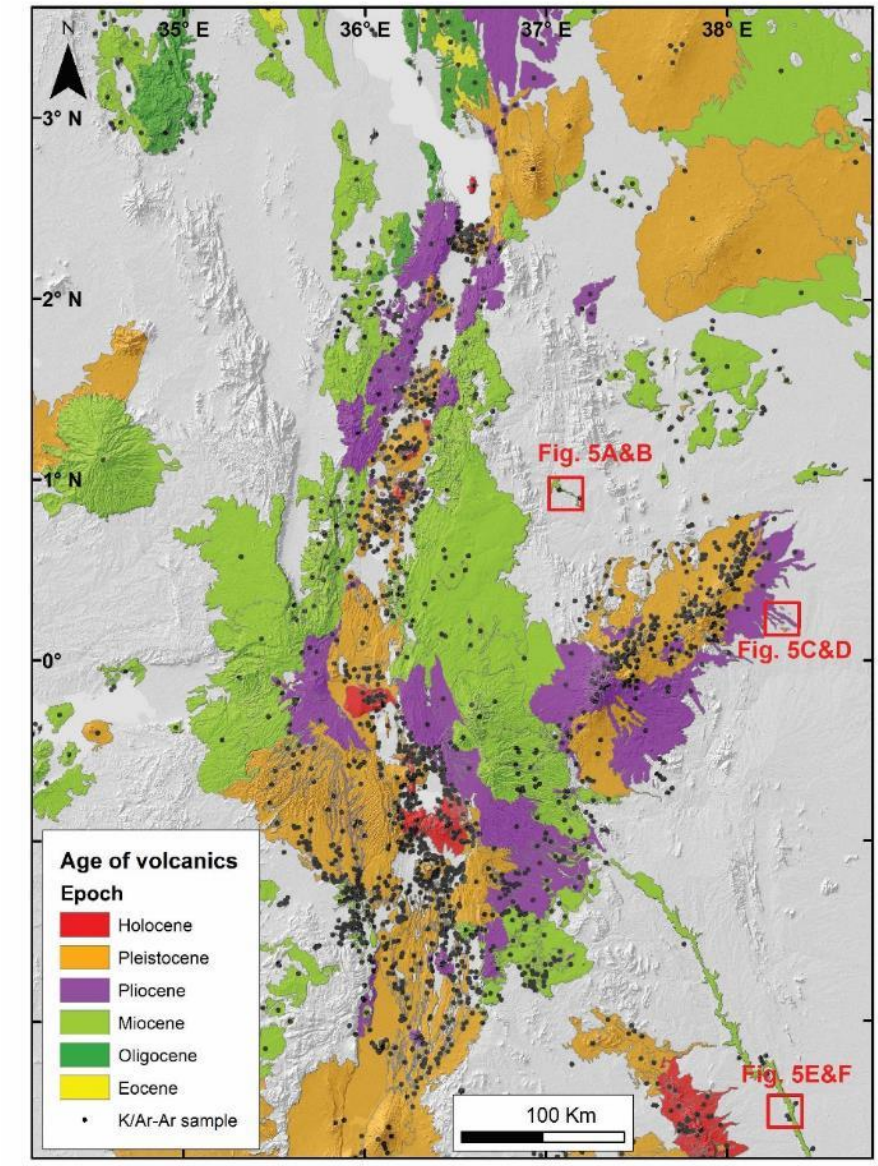

Figure 4- 4 Map of volcanic rock remnants in the Kenya Rift. The extents of these remnants are constrained by former geological maps [Guth, 2016; Milési et al., 2004; Pulfrey, 1969] and Sentinel-2A data, while, the age of these remnants are derived from Ar/K-Ar data (see Appendix 1). The red boxes illustrate three examples used for Figure 5.

4.3.1. Establishing Long-term Drainage Incision Rate

To establish the long-term drainage incision rate for the Kenya Rift, this work first produced a geological map for the distribution of Miocene to Recent volcanic remnants by synthesizing results from geological maps and published $^{40}Ar/^{39}Ar$ and K/Ar geochronological data (Fig. 4).

The location and extent of these volcanic remnants were first mapped by integrating the 1:3,000,000 geologic map produced by the Geological Survey of Kenya [*McCall*, 1967, Scale: 1:3, 000, 000] and geologic maps from *Guth* [2016]. Various $^{40}Ar/^{39}Ar$ and K/Ar geochronological studies have been carried out for the volcanism in the Kenya Rift since 1970s [*B H Baker and Mitchell*, 1976; *Brotzu et al.*, 1984; *A Foster et al.*, 1997; *McDougall et al.*, 2012; *Opdyke et al.*, 2010]. These studies have been reviewed by *Smith* [1994] and *Guth* [2016]. More than 2000 geochronological data points are used to provide age constraints on widely distributed volcanic remnants throughout the Kenya Rift (Fig. 4) (Appendix 3).

To further constrain in detail their spatial extent, the boundaries of the volcanic remnants obtained from the geologic maps are adjusted using Red-Green-Blue (RGB) color combination images extracted from Sentinel-2A multi-spectral data. Three examples of 12-8-3 RGB color combination images from the Sentinel-2A data that are used to map the volcanic remnants of the Kenya Rift are shown in Fig. 5.

Based on the detailed map of volcanic remnants and their associated age, this study estimated the long-term drainage incision rate by reconstruction of the pre-incision paleo-datum in the SRTM DEMs [*Prince and Spotila*, 2013]. These remnants are widely distributed on the flanks of the Kenya Rift and are highly dissected by the drainage system. For example, three major streams are observed incising into these volcanic rocks including the Ngiro River (Figs. 5A and B), the Tana River (Figs. 5C and D), and the Athi River (Figs. 5E and F). Second, the amount of long-term drainage incision is assumed to be represented by the elevation difference between the paleo-datum and the present topography. Third, the long-term incision rate is estimated by dividing the incision magnitude by the ages of the volcanic remnants.

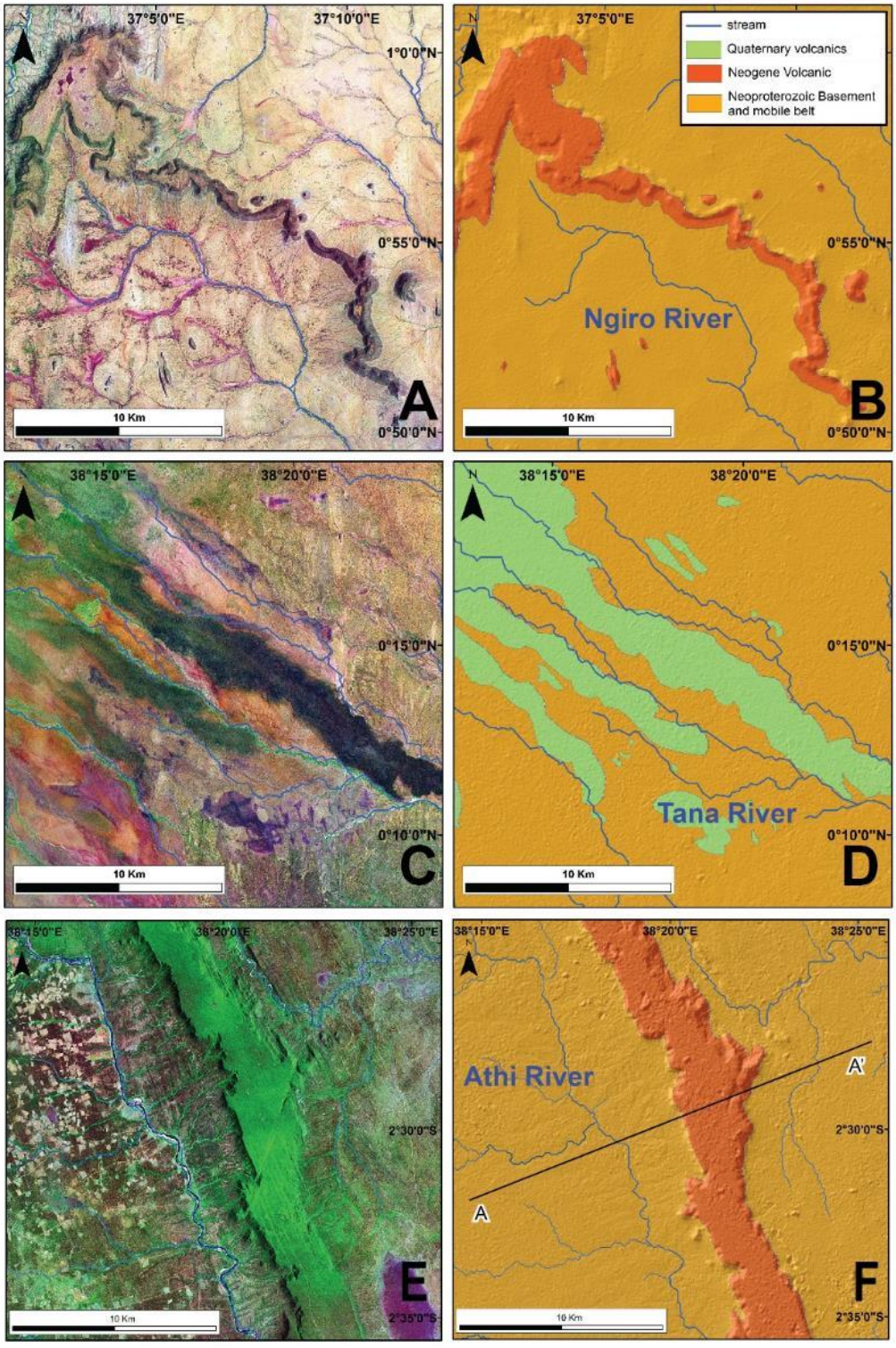

Figure 4- 5 False color image for the Ngiro River (A), the Tana River (C), and the Athi River (E), extracted from Sentinel-2A satellite data with band combination (11/8/3), which highlights the iron oxide and magnetite. Three examples illustrate the incision on the Neogene and Quaternary volcanics (B, D, and F) and also the locations used for calculating the long-term incision rates (F).

This work presents the Athi River (Figs. 5E and F) as an example to illustrate the methods applied to calculate the long-term drainage incision rates. The long-term incision rate of the Athi River is calculated by using the Yatta plateau located parallel and to the east of the Athi River (Figs. 5E and F). The ~300-km-long Yatta plateau is considered to be the longest inverted valley on Earth [*Wichura et al.*, 2010]. This plateau was developed by southeastward flow of ~13.5 Ma phonolitic flow. This lava followed the paleo valley of the Athi River [*Veldkamp et al.*, 2007; *Wichura et al.*, 2011] (Fig. 6A). Subsequently, erosion of the Precambrian materials occurred, resulting in the lava-filled valley that formed the ~250 m high Yatta Plateau (Fig. 6B). Therefore, the top of the Yatta plateau represents the minimum elevation of the Miocene (~13.5 Ma) paleo-datum. Subsequently, the amount of the drainage incision was calculated by subtracting the elevation of the longitudinal profile of the Athi River from that of the Yatta plateau. With the assumption that incision occurred shortly after the formation of the Yatta Plateau, this work calculated the long-term drainage incision rate to be 18.52 mm/ky by dividing the amount of drainage incision (~250 m) by the age of phonolite (~13. 5 Ma).

Because of the availability of the detailed map of the volcanic remnants and their $^{40}Ar/^{39}Ar$ and K/Ar ages (Fig. 4), a total of 85 drainage incision rate data points are calculated for the three segments of the Kenya Rift. Twenty one data points are found within the NKR, 29 within the CKR, and 35 within the SKR. Subsequently, the discrete data points of drainage incision rate are plotted against the age of the volcanic remnants (Fig. 7). Furthermore, because it is observed that the most extensive magmatic activities in the Kenya Rift were recorded in the middle Miocene (~15 Ma) and the Pliocene (~4.5 Ma), two maps showing the distribution of drainage incision rate during ~15 Ma and ~4.5 Ma period were constructed by using nearest-neighbor interpolation of

the 85 discrete data points (Figs. 8 A and 8 B).

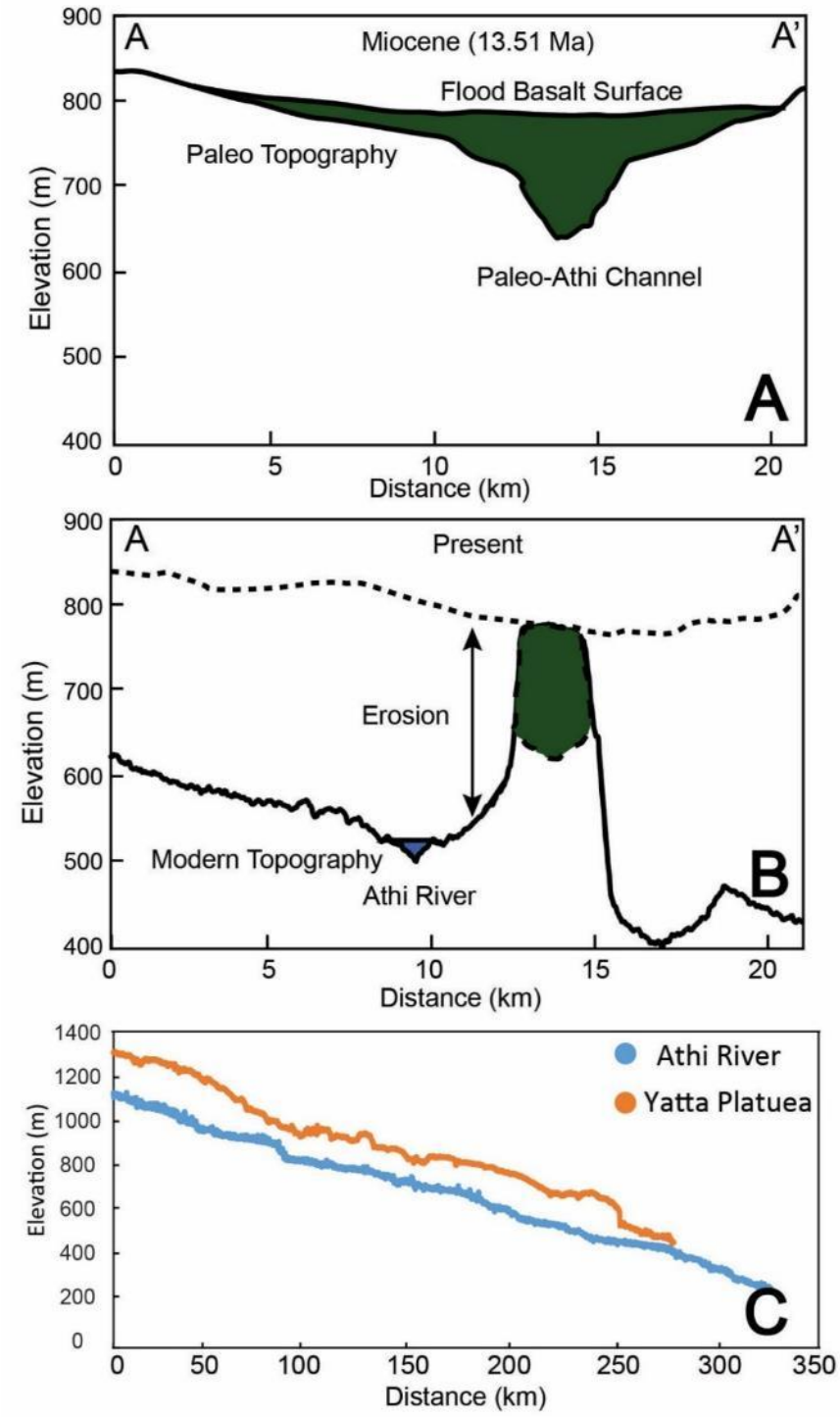

Figure 4- 6 Cross section along A-A' for Yatta Plateau (Figs. 5 EF) showing the conceptual map of Miocene paleo topography (A), and the present topography (B) illustrating more than 200 m incision of Athi River since Miocene. (C) The longitudinal profile of the Athi River and projected Yatta Plateau, showing the estimation of the incision along the plateau.

4.3.2. Establishing Short –term Incision (4.5 Ma)

The pattern of the short-term drainage incision rate in the three segments of the Kenya Rift was evaluated using the chi integral geomorphic proxy (Figs. 9 and 10). The chi integral, can be used as a proxy for evaluating the steady-state condition of the drainage systems network, in length units [*Perron and Royden*, 2013; *Willett et al.*, 2014]. In the steady-state condition, the channel slope can be expressed as:

$$S = \frac{dz}{dx} = (\frac{E}{K})^{\frac{1}{n}} A^{\frac{-m}{n}} \quad (1)$$

where S is the local slope of the stream's longitudinal profile, A is the area of the drainage basin, z is the local elevation, x is horizontal coordinate, E is the drainage incision rate, K is erosional coefficient, and m and n are empirical constants [e.g., *Whipple and Tucker*, 1999]. The chi integral can be calculated by the integration of equation (1):

$$z(x) = z_b + (\frac{E}{K A_0^m})^{\frac{1}{n}} \boldsymbol{\chi} \quad (2)$$

with

$$\chi = \int_{x_b}^{x} (\frac{A_0}{A(x)})^{\frac{m}{n}} dx \quad (3)$$

where A_0 is a reference area within the drainage basin and z_b is the elevation at the outlet of the drainage basin. Hence, given the linear form of equation (2), the chi integral is useful to evaluate the dynamic state of the divide between drainage basins [*Willett et al.*, 2014]. Also, the change in chi integral values across the drainage basin divide are suggestive of the long-term divide migration direction [*Beeson et al.*, 2017; *Willett et al.*, 2014].

To evaluate the pattern of the short term drainage incision rate in the three segments of the Kenya Rift, this work produced a chi plot by plotting the elevation of major streams (Fig. 9A) in the eastern flank of the NKR, CKR, SKR versus the chi integral (Fig. 9B). The streams on the eastern flanks of the Kenya Rift are selected for the chi plot because their mouths to the Indian Ocean have the same elevation and are close and witnessed the same rise and fall of the base level. Also, the chi integral values are calculated for the streams in the three segments of the Kenya Rift (Fig. 10) from the SRTM DEM using the Topotool Box 2 [*Schwanghart and Scherler*, 2014]. To keep the main streams relatively consistent and straight, we applied concavity of 0.4 for the calculation. We applied reference area A_0 of 1 m^2 and minimum drainage area of 1000 m^2. Also, to highlight the drainage divide and basin boundaries, we have established a number of sub-basins throughout the Kenya Rift and numbered them from 1 to 110 according to their relative locations (Figs, 10A-C).

4.4. Results

4.4.1. Distribution of remnants of volcanic rocks from Miocene to Recent

Based on the age of volcanic remnants, it is found that the two major phases of extrusive volcanism occurred in the middle Miocene (16-8 Ma) and the Pliocene (5.3-1.6 Ma). These represent the majority of exposure of volcanic rocks in the Kenya Rift (Fig. 4). Only restricted outcrops of the oldest Eocene and Oligocene volcanism is observed in the NKR (Fig. 4). Nevertheless, no pattern of north to south younging of volcanic rocks is observed. Rather, it was noticed that the first phase of extrusive volcanism (16-8 Ma) spread throughout the NKR, the CKR, and the NKR. However, the second phase (5.3-1.6 Ma) is more concentrated within the CKR and some parts of the SKR. Such a volcanism distribution pattern generally matches the observation of flood basalt extents from *Smith* [1994] and *Claessens et al.* [2016](Figs. 8 AB).

4.4.2. Long-term Incision Rate

The long-term incision rate varies from 0.9 mm/ky to 276. 92 mm/ky (Fig. 7). Notably, before ~4.5 Ma the long-term drainage incision rate throughout the three segments of the Kenya Rift was below 50 mm/ky (Fig. 7). The rate rapidly increased in the CKR and the SKR after 4.5 Ma, where the CKR witnessed a drainage incision rate as high as 276 mm/ky, and the SKR witnessed a drainage incision rate that reaches 130 mm/ky (Fig. 7). Differently, the drainage incision rate of the NKR remained below 50 mm/ky even after ~4.5 Ma.

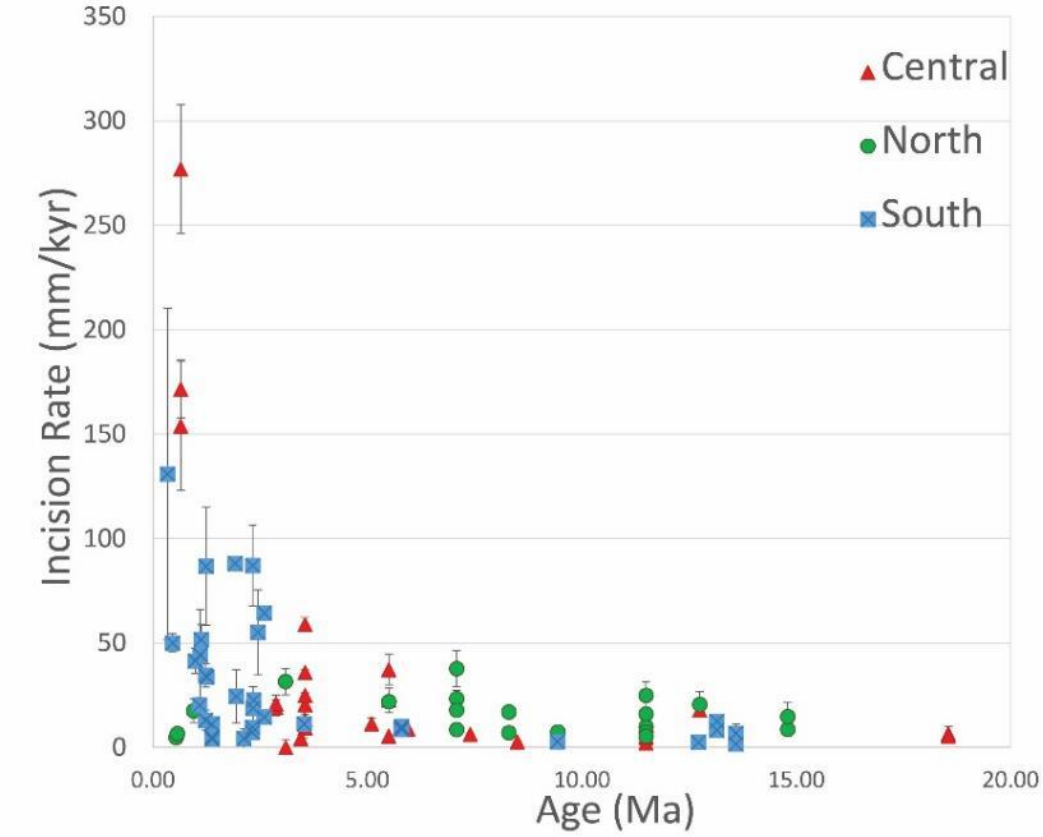

Figure 4- 7 Long-term incision rates for North, Central, and South Kenya Rift, the error is derived from the ±σ values of the Ar-Ar and K-Ar dates.

The drainage incision rate at ~15 Ma is relatively low (<60 mm/ky) throughout the three segments of the Kenya Rift and only a few regions in the NKR and CKR have drainage incision rates higher than 30 mm/ky (Fig. 8A). The drainage incision rate at ~4.5 Ma showed significantly higher rates in the CKR compared to other segments of the Kenya Rift. The SKR has a slightly

higher drainage incision rate than that of the NKR.

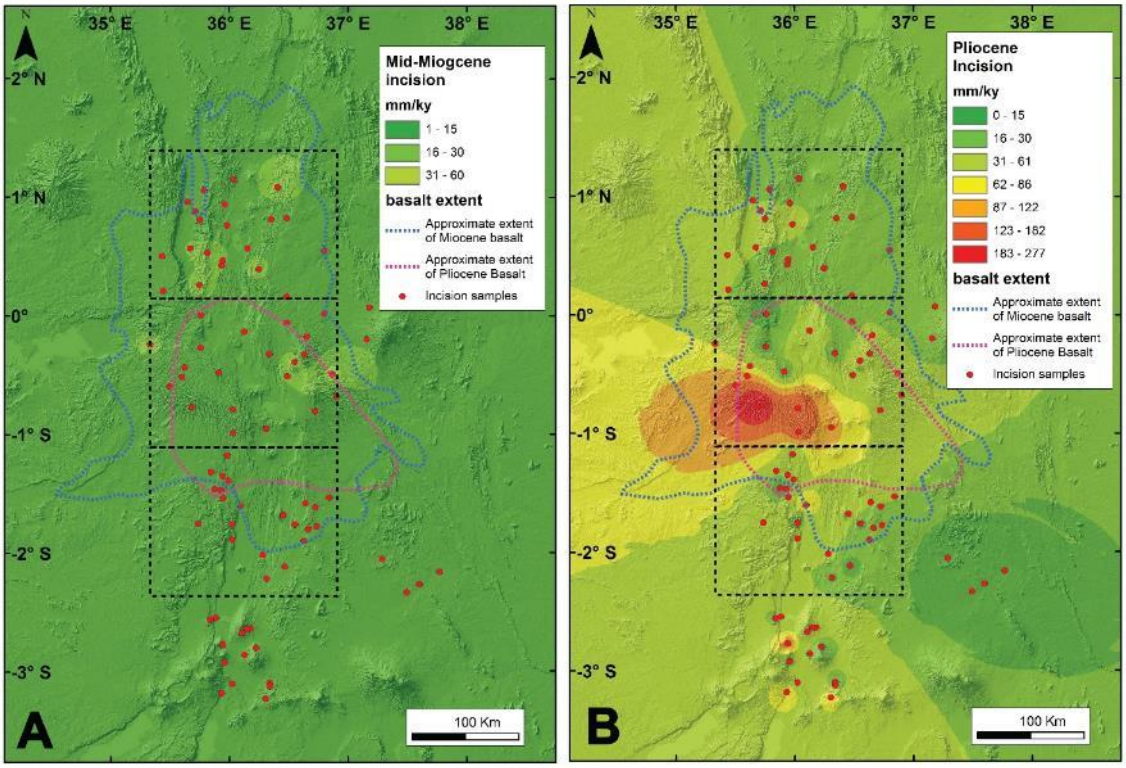

Figure 4- 8 Interpolated map of the incision rates in the Miocene (A) and Pliocene (B), showing the incision rate increases rapidly in the central Kenya Rift since Pliocene. Also, the red and blue dashed lines are the approximate extents of flood basalts in Pliocene and Miocene, respectively. These flood basalt extents are modified after Smith [1994] and Claessens et al. [2016].

4.4.3. Short-term Incision Rate

It is observed from the chi-plot that the streams on the flanks of the SKR and the NKR have similar pattern showing shallow slope from upstream. Differently, the streams on the flanks of the CKR have steeper slope (Fig. 9B). Therefore, it can be easily observed that the streams in the CKR have a higher channel steepness and associated drainage incision rate than those of the SKR

and the NKR.

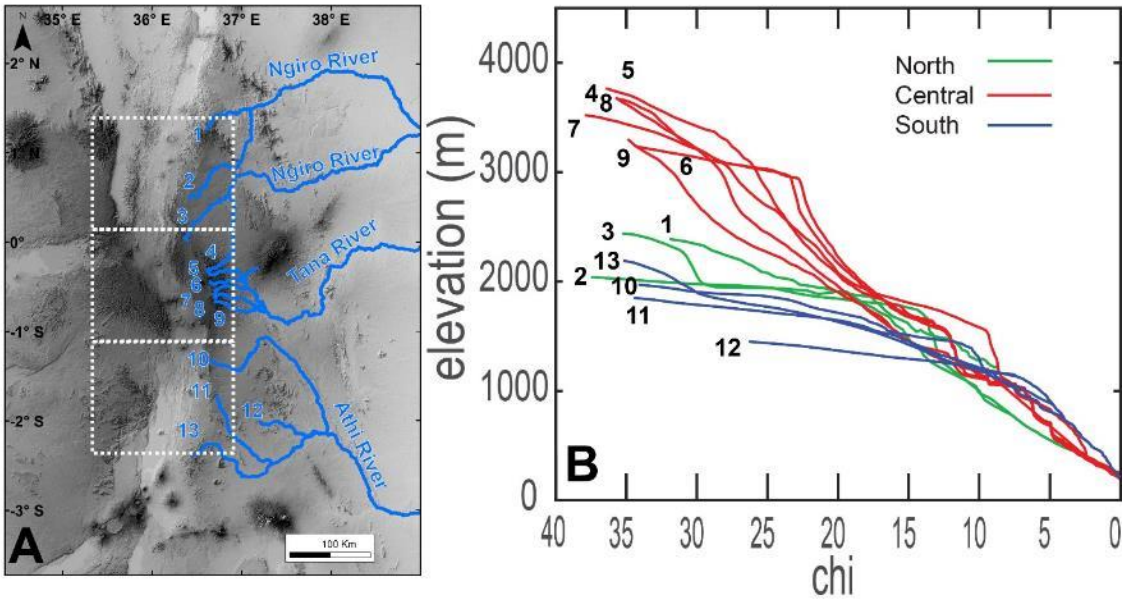

Figure 4- 9 (A) Hillshade map illustrating the locations of the major branches of Ngiro River, Tana River, and Athi River, which are labelled form 1 to 13 from north to south. (B) chi plot of the 13 streams on the eastern flanks of the Kenya Rift, showing the distinct patterns between Central KR and S/N KR.

The chi map is indicative of the migration direction of the drainage divide between drainage basins. It is found that the drainage divide migration in both the eastern and western flanks of the NKR is limited, where the chi values across the drainage divide are relatively similar (e.g., divides between drainage basins 93 and 54, 59 and 1, 55 and 53 in Fig. 10A). This suggests an equilibrium stage of these drainage divides. However, the drainage divides in the southeastern flank of NKR exhibit an eastward migration (e.g., divides between 78 and 62, 57 and 62 in Fig. 10A). In the CKR, the chi values across the divides of drainage basins show significant difference, representing relatively high migration, especially in the western flank of CKR (Fig. 10B). In the CKR, the direction of the drainage divide migration is consistent with E-W directed extension, where the drainage divide in the western flanks moved to the west, and those in the eastern flank moved to the east. Similar to the NKR, the drainage divides on the eastern and western flanks of the SKR are suggestive of an equilibrium stage, where, for the most part, the chi

are similar (e.g., divides between 45 and 81, 43 and 85, 42 and 105, 37 and 109, 110 and 107 in Fig. 10C).

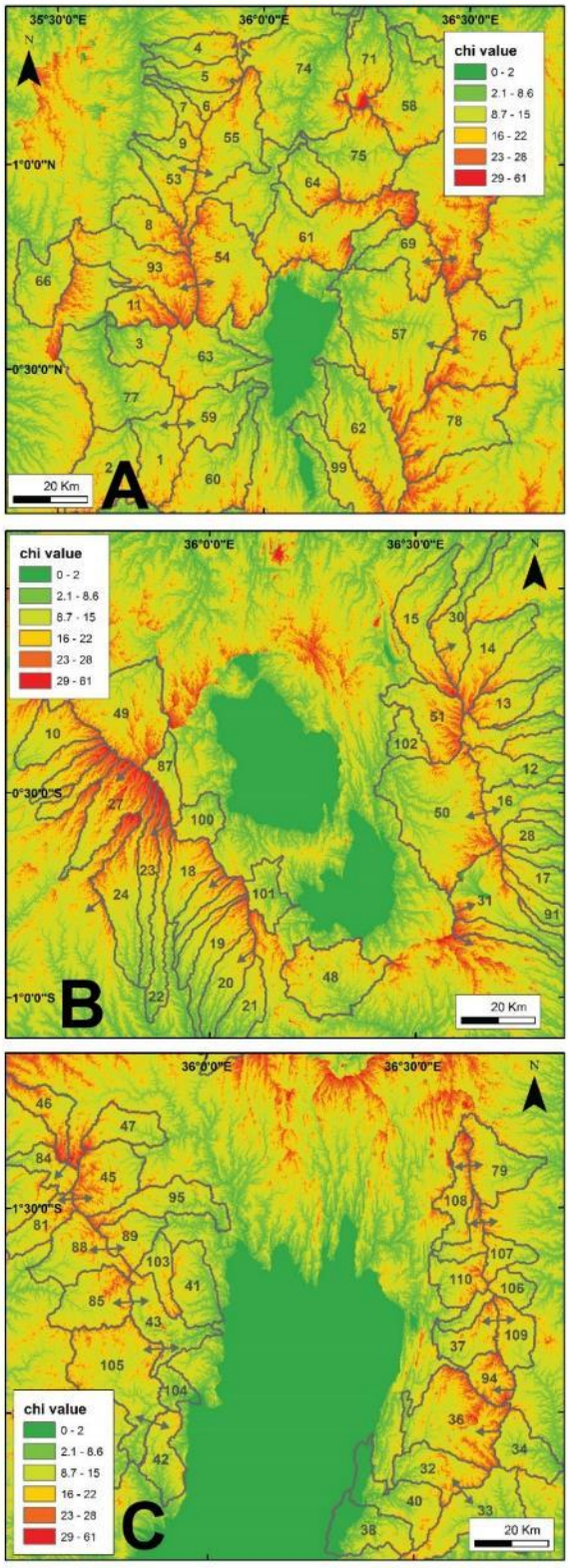

Figure 4- 10 Chi value maps showing the migration direction of drainage basins, in North (A), Central (B), and South (C) Kenya.

4.5. Discussion

4.5.1. Distribution of Drainage Incision in the Kenya Rift

The results obtained from the distribution of long-term and short-term drainage incision of the Kenya Rift are consistent. Both showed that the CKR is characterized by a higher drainage incision rate since ~4.5 Ma (Fig. 7) and have witnessed more pronounced drainage basin divides migration (Figs.9 and 10B). This suggests differential drainage incision patterns for the three segments of the Kenya Rift. This observation is consistent with a number of previous studies. First, *Wagner et al.* [1992] reported that the cooling history of the basement rocks at different segments of the Kenya Rift is different. Second, using Bouguer gravity anomalies and density models, *Bechtel et al.* [1987] calculated the locally compensated topography, which indicated a highly uplifted CKR and a westward rise of the East African Plateau. Third, *C Morley and Bosworth* [1988] mentioned that widely distributed phonolite flows erupted onto both the eastern and western rift flanks in 13.5 -11 Ma.

Further, the higher drainage incision rate in the CKR since 4.5 Ma coincides with the distribution of volcanic activities where Pleistocene volcanic rocks are found concentrating in the CKR (Fig. 4). The incision map of the middle Miocene (16-8 Ma, Fig. 8A) shows that higher drainage incision rates (30-60 mm/ky) coincides with regions that witnessed the extrusion of middle Miocene flood basalt. Similarly, the incision map of the Pliocene (5.3 – 1.6 Ma) shows that the higher drainage incision rate (>100 mm/ky) coincides with regions that witnessed Pliocene extrusion of Pliocene flood basalts in the CRK. Therefore, the rapid increase in the drainage incision rate in the CKR may be related to magmatic upwelling and associated tectonic uplift. This association between magmatism and tectonic uplift is also suggested for the Southeastern Ethiopian Plateau [*Xue et al.*, 2018].

Dynamic topography modeling and Ar-Ar geochronological data have suggested southward younging in the age of magmatism and rifting in the EARS [e.g., *C J Ebinger and Sleep*, 1998; *Furman et al.*, 2004; *Moucha and Forte*, 2011; *Wichura et al.*, 2015]. However, this work has shown that the drainage incision rate within the Kenya Rift are higher in the CKR compared to the NKR and SKR, rather than showing a southward increase in the drainage incision rate. This observation is also supported by recent thermochronology study and volcanism studies [*Michon*, 2015; *Torres Acosta et al.*, 2015]. For example, a summary of Ar-Ar geochronological data on the volcanic activities showed that the north to south migration of volcanism and tectonic activities is not applicable to some regions in the EARS [*Michon*, 2015]. Rather, *Michon* [2015] suggested that volcanic eruptions in the EARS are largely controlled by Precambrian lithospheric-scale suture zones and shear zones. The three segments of the Kenya Rift extends within different pre-existing Precambrian structures. The NKR is extending on the juvenile crust of the Arabian – Nubian Shield the CKR extends parallel to the Eastern Granulite Belt, and the SKR stretches along the boundary between Eastern and Western Granulite belts (Fig. 3). Therefore, it is possible that the variation in the underlying Precambrian lithospheric structures played a role in the variation in geometry, tectonic uplift, and magmatism in the three segments of the Kenya Rift.

Furthermore, this work showed that the eastern and western flanks of the Kenya Rift possessed different drainage incision patterns. By applying apatite (U-Th)/He thermal modeling, *Spiegel et al.* [2007] suggested a rapid cooling between ~7 Ma and ~4 Ma in the eastern flank and between ~5 Ma and ~2 Ma in the western flank in the NKR and CKR (Fig. 9B). Also, *C J Ebinger* [1989] demonstrated that the displacement of border faults in the western flank of the CKR is greater than that of the eastern flank, which implied differential tectonic uplift rates between the eastern and western flanks of the rift. Results from the chi analysis (Figs. 10 A-C) also suggested a more expressed drainage divide migration in the western flank than that of the eastern flank of the CKR. Based on seismic data, *Birt et al.* [1997] reported the existence of a mantle-plume

circulation beneath the uplifted East African Plateau to the west of the Kenya Rift. This asymmetry in incision and the inferred tectonic uplift may also be related to the composition-derived crustal density difference, where the crust density of western Kenya is <2880 kg/ m^3, while that the that of eastern Kenya is >2880 kg/m^3 [*Sippel et al.*, 2017]. Similarly, gravity and seismic interpretation suggested an asymmetry in crust thickness and faults displacement between the eastern and western flanks of the Kenya Rift [*Simiyu and Keller*, 2001].

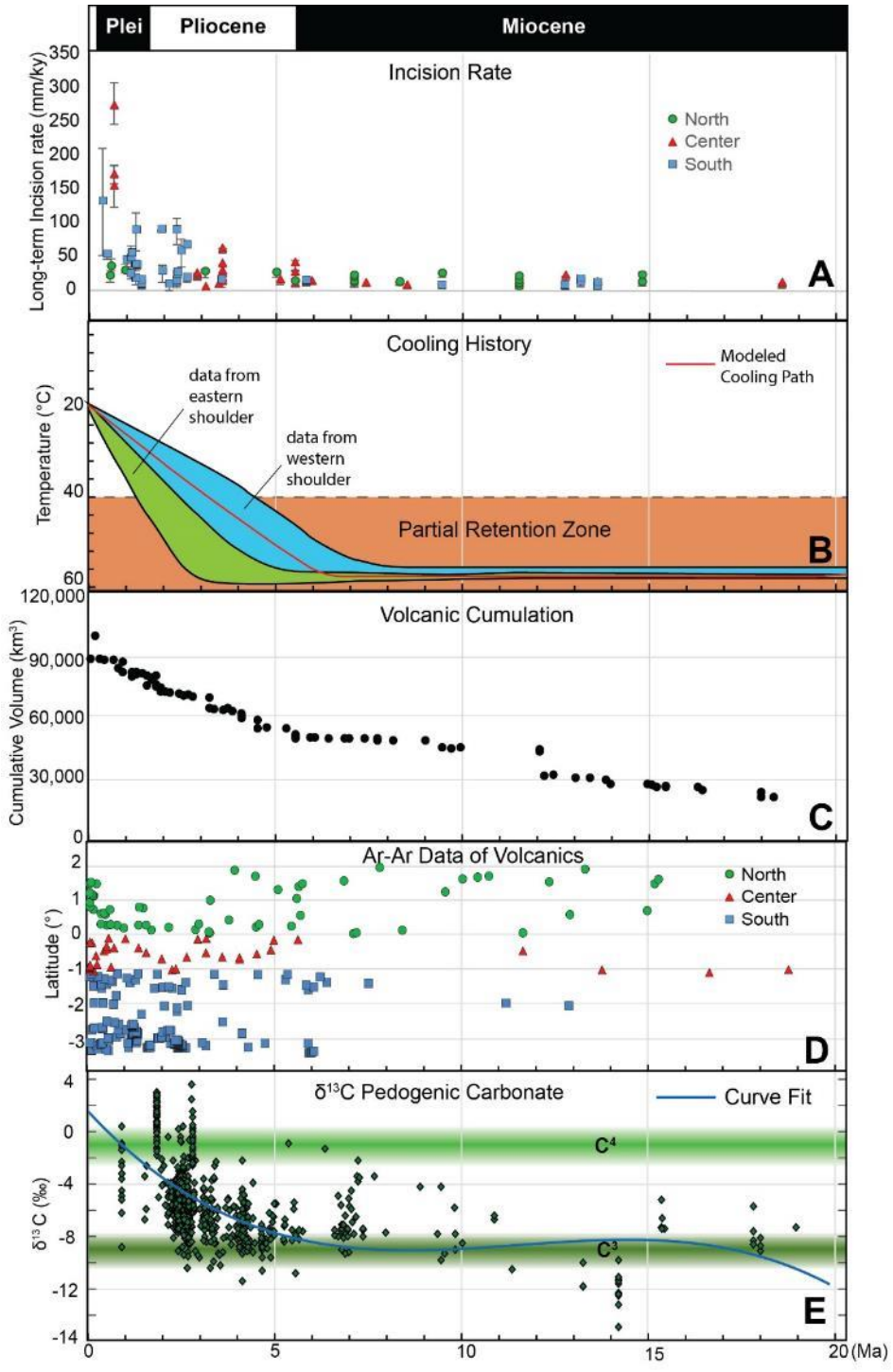

Figure 4- 11 (A) Incision history of the Kenya Rift, (B) Cooling history of western and eastern flanks of the Kenya Rift, modified from (Spiegel et al., 2007). (C) Cumulative volcanic volume in Kenya, modified from [Guth, 2016]; (D) Summary of Ar-Ar data in North, Central, and South Kenya; (E) Pedogenic carbonate δ13C in Kenya Rift [Feakins et al., 2013; Uno et al., 2016], representing local vegetation conditions.

4.5.2. Drainage Incision History and Implications for Tectonic Uplift in Kenya

Various studies have shown evidence of middle Miocene tectonic uplift of the Kenya Rift flanks. Through modeling of fission track thermochronologic ages, *D A Foster and Gleadow* [1996, 1992] reported a rapid Miocene (~10 Ma) denudation (~500 m) from Mathews Range in NKR (Fig. 1C). *Torres Acosta et al.* [2015] concluded that the onset of extension and the border fault activities started at ~ 12-15 Ma in the Elgeyo Escarpment in the NKR (Fig. 1C).

The rapid increase of the drainage incision rate on the flanks of the CKR coincides with the eruption of coeval volcanism, and shifting of the dominant type of vegetation from C3 dominated to C4 dominated, generally from woodland to grassland (Fig. 11). First, *Spiegel et al.* [2007] suggested a phase of renewed tectonic uplift in both the eastern and the western flanks of the Kenya Rift, forming a series of border faults in 4.5 Ma (Fig. 11B). Second, the CKR rapid drainage incision rate starting in 4.5 Ma was accompanied by the extensive pyroclastic eruption [i.e., *Smith,* 1994]. Various geochronologic analysis suggested a Pliocene volcanism in the CKR (Fig. 4), including the Kinangop Plateau [*B Baker et al.,* 1988], Mau Escarpment [*R Crossley and Knight,* 1981; *Jones and Lippard,* 1979], Mt. Kenya [*Schoorl et al.,* 2014; *Veldkamp et al.,* 2012], southern Kinangop Plateau [*Clarke,* 1990], and Lukenya Hill [*Claessens et al.,* 2016]. Such a volcanic event caused a total of 109 eruptions and emplaced ~48,000 km^3 of volcanic materials [*Guth,* 2016], which was correlated with rapid drainage incision of the CKR starting in the 4.5 Ma (Fig. 11C and D). Third, the $\delta^{13}C$ pedogenic carbonate in Kenya showed an overall trend toward more higher $\delta^{13}C$ values from ~6 Ma to present (Fig. 11E) indicating a major change in vegetation. This summarized the data from $\delta^{13}C$ pedogenic carbonate [*Feakins et al.,* 2013; *Uno et al.,* 2016] and noticed that C3 grassland and woodlands in the Miocene were mostly replaced by a combination of C4 grassland and C3/C4 shrubland in the Pliocene. *Spiegel et al.* [2007] also suggested this geomorphological reorganization in the Pliocene may be related to the coeval

regional changes of climate and/or precipitation patterns. Therefore, this correlation between volcanism and drainage incision may likely suggest regional-scale tectonics and/or climatic events in ~4.5 Ma that gave rise to the change in paleoenvironment and associated vegetation type shift in Kenya.

In addition, the drainage incision history observed in the Kenya Rift coincide temporally with major cooling periods related to the tectonic uplift and border faults formation of other sectors in the EARS. Using geomorphological and sedimentological observations, *Pickford* [1990] demonstrated that the flanks of the Western Branch of the EARS were uplifted during late Pliocene. Also, seismic patterns and field observations suggested an uplift of lake Pleistocene lacustrine sequence of ~ 500 m in the Western Branch [*C J Ebinger*, 1989]. Morphotectonic analysis on the northwestern [*Gani et al.*, 2007] and southeastern Ethiopian Plateau [*Xue et al.*, 2018] also suggest a phase of rapid drainage incision starting 4.5 Ma. Therefore, this phase of rapid incision and associated tectonic uplift may not only occur at the Kenya Rift, but also spread widely in East Africa.

4.6. Conclusions

This study provided an integrated framework of the long-term and short-term incision rate and pattern for the drainage systems on the flanks of the Kenya Rift. Our results suggested that:

(1)The long-term incision rates of the three sections of the Kenya rift indicated three distinctive incision patterns, where incision rate increased rapidly since 4.5 Ma in the Central Kenya Rift (>200 mm/ky) and South Kenya Rift (~100 mm/ky). While, the incision rate remains low in North Kenya (<50 mm/ky).

(2) Similar to the long-term incision rate, the chi plot also indicates a higher short-term incision rate in the Central Kenya Rift and a low one in the North and South Kenya. Likewise, the chi map shows more pronounced and drainage divide migration in the Central Kenya Rift than that of

South and South Kenya Rift, caused by the propagation of the rift and associated tectonic uplift of rift flanks.

(3) The rapid increase of incision rate in 4.5 Ma is correlated temporally with the Pliocene flood basalt extrusion in the Central Kenya Rift. Furthermore, this phase matches the coeval rapid crust cooling, cumulative volcanism, major vegetation change in Kenya, implying the existence of major shift in ecosystem and tectonics in 4.5 Ma.

4.7. Reference

Abdelsalam, M. G., and R. J. Stern (1996), Sutures and shear zones in the Arabian-Nubian Shield, *J Afr Earth Sci, 23*(3), 289-310.

Abdelsalam, M. G., J.-P. Liégeois, and R. J. Stern (2002), The saharan metacraton, *J Afr Earth Sci*, *34*(3-4), 119-136.

Baker, B., J. G. Mitchell, and L. Williams (1988), Stratigraphy, geochronology and volcano-tectonic evolution of the Kedong–Naivasha–Kinangop region, Gregory Rift Valley, Kenya, *Journal of the Geological Society*, *145*(1), 107-116.

Baker, B. H., and J. G. Mitchell (1976), Volcanic stratigraphy and geochronology of the Kedong–Olorgesailie area and the evolution of the South Kenya rift valley, *Journal of the Geological Society*, *132*(5), 467-484.

Beauvais, A., and D. Chardon (2013), Modes, tempo, and spatial variability of Cenozoic cratonic denudation: The West African example, *Geochemistry, Geophysics, Geosystems*, *14*(5), 1590-1608.

Bechtel, T. D., D. W. Forsyth, and C. J. Swain (1987), Mechanisms of isostatic compensation in the vicinity of the East African Rift, Kenya, *Geophys J Int*, *90*(2), 445-465.

Beeson, H. W., S. W. McCoy, and A. Keen-Zebert (2017), Geometric disequilibrium of river basins produces long-lived transient landscapes, *Earth Planet Sc Lett, 475*, 34-43.

Birt, C., P. Maguire, M. Khan, H. Thybo, G. R. Keller, and J. Patel (1997), The influence of pre-existing structures on the evolution of the southern Kenya Rift Valley—evidence from seismic and gravity studies, *Tectonophysics*, *278*(1), 211-242.

Brotzu, P., L. Morbidelli, M. Nicoletti, E. Piccirillo, and G. Traversa (1984), Miocene to Quaternary volcanism in eastern Kenya: sequence and geochronology, *Tectonophysics*, *101*(1-2), 75-86.

Chorowicz, J. (2005), The east African rift system, *J Afr Earth Sci*, *43*(1), 379-410.

Claessens, L., A. Veldkamp, J. Schoorl, J. Wijbrans, W. van Gorp, and R. MacDonald (2016), Large scale pantelleritic ash flow eruptions during the Late Miocene in central Kenya and evidence for significant environmental impact, *Global and Planetary Change*, *145*, 30-41.

Clarke, M. C. (1990), *Geological, Volcanological and Hydrogeological Controls on the Occurrence of Geothermal Activity in the Area Surrounding Lake Naivasha, Kenya: With Coloured 1: 250 000 Geological Maps*, Ministry of Energy.

Craig, T., J. Jackson, K. Priestley, and D. McKenzie (2011), Earthquake distribution patterns in Africa: their relationship to variations in lithospheric and geological structure, and their rheological implications, *Geophys J Int*, *185*(1), 403-434.

Crossley, R. (1979), The Cenozoic stratigraphy and structure of the western part of the rift valley in southern Kenya, *Journal of the Geological Society*, *136*(4), 393-405.

Crossley, R., and R. Knight (1981), Volcanism in the western part of the rift valley in southern Kenya, *Bulletin of Volcanology*, *44*(2), 117-128.

Drusch, M., U. Del Bello, S. Carlier, O. Colin, V. Fernandez, F. Gascon, B. Hoersch, C. Isola, P. Laberinti, and P. Martimort (2012), Sentinel-2: ESA's optical high-resolution mission for GMES operational services, *Remote sensing of Environment*, *120*, 25-36.

Ebinger, C. (1989), Tectonic development of the western branch of the East African rift system, *Geol Soc Am Bull*, *101*(7), 885-903.

Ebinger, C., and C. A. Scholz (2012), Continental rift basins: the East African perspective, *Tectonics of Sedimentary Basins: Recent Advances*, 183-208.

Ebinger, C., Y. P. Djomani, E. Mbede, A. Foster, and J. Dawson (1997), Rifting Archaean lithosphere: the Eyasi-Manyara-Natron rifts, East Africa, *Journal of the Geological Society*, *154*(6), 947-960.

Ebinger, C. J. (1989), Tectonic Development of the Western Branch of the East-African Rift System, *Geol Soc Am Bull*, *101*(7), 885-903.

Ebinger, C. J., and N. Sleep (1998), Cenozoic magmatism throughout east Africa resulting from impact of a single plume, *Nature*, *395*(6704), 788-791.

Emishaw, L., D. A. Laó-Dávila, M. G. Abdelsalam, E. A. Atekwana, and S. S. Gao (2017), Evolution of the broadly rifted zone in southern Ethiopia through gravitational collapse and extension of dynamic topography, *Tectonophysics*, *699*, 213-226.

Feakins, S. J., N. E. Levin, H. M. Liddy, A. Sieracki, T. I. Eglinton, and R. Bonnefille (2013), Northeast African vegetation change over 12 my, *Geology*, *41*(3), 295-298.

Foster, A., C. Ebinger, E. Mbede, and D. Rex (1997), Tectonic development of the northern Taiizaiiian sector of the East African Rift System, *Journal of the Geological Society*, *154*(4), 689-700.

Foster, D. A., and A. J. Gleadow (1992), Reactivated tectonic boundaries and implications for the reconstruction of southeastern Australia and northern Victoria Land, Antarctica, *Geology*, *20*(3), 267-270.

Foster, D. A., and A. J. Gleadow (1996), Structural framework and denudation history of the flanks of the Kenya and Anza Rifts, East Africa, *Tectonics*, *15*(2), 258-271.

Fritz, H., M. Abdelsalam, K. Ali, B. Bingen, A. Collins, A. Fowler, W. Ghebreab, C. Hauzenberger, P. Johnson, and T. Kusky (2013), Orogen styles in the East African Orogen: A review of the Neoproterozoic to Cambrian tectonic evolution, *J Afr Earth Sci*, *86*, 65-106.

Furman, T., J. G. Bryce, J. Karson, and A. Iotti (2004), East African Rift System (EARS) plume structure: insights from Quaternary mafic lavas of Turkana, Kenya, *Journal of Petrology*, *45*(5), 1069-1088.

Furman, T., K. M. Kaleta, J. G. Bryce, and B. B. Hanan (2006), Tertiary mafic lavas of Turkana, Kenya: constraints on East African plume structure and the occurrence of high-μ volcanism in Africa, *Journal of Petrology*, *47*(6), 1221-1244.

Gallen, S. F., K. W. Wegmann, and D. Bohnenstiehl (2013), Miocene rejuvenation of topographic relief in the southern Appalachians, *GSA Today*, *23*(2), 4-10.

Gani, N. D., M. R. Gani, and M. G. Abdelsalam (2007), Blue Nile incision on the Ethiopian Plateau: pulsed plateau growth, Pliocene uplift, and hominin evolution, *GSA today*, *17*(9), 4.

George, R., N. Rogers, and S. Kelley (1998), Earliest magmatism in Ethiopia: evidence for two mantle plumes in one flood basalt province, *Geology*, *26*(10), 923-926.

Grimaud, J.-L., D. Chardon, and A. Beauvais (2014), Very long-term incision dynamics of big rivers, *Earth Planet Sc Lett*, *405*, 74-84.

Guth, A. (2016), Volcanic volumes associated with the Kenya Rift: recognition and correction of preservation biases, *Geological Society, London, Special Publications*, *420*(1), 31-42.

Hilley, G. E., and J. R. Arrowsmith (2008), Geomorphic response to uplift along the Dragon's Back pressure ridge, Carrizo Plain, California, *Geology*, *36*(5), 367-370.

Howard, A. D., W. E. Dietrich, and M. A. Seidl (1994), Modeling Fluvial Erosion on Regional to Continental Scales, *J Geophys Res-Sol Ea*, *99*(B7), 13971-13986.

Jones, W., and S. Lippard (1979), New age determinations and the geology of the Kenya Rift-Kavirondo Rift junction, W Kenya, *Journal of the Geological Society*, *136*(6), 693-704.

Katumwehe, A. B., M. G. Abdelsalam, E. A. Atekwana, and D. A. Laó-Dávila (2016), Extent, kinematics and tectonic origin of the Precambrian Aswa Shear Zone in eastern Africa, *Gondwana Research*, *34*, 241-253.

Kirby, E., and K. X. Whipple (2012), Expression of active tectonics in erosional landscapes, *Journal of Structural Geology*, *44*, 54-75.

Kirby, E., K. X. Whipple, W. Q. Tang, and Z. L. Chen (2003), Distribution of active rock uplift along the eastern margin of the Tibetan Plateau: Inferences from bedrock channel longitudinal profiles, *Journal of Geophysical Research: Solid Earth*, *108*(B4).

Koptev, A., E. Calais, E. Burov, S. Leroy, and T. Gerya (2015), Dual continental rift systems generated by plume-lithosphere interaction, *Nat Geosci*, *8*(5), 388-392.

Lavé, J., and J. Avouac (2001), Fluvial incision and tectonic uplift across the Himalayas of central Nepal, *Journal of Geophysical Research: Solid Earth*, *106*(B11), 26561-26591.

Macdonald, R. (2002), Magmatism of the Kenya Rift Valley: a review, *Earth and Environmental Science Transactions of the Royal Society of Edinburgh*, *93*(3), 239-253.

McCall, G. J. H. (1967), *Geology of the Nakuru-Thomson's Falls-Lake Hannington Area: Degree Sheet No. 35 SW Quarter and 43 NW Quarter (with Coloured Maps)*, Geological Survey of Kenya.

McDougall, I., F. H. Brown, P. M. Vasconcelos, B. E. Cohen, D. S. Thiede, and M. J. Buchanan (2012), New single crystal 40Ar/39Ar ages improve time scale for deposition of the Omo Group, Omo–Turkana Basin, East Africa, *Journal of the Geological Society*, *169*(2), 213-226.

Michon, L. (2015), What the volcanism of the East African Rift tells us on its evolution and dynamics: a reappraisal, paper presented at EGU General Assembly Conference Abstracts.

Montgomery, D. R., and M. T. Brandon (2002), Topographic controls on erosion rates in tectonically active mountain ranges, *Earth Planet Sc Lett*, *201*(3-4), 481-489.

Morley, C., and W. Bosworth (1988), Comment and Reply on" Off-axis volcanism in the Gregory rift, east Africa: Implications for models of continental rifting", *Geology*, *16*(6), 569-571.

Morley, C. K., W. Wescott, D. Stone, R. Harper, S. Wigger, and F. Karanja (1992), Tectonic evolution of the northern Kenyan Rift, *Journal of the Geological Society*, *149*(3), 333-348.

Moucha, R., and A. M. Forte (2011), Changes in African topography driven by mantle convection, *Nat Geosci*, *4*(10), 707-712.

Nyblade, A. A., and R. A. Brazier (2002), Precambrian lithospheric controls on the development of the East African rift system, *Geology*, *30*(8), 755-758.

Opdyke, N. D., D. V. Kent, K. Huang, D. A. Foster, and J. Patel (2010), Equatorial paleomagnetic time-averaged field results from 0–5 Ma lavas from Kenya and the latitudinal variation of angular dispersion, *Geochemistry, Geophysics, Geosystems*, *11*(5).

Perron, J. T., and L. Royden (2013), An integral approach to bedrock river profile analysis, *Earth Surf Proc Land*, *38*(6), 570-576.

Pickford, M. (1990), Uplift of the roof of Africa and its bearing on the evolution of mankind, *Human Evolution*, *5*(1), 1-20.

Pik, R., B. Marty, and D. Hilton (2006), How many mantle plumes in Africa? The geochemical point of view, *Chemical Geology*, *226*(3), 100-114.

Prince, P. S., and J. A. Spotila (2013), Evidence of transient topographic disequilibrium in a landward passive margin river system: knickpoints and paleo-landscapes of the New River basin, southern Appalachians, *Earth Surf Proc Land*, *38*(14), 1685-1699.

Rogers, N., R. Macdonald, J. G. Fitton, R. George, M. Smith, and B. Barreiro (2000), Two mantle plumes beneath the East African rift system: Sr, Nd and Pb isotope evidence from Kenya Rift basalts, *Earth Planet Sc Lett*, *176*(3), 387-400.

Saria, E., E. Calais, D. Stamps, D. Delvaux, and C. Hartnady (2014), Present-day kinematics of the East African Rift, *Journal of Geophysical Research: Solid Earth*, *119*(4), 3584-3600.

Schoenbohm, L., K. Whipple, B. Burchfiel, and L. Chen (2004), Geomorphic constraints on surface uplift, exhumation, and plateau growth in the Red River region, Yunnan Province, China, *Geol Soc Am Bull*, *116*(7-8), 895-909.

Schoorl, J., A. Veldkamp, L. Claessens, W. Van Gorp, and J. Wijbrans (2014), Edifice growth and collapse of the Pliocene Mt. Kenya: Evidence of large scale debris avalanches on a high altitude glaciated volcano, *Global and Planetary Change*, *123*, 44-54.

Schwanghart, W., and D. Scherler (2014), TopoToolbox 2-MATLAB-based software for topographic analysis and modeling in Earth surface sciences, *Earth Surface Dynamics*, *2*(1), 1.

Shackleton, R. M. (1984), Thin-skinned tectonics, basement control and the Variscan front, *Geological Society, London, Special Publications*, *14*(1), 125-129.

Shackleton, R. M., and A. C. Ries (1984), The relation between regionally consistent stretching lineations and plate motions, *Journal of Structural Geology*, *6*(1-2), 111-117.

Simiyu, S. M., and G. R. Keller (2001), An integrated geophysical analysis of the upper crust of the southern Kenya rift, *Geophys J Int*, *147*(3), 543-561.

Sippel, J., C. Meeßen, M. Cacace, J. Mechie, S. Fishwick, C. Heine, M. Scheck-Wenderoth, and M. R. Strecker (2017), The Kenya rift revisited: insights into lithospheric strength through data-driven 3-D gravity and thermal modelling, *Solid Earth*, *8*(1), 45.

Smith, M. (1994), Stratigraphic and structural constraints on mechanisms of active rifting in the Gregory Rift, Kenya, *Tectonophysics*, *236*(1-4), 3-22.

Smith, M., and P. Mosley (1993), Crustal heterogeneity and basement influence on the development of the Kenya Rift, East Africa, *Tectonics*, *12*(2), 591-606.

Spiegel, C., B. P. Kohn, D. X. Belton, and A. J. Gleadow (2007), Morphotectonic evolution of the central Kenya rift flanks: Implications for late Cenozoic environmental change in East Africa, *Geology*, *35*(5), 427-430.

Stern, R. J. (1994), Arc assembly and continental collision in the Neoproterozoic East African Orogen: implications for the consolidation of Gondwanaland, *Annual Review of Earth and Planetary Sciences*, *22*(1), 319-351.

Thouret, J.-C., G. Wörner, Y. Gunnell, B. Singer, X. Zhang, and T. Souriot (2007), Geochronologic and stratigraphic constraints on canyon incision and Miocene uplift of the Central Andes in Peru, *Earth Planet Sc Lett*, *263*(3-4), 151-166.

Torres Acosta, V., A. Bande, E. R. Sobel, M. Parra, T. F. Schildgen, F. Stuart, and M. R. Strecker (2015), Cenozoic extension in the Kenya Rift from low-temperature thermochronology: Links to diachronous spatiotemporal evolution of rifting in East Africa, *Tectonics*, *34*(12), 2367-2386.

Uno, K. T., P. J. Polissar, and K. E. Jackson (2016), Neogene biomarker record of vegetation change in eastern Africa, *Proceedings of the National Academy of Sciences*, *113*(23), 6355-6363.

Veldkamp, A., J. Schoorl, J. Wijbrans, and L. Claessens (2012), Mount Kenya volcanic activity and the Late Cenozoic landscape reorganisation in the upper Tana fluvial system, *Geomorphology*, *145*, 19-31.

Veldkamp, A., E. Buis, J. Wijbrans, D. Olago, E. Boshoven, M. Marée, and R. v. d. B. van Saparoea (2007), Late Cenozoic fluvial dynamics of the River Tana, Kenya, an uplift dominated record, *Quaternary Science Reviews*, *26*(22), 2897-2912.

Wagner, M., R. Altherr, and P. Van Den Haute (1992), Apatite fission-track analysis of Kenyan basement rocks: constraints on the thermotectonic evolution of the Kenya dome. A reconnaissance study, *Tectonophysics*, *204*(1), 93-110.

Whipple, K. X. (2004), Bedrock rivers and the geomorphology of active orogens, *Annual Review of Earth and Planetary Sciences 32*, 151-185.

Whipple, K. X., and G. E. Tucker (1999), Dynamics of the stream-power river incision model: Implications for height limits of mountain ranges, landscape response timescales, and research needs, *J Geophys Res-Sol Ea*, *104*(B8), 17661-17674.

Wichura, H., R. Bousquet, R. Oberhänsli, M. R. Strecker, and M. H. Trauth (2010), Evidence for middle Miocene uplift of the East African Plateau, *Geology*, *38*(6), 543-546.

Wichura, H., R. Bousquet, R. Oberhänsli, M. R. Strecker, and M. H. Trauth (2011), The Mid-Miocene East African Plateau: a pre-rift topographic model inferred from the emplacement of the phonolitic Yatta lava flow, Kenya, *Geological Society, London, Special Publications*, *357*(1), 285-300.

Wichura, H., L. L. Jacobs, A. Lin, M. J. Polcyn, F. K. Manthi, D. A. Winkler, M. R. Strecker, and M. Clemens (2015), A 17-My-old whale constrains onset of uplift and climate change in east Africa, *Proceedings of the National Academy of Sciences*, *112*(13), 3910-3915.

Wilkinson, P., J. Mitchell, P. Cattermole, and C. Downie (1986), Volcanic chronology of the Men–Kilimanjaro region, Northern Tanzania, *Journal of the Geological Society*, *143*(4), 601-605.

Willett, S. D., S. W. McCoy, J. T. Perron, L. Goren, and C. Y. Chen (2014), Dynamic reorganization of river basins, *Science*, *343*(6175), 1248765.

Wobus, C., K. X. Whipple, E. Kirby, N. Snyder, J. Johnson, K. Spyropolou, B. Crosby, and D. Sheehan (2006), Tectonics from topography: procedures, promise, and pitfalls, *Geological Society of America Special Papers*, *398*, 55-74.

Xue, L., T. Alemu, N. D. Gani, and M. G. Abdelsalam (2018), Spatial and temporal variation of tectonic uplift in the southeastern Ethiopian Plateau from morphotectonic analysis, *Geomorphology*, *309*, 98-111.

APPENDICES

Appendices 1. Identification of knickpoint locations

We selected the knickpoints for the streams with order >3 in the SEEP. We extracted Log S- Log A and longitudinal profiles (A, B, D, E) from ASTER DEM using Stream profiler [Kirby and Whipple, 2012; Kirby et al., 2003; Wobus et al., 2006]. Also, to distinguish between knickpoints caused by tectonic uplift and/or enhanced precipitation from those formed due to difference in rock erodibility, we applied geologic maps and false colored map with Sentinel-2 band combination 12/8/3 (C, F). For example, Log S- Log A profiles suggested knickpoints in Basin 33 and Basin 19. The knickpoint in basin 33 suggested a 'vertical-step' pattern, while the knickpoints in Basin 19 has a 'slope-break' pattern [Kirby and Whipple, 2012]. Detailed analysis of lithology indicated the knickpoint in Basin 33 located at the contact between Mesozoic sediments and Quaternary alluvial deposits (C), while the knickpoints in Basin 19 have homogeneous lithology (F). Therefore, we kept the knickpoints in the Basin 19 and remove these in Basin 33 for the knickpoint celerity model.

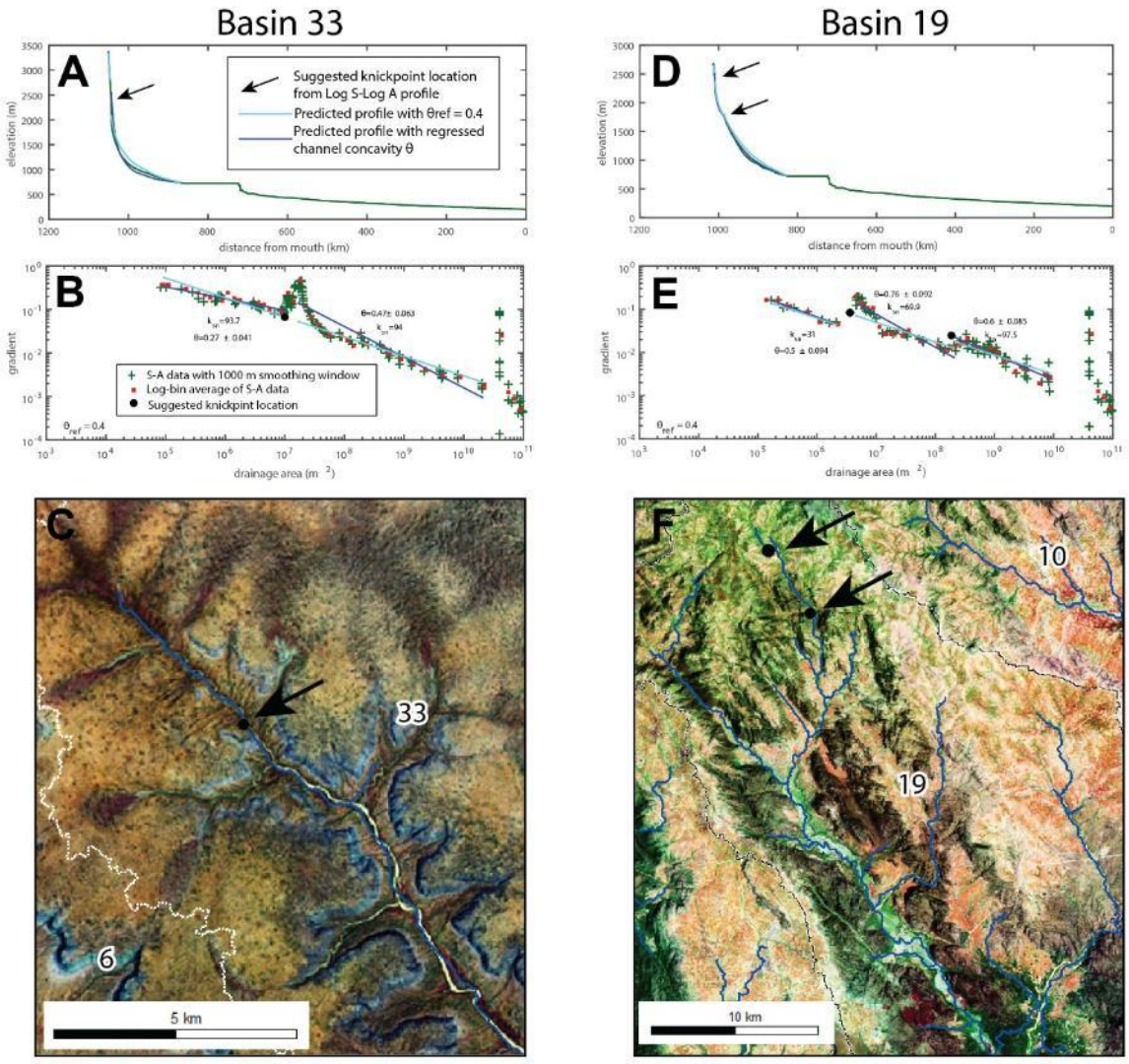

Appendices 1. Longitudinal profiles of the major stream in (A) Basin 33 and (D) Basin 19. Slope-Area plots of the major stream in (B) Basin 33 and (D) Basin 19, showing 'vertical-step' and 'slope-break' knickpoint pattern.

Appendices 2. Calculation of m/n

The χ value depends on the concavity index m/n. When a stream profile fits equation (7) with uniform K and E, all the streams should be collinear in χ-elevation space [Perron and Royden, 2013]. The correct m/n value would collapse the mainstream and its tributaries into a single line [Perron and Royden, 2013]. Mudd et al. [2014] proposed code and reproducible methodology to evaluate best fit m/n ratio (code available online: https://github.com/LSDtopotools/LSDTopoTools_ChiMudd2014). We applied the AICC-collinearity tests, as suggested by Mudd et al. [2014], and we explored the m/n ratio from 0.15 to 0.75 with an interval of 0.05, generating movern files. Then we took these movern files for AICC-collinearity tests and found the best fit for the m/n ratio to be 0.4.

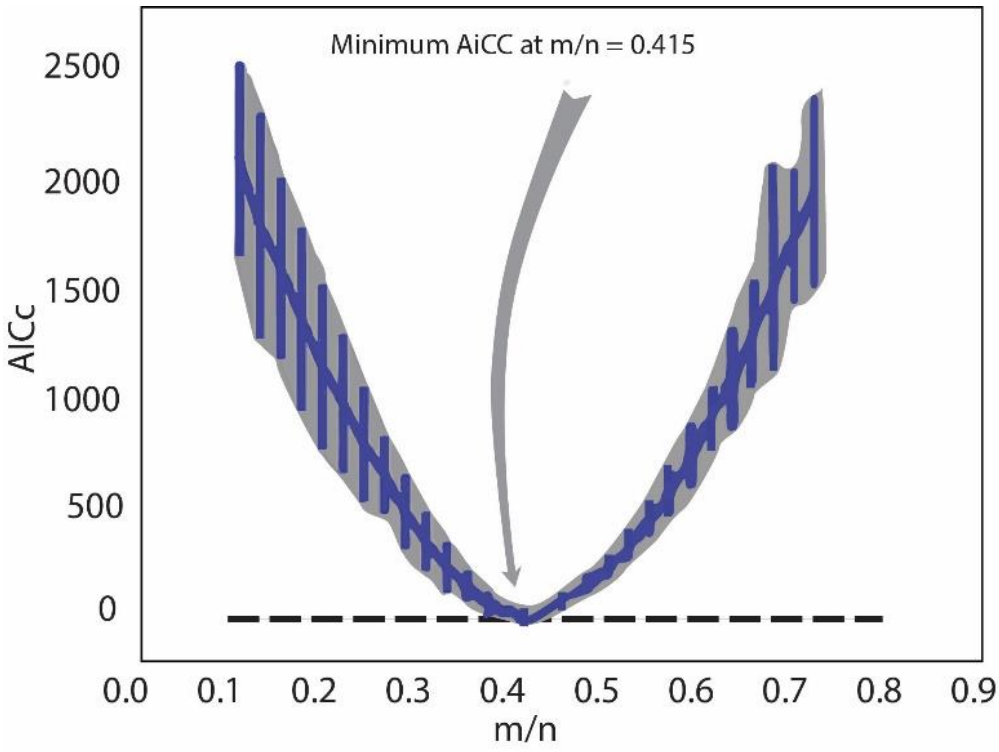

Appendices 3. Summary of Ar-Ar samples in the Kenya Rift.

Sample	long	lat	material	Corrected Age(Ma)	Error	reference
ESMT-2	36.05092	-3.42436	matrix	5.95	0.01	
			whole rock	5.93	0.01	
ESMT-4	36.05192	-3.42358	nepheline			
ES14-2008	36.05444	-3.42808	nepheline	5.91	0.01	
				5.9	0.07	Mana et al., 2012
ES-8	35.9945	-3.46478	whole rock	5.86	0.02	
ES-18	36.00921	-3.46362	whole rock	5.89	0.02	
ES-3	35.99492	-3.47224	whole rock	5.83	0.01	
01-SM-3	35.40268	-3.19243	matrix	5.8	0.02	
01-SM-5	35.41198	-3.19159	matrix	4.66	0.05	
04-NT-3	35.22927	-3.30222	matrix	4.22	0.02	
ENGB	35.38344	-2.90816	matrix	4.05	0.02	
00-LM-6	35.39075	-3.17588	matrix	2.99	0.02	
00-LM-7	35.39086	-3.17494	matrix	2.26	0.01	
02-LM-4	35.33113	-3.09797	matrix	2.27	0.01	Mollel et al., 2011
04-OS-1,	35.28951	-3.21938	anorthoclase	2.24	0.01	
04-OS-3,	35.29458	-3.22259	matrix	2.42	0.01	
04-OS-4,	35.29602	-3.22081	matrix	2.3	0.004	
04-OG-1	35.16988	-3.23186	matrix	2.32	0.01	
04-OG-2	35.2327	-3.21322	matrix	2.28	0.05	
NG-DS		n.r.	Anorthoclase	2.02	0.02	
NG-AS		n.r.	Anorthoclase	2.24	0.08	Mollel et al., 2008
NG8		n.r.	Matrix	2.21	0.02	
NG2		n.r.	Matrix	2.26	0.02	
00-OLT2	35.67649	-3.02063	matrix	2.02	0.04	
00-OLT5	35.67789	-3.02009	matrix	1.91	0.02	
03-OLT1	35.65111	-3.033	matrix	1.86	0.01	
03-OLT2	35.6507	-3.03342	matrix	1.88	0.02	Mollel et al., 2009
03-OLT3	35.65213	-3.03298	matrix	1.81	0.01	
04-OLT2	35.66463	-3.03418	anorthoclase	1.86	0.03	
04-OLT4	35.66099	-3.0329	matrix	1.84	0.04	

03-OLDI-1	35.35181	-3.32075	matrix	1.53	0.02	
03-OLDI-2	35.35937	-3.31225	matrix	1.59	0.02	
03-OLDI-4	35.36428	-3.31098	matrix	1.62	0.01	Mollel et al., 2011
03-OLDI-5	35.36934	-3.31246	matrix	1.56	0.02	
04-OLDI-3	35.42758	-3.252	matrix	1.58	0.03	
04-OLDI-4	35.41454	-3.23682	matrix	1.62	0.03	
LS-3			matrix	1.32	0.03	
LL-8			matrix	1.36	0.02	Mollel in progress
LL-13			matrix	1.36	0.04	
EMB3	35.83999	-2.88206	matrix	1.17	0.04	
EMB6	35.86115	-2.9059	nepheline	1.14	0.01	Mollel et al., 2011
			matrix	1.07	0.01	
EMB5	35.86037	-2.90545	matrix	0.82	0.02	
S10-L9	35.9829	-2.72834	groundmass	0.34	0.85	
S10-L40	35.97977	-2.79847	phlogopite	0.93	0.07	
S10-L103	35.9497	-2.77178	alkali feldspar	0.34	0.23	Sherrod et al., 2013
S10-L236B	35.9501	-2.75785	phlogopite	0.36	0.65	
S10-L136	35.8875	-2.55074	phlogopite	0.46	0.75	
S10-L65	35.9836	-2.63733	phlogopite	0.78	0.63	
KA1814		n.r.	nephelinite	4.75	0.07	Isaac and Curtis, 1974
NATM89-07	35.8401	-2.5637		3.53	0.06	Manega, 1993
KA1757		n.r.	biotite lava	3.26	0.08	Isaac and Curtis, 1974
309		a	olivine basalt	2.46	0.62	
305		a	sodic trachite	2.32	0.06	Macintrye et al., 1974(map)
510		a	sodic trachite	2.27	0.1	
306		a	sodic trachite	2.26	0.06	
3705		14	alkali basalt	2.49	0.06	
				2.44	0.06	Wilkinson et al., 1986 (map)
3706		14	mugearite	2.3	0.06	
				2.25	0.04	
490		b	sodic trachite	2.22	0.06	Macintrye et al., 1974 (map)
				2.1	0.04	
				2.03	0.03	

488		b	sodic trachite	1.97	0.04	
136	36.46361	-3.19444	olivine basalt	2.14	0.06	
				2.24	0.05	
155		Y	olivine basalt	1.58	0.1	Evans et al., 1971
				1.7	0.07	
156		Y	olivine basalt	1.79	0.08	
				1.93	0.08	
05KI07C			trachybasalt	1.926	0.041	Nonnotte et al., 2008
05KI08B			basanite	1.974	0.042	
7c	35.2167	-3.2647	ankaramite	3.08	0.3	Foster et al., 1997
304		d	olivine basalt	2.06	0.5	
191		c	olivine basalt	1.72	0.08	
				1.81	0.11	Macintrye et al., 1974(map)
139		e	olivine trachybasalt	1.28	0.03	
				1.23	0.04	
				1.21	0.05	
S13/3	35.9401	-3.1926	basalt	1.02	0.1	
S14/5	35.9374	-3.1782	basalt	1.24	0.06	
S13/2	36.0242	-3.0977	olivine basalt	1.26	0.07	Foster et al., 1997
3			phlogopite	0.59	0.15	
			phlogopite	0.14	0.15	
891			phlogopite	0.55	0.1	
			phlogopite	0.42	0.1	
137	36.21306	-3.31528	nephelinite	1.03	0.04	Macintrye et al., 1974(map)
138			nephelinite	0.98	0.03	
05KI43B			trachybasalt	0.492	0.011	
05KI45			trachybasalt	0.488	0.011	Evans et al., 1971 (map)
KIBO						
05KI14			phono-tephrite	0.482	0.01	
05KI05A			phonolite	0.359	0.008	
05KI03A			phonolite	0.348	0.007	
05KI29			phonolite	0.346	0.008	
05KI32			phonolite	0.343	0.007	
05KI37			phonolite	0.339	0.007	Nonnotte et al., 2008 (map)
05KI30			phonolite	0.337	0.007	
05KI17			phonolite	0.274	0.006	
05KI12			phonolite	0.258	0.006	
05KI38B			phonolite	0.227	0.005	
05KI24			phonolite	0.209	0.005	
05KI41B			basanite	0.195	0.005	
03TZ42B			basanite	0.165	0.005	

3436			phonolitic nephelinite	1.53	0.03	
				1.49	0.03	
3193			trachytoid phonolite	0.383	0.009	
3912			phonolite	0.311	0.011	
				0.3	0.011	
3303			phonolitic nephelinite	0.313	0.009	
				0.303	0.01	
				0.299	0.01	
3127			phonolitic nephelinite	0.281	0.005	
			sanidine phonolite	0.179	0.01	
				0.168	0.009	
				0.158	0.01	
4191			nephelinite	0.148	0.013	
				0.148	0.01	
			phonolitic tephrite	0.111	0.007	Wikinson et al., 1986(map)
				0.107	0.007	
3114			phonolitic tephrite	0.107	0.006	
				0.102	0.005	
3930			phonolitic nephelinite	0.09	0.004	
				0.079	0.004	
3655			nephelinite	0.08	0.005	
				0.08	0.005	
3403			nephelinite	0.067	0.008	
				0.059	0.01	
105			olivine nephelinite	0.15	0.12	
10-BRK-12	36.20278	-3.32836	wr	2.553	0.009	
10-BRK-16	36.19042	-3.32908	matrix	2.337	0.008	
10-MON-02	36.42457	-3.25272	wr	2.442	0.006	Macintrye et al., 1974(map)
10-MON-03	36.42217	-3.25244	matrix	2.431	0.004	Mana et al., 2015
10-MON-04	36.42019	-3.25178	matrix	2.469	0.005	

10-MON-07	36.46858	-3.28394	matrix	2.344	0.01
10-MON-10	36.46858	-3.28394	wr	2.395	0.006
10-MON-11	36.46858	-3.28394	matrix	2.376	0.01
MR103	36.52955	-3.23224	plag	2.39	0.06
MR104	36.52893	-3.22943	matrix	2.381	0.013
MR220	36.45217	-3.27872	matrix	2.462	0.007
MR226	36.40263	-3.25991	matrix	2.401	0.005
MR110	36.53735	-3.16865	matrix	2.338	0.013
MR240	36.44998	-3.18968	wr	2.351	0.007
10-TRS-01	36.37078	-3.21715	matrix	2.342	0.005
10-TRS-02	36.36052	-3.20247	wr	2.346	0.002
10-TRS-03	36.35757	-3.19976	plag	2.302	0.005
10-TRS-05	36.35497	-3.19538	matrix	2.355	0.004
BD521	36.33667	-3.26833	wr	2.348	0.004
BD261	36.25667	-3.195	matrix	2.363	0.004
BD256	36.26667	-3.13333	plag	2.327	0.004
BD512	36.31167	-3.225	matrix	2.325	0.003
BD324	36.375	-3.14667	plag	2.358	0.003
BD270	36.34167	-3.12667	wr	2.35	0.003
BD306	36.34167	-3.1	mag	2.338	0.003
BD510	36.31167	-3.225	plag	2.352	0.004
10-KTM-01	36.21862	-2.81953	matrix	2.066	0.007
10-KTM-02	36.21916	-2.81989	matrix	2.111	0.007
10-KTM-03	36.22268	-2.81185	matrix	2.163	0.005
10-KTM-04	36.22105	-2.80484	matrix	2.124	0.008
KTG-4B	36.12413	-2.86007	matrix	1.941	0.016
KTG-3	36.1277	-2.8504	matrix	1.248	0.004
KTT-2	36.10345	-2.91541	matrix	1.279	0.004
KTT-3	36.10361	-2.91526	matrix	1.25	0.003
KTW-2A	36.11394	-2.8958	matrix	1.235	0.003
KTW-3B	36.11461	-2.89398	wr	1.286	0.004
10-GEL-01	36.10448	-2.68366	wr	1.116	0.004
10-GEL-03	36.10639	-2.67786	matrix	1.106	0.002
10-GEL-04	36.10398	-2.68128	matrix	1.121	0.002
10-GEL-05	36.10247	-2.68266	matrix	1.13	0.002
10-GEL-06	36.07478	-2.65594	matrix	1.13	0.003
10-GEL-10	36.11277	-2.70499	matrix	1.139	0.012
10-GEL-13	36.14754	-2.63967	matrix	1.123	0.002

10-GEL-14	36.15082	-2.63901	matrix	1.165	0.003	
10-GEL-19	36.12638	-2.72956	matrix	1.191	0.005	
10-GEL-20	36.12623	-2.7304	matrix	1.152	0.013	
MR89	36.54576	-3.40629	matrix	0.499	0.005	
MR92	36.51065	-3.38136	matrix	0.453	0.008	
MR154	36.77287	-3.20895	wr	0.301	0.003	
MR2	36.74772	-3.39414	matrix	0.056	0.008	
MR168	36.86491	-3.16233	matrix	0.011	0.002	
MR260	36.81636	-3.16641	matrix	0.046	0.004	
10-KER-04	35.96291	-2.92783	matrix	1.09	0.02	
10-LOO-01	35.97976	-2.79844	mica	0.759	0.01	
10-LOO-06	35.98326	-2.79788	wr	0.069	0.009	
1-KM 318	37.88333	1.533333		12.2	3	
2-KM 202	37.81667	1.7		10.6	0.7	
3-KM 324	37.86667	1.666667		10.3	1	
4-KM 308	37.88333	1.616667		9.9	1	
6-KM 301	37.2	1.95		7.7	0.4	
7-KM 263	37.63333	2.95		7.3	0.5	
8-KM 252	37.51667	3.233333		5.4	0.5	
9-KM 277	37.28333	3.866667		6.1	0.6	
10-KM 270	37.26667	3.6		4.5	0.3	
15-KM 114	38.11667	0.283333		4.5	0.25	
16-KM 113	38.05	0.3		2.9	0.4	Brotzu et al., 1984
17-KM 130	37.93333	0.2		2.1	0.12	
18-KM 128	37.9	0.266667		1.3	0.04	
19-Km 131	37.91667	0.183333		0.91	0.13	
20-Km 151	37.76667	0.266667		0.46	0.06	
25_KM 243	37.76667	2.716667		0.6	0.2	
29_KM257	37.7	3.316667		2.3	0.17	
30-KM 258	37.71667	3.383333		1.9	0.15	
31-KM 259	37.75	3.416667		1.4	0.5	
32-KM271	37.33333	3.85		0.9	0.3	
KAII	37.30333	-0.44233		0.45	0.17	
KAM	37.21933	0.0685		3.17	0.22	Opdyke et al., 2010
KAW	37.672	-0.1575		5.53	0.88	

KAZ	37.67533	-0.1725	4.89	0.21
KBC	37.84383	0.258667	0.73	0.3
KBQ	37.986	0.293667	0.3	0.25
KCK	37.6285	0.207333	4.42	1.05
KCL	37.66267	0.126	1.64	0.5
KEB	37.09233	-0.45733	4.81	0.26
KEE	37.169	-0.57683	4.44	0.43
KEF	37.20217	-0.66983	2.58	0.73
KEK	37.14183	0.039	3.19	0.27
KEP	37.4615	0.132833	2.81	0.34
KGO	37.61683	0.237167	5.36	1.06
KBY	36.82267	2.823667	3.9	0.9
KBZ	36.78983	2.811167	4.84	0.44
KCC	36.766	2.993667	4.51	0.96
KFZ	36.70983	2.588333	3.64	0.28

VITA

LIANG XUE

Candidate for the Degree of

Doctor of Philosophy

Dissertation: MORPHO-TECTONIC ANALYSIS OF THE DRAINAGE SYSTEMS IN THE EAST AFRICAN RIFT

Major Field: GEOLOGY

Education:

Completed the requirements for the Doctor of Philosophy in your major at Oklahoma State University, Stillwater, Oklahoma in July, 2018.

Completed the requirements for the Master of Science in Geology at Missouri University of Science and Technology, Rolla, MO in 2014.

Completed the requirements for the Bachelor of Engineering in Geological Engineering at Central South University, Changsha, China in 2011.